

Tensor-train Thermo-field Memory Kernels for Generalized Quantum Master Equations

Ningyi Lyu,^{†,||} Ellen Mulvihill,^{†,||} Micheline B. Soley,^{†,‡,¶} Eitan Geva,^{*,§} and Victor S. Batista^{*,†,‡}

[†]*Department of Chemistry, Yale University, New Haven, CT 06520, U.S.A.*

[‡]*Yale Quantum Institute, Yale University, New Haven, CT 06511, U.S.A.*

[¶]*Department of Chemistry, University of Wisconsin-Madison, Madison, WI 53706, U.S.A.*

[§]*Department of Chemistry, University of Michigan, Ann Arbor, MI 48109, U.S.A.*

|| These authors contributed equally.

E-mail: eitan@umich.edu; victor.batista@yale.edu

Abstract

The generalized quantum master equation (GQME) approach provides a rigorous framework for deriving the exact equation of motion for any subset of electronic reduced density matrix elements (e.g., the diagonal elements). In the context of electronic dynamics, the memory kernel and inhomogeneous term of the GQME introduce the implicit coupling to nuclear motion or dynamics of electronic density matrix elements that are projected out (e.g., the off-diagonal elements), allowing for efficient quantum dynamics simulations. Here, we focus on benchmark quantum simulations of electronic dynamics in a spin-boson model system described by various types of GQMEs. Exact memory kernels and inhomogeneous terms are obtained from short-time quantum-mechanically exact tensor-train thermo-field dynamics (TT-TFD) simulations and are compared with those obtained from an approximate linearized semiclassical method.

The TT-TFD memory kernels can provide insights on the main sources of inaccuracies of GQME approaches when combined with approximate input methods and pave the road for development of quantum circuits that could implement GQMEs on digital quantum computers.

1 Introduction

Quantum dynamics simulations are central to theoretical studies of many areas of chemistry and technological applications, including charge and energy transfer in photosynthetic and photovoltaic systems and a wide range of reactions with nonadiabatic dynamics and photochemical processes, including spin and vibrational energy relaxation as well as polaritonic chemistry.¹⁻¹² Despite considerable progress over the past few decades, the development of efficient methods for simulations of quantum dynamics remains an outstanding challenge for studies of complex molecular systems at finite temperature.¹³⁻²⁶ This is primarily due to the computational cost of quantum-mechanically exact simulations, which scales exponentially with the number of degrees of freedom in the system, thereby making such simulations intractable in most complex molecular systems of practical interest. Thus, reduced-dimensionality approaches that can offer more favorable scaling are highly desirable.

The Nakajima-Zwanzig generalized quantum master equation (GQME)^{17,18} provides a formally exact general-purpose framework for modeling quantum dynamics in reduced dimensionality. It can be obtained for any subset of reduced density matrix elements by using suitable projection operators.¹⁹ When focusing on electronic dynamics, the effect of projecting out nuclear degrees of freedoms (DOF) or electronic density matrix elements not included in the subset of interest is accounted for by the *memory kernel* and the *inhomogeneous term* of the GQME. The dimensionality of those spatially and temporally compact quantities is typically much lower than the dimensionality of the overall system since it is determined by the number of reduced density matrix elements included in the subset of interest, allowing for efficient simulations.

Considerable progress has already been made towards calculating the aforementioned memory kernels and inhomogeneous terms without resorting to perturbation theory.^{19,27–52} Much of that progress has been based on the strategy introduced by Shi and Geva,²⁷ which relies on formally exact relationships between the memory kernel and the inhomogeneous term and projection-free inputs (PFIs) that are given in terms of two-time correlation functions of the overall system. These PFIs can be obtained from quantum-mechanically exact or approximate (e.g., semiclassical or mixed quantum-classical) input methods.^{19,27–50,52}

In this paper, we introduce exact memory kernels and inhomogeneous terms obtained from quantum-mechanically exact tensor-train thermo-field dynamics (TT-TFD) simulations.^{53,54} To the best of our knowledge, this is the first application of TT-TFD to calculations of memory kernels and inhomogeneous terms of GQMEs. Previously, exact memory kernels have been obtained by the Geva,²⁷ Shi,^{47–50} Makri,⁵¹ and Rabani^{31,33,34,36,55} groups. This paper extends the available exact results to include the memory kernels and inhomogeneous terms of the modified GQME and reduced-dimensionality GQME approaches for the spin-boson model. We demonstrate the capabilities of the GQMEs as applied to benchmark simulations of electronic relaxation dynamics in a spin-boson model system, including calculations based on various types of reduced-dimensionality GQMEs. The spin-boson benchmark model provides a useful framework for modeling molecular systems with coupled electronic states. The resulting quantum-mechanically exact memory kernels and inhomogeneous terms can serve as benchmarks for assessing the accuracy of approximate memory kernels and inhomogeneous terms obtained by approximate input methods. In addition, the reported quantum-mechanically exact memory kernels and inhomogeneous terms could enable the development of quantum circuits for the implementation of GQMEs on digital quantum computers.

The paper is organized as follows. The objectives and scope of our approach are presented in Sec. 2, the GQME formalism is outlined in Sec. 3, and the protocol used for calculating the PFIs via TT-TFD is described in Sec. 4. The utility of combining the GQME and TT-TFD

approaches is demonstrated for the benchmark spin-boson model in Sec. 5. Also included in Sec. 5 is a comprehensive comparison between the TT-TFD-based quantum-mechanically exact results and the corresponding approximate results based on PFIs previously obtained with approximate linearized semiclassical mapping Hamiltonian methods.¹⁹ Concluding remarks are provided in Sec. 6. Additional graphs and computational details are included in supporting information (SI).

2 Model System

We focus on molecular systems exhibiting nonadiabatic quantum dynamics such as photosynthetic and photovoltaic molecular assemblies, commonly described by the following model Hamiltonian:

$$\hat{H} = \sum_{j=1}^{N_e} \hat{H}_j |j\rangle\langle j| + \sum_{\substack{j,k=1 \\ j \neq k}}^{N_e} \hat{V}_{jk} |j\rangle\langle k|, \quad (1)$$

Here, $\hat{H}_j = \hat{\mathbf{P}}^2/2 + V_j(\hat{\mathbf{R}})$ is the nuclear Hamiltonian when the system is in diabatic electronic state $|j\rangle$, with index j running over the N_e electronic states ($j = 1, 2, \dots, N_e$), while $\hat{\mathbf{R}} = (\hat{R}_1, \dots, \hat{R}_{N_n})$ and $\hat{\mathbf{P}} = (\hat{P}_1, \dots, \hat{P}_{N_n})$ are the mass-weighted position and momentum operators of the $N_n \gg 1$ nuclear DOF, and $\{\hat{V}_{jk}|j \neq k\}$ are coupling terms between electronic states which can be either nuclear operators (non-Condon case) or constants (Condon case). Throughout this paper, a hat over a variable (e.g., \hat{B}) indicates an operator quantity and calligraphic font (e.g., \mathcal{L}) indicates a superoperator.

For simplicity, we assume that the initial state of the overall system has the single-product form,

$$\hat{\rho}(0) = \hat{\rho}_n(0) \otimes \hat{\sigma}(0). \quad (2)$$

Here, $\hat{\rho}_n(0) = \text{Tr}_e\{\hat{\rho}(0)\}$ and $\hat{\sigma}(0) = \text{Tr}_n\{\hat{\rho}(0)\}$ are the reduced density operators that describe the initial states of nuclear DOF and electronic DOF, respectively, while $\text{Tr}_e\{\cdot\}$ and $\text{Tr}_n\{\cdot\}$ represent partial traces over the electronic and nuclear Hilbert spaces, respectively.

It should be noted that the methodology presented in this paper is not limited to factorized initial states, as introduced by Eq. (2), and can be applied to arbitrary initial states.⁴³

The time-dependent propagation of the initial state, introduced by Eq. (2), according to the Hamiltonian introduced by Eq. (1) yields the propagated state $\hat{\rho}(t)$ at time t described by the following density operator:

$$\hat{\rho}(t) = e^{-i\hat{H}t/\hbar}\hat{\rho}_n(0) \otimes \hat{\sigma}(0)e^{i\hat{H}t/\hbar} \equiv e^{-i\mathcal{L}t/\hbar}\hat{\rho}_n(0) \otimes \hat{\sigma}(0). \quad (3)$$

Here, $\mathcal{L}(\cdot) = [\hat{H}, \cdot]$ is the overall Liouvillian superoperator. The reduced electronic density operator $\hat{\sigma}(t)$ at time t is obtained by tracing out the nuclear, as follows:

$$\hat{\sigma}(t) = \text{Tr}_n\{\hat{\rho}(t)\} = \sum_{j,k=1}^{N_e} \sigma_{jk}(t)|j\rangle\langle k|. \quad (4)$$

The electronic populations and coherences are given by $\{\sigma_{jj}(t) = \langle j|\hat{\sigma}(t)|j\rangle\}$ and $\{\sigma_{jk}(t) = \langle j|\hat{\sigma}(t)|k\rangle|j \neq k\}$, respectively. These quantities are of particular interest because their time evolution underlies electronic energy, charge, and coherence transfer dynamics, as well as electronic decoherence.

3 GQMEs in Reduced Dimensionality

The GQME formalism can be applied to derive exact equations of motion for electronic observables while keeping the input regarding other DOF in the system to the minimum necessary to account for their impact on dynamics. To this end, we begin with the well-known Nakajima-Zwanzig GQME (whose derivation is outlined in the SI),

$$\frac{d}{dt}\mathcal{P}\hat{\rho}(t) = -\frac{i}{\hbar}\mathcal{P}\mathcal{L}\mathcal{P}\hat{\rho}(t) - \frac{1}{\hbar^2}\int_0^t d\tau\mathcal{P}\mathcal{L}e^{-i\mathcal{Q}\mathcal{L}\tau/\hbar}\mathcal{Q}\mathcal{L}\mathcal{P}\hat{\rho}(t-\tau) - \frac{i}{\hbar}\mathcal{P}\mathcal{L}e^{-i\mathcal{Q}\mathcal{L}t/\hbar}\mathcal{Q}\hat{\rho}(0), \quad (5)$$

where \mathcal{P} is a projection superoperator.^{17,18} Here, $\mathcal{Q} = 1 - \mathcal{P}$ is the projection complementary to \mathcal{P} , 1 is the identity superoperator, and \mathcal{L} is the Liouvillian superoperator as in Eq. (3). Integrating Eq. (5), we obtain the time-dependent projected state $\mathcal{P}\hat{\rho}(t)$. Importantly, there is a lot of flexibility on the choice of \mathcal{P} to select the specific quantity of interest.¹⁹

In this paper, we focus on quantities of interest corresponding to a subset of electronic reduced density matrix elements $\{\sigma_{ab}(t)\}$ by introducing the following projection operators:

$$\mathcal{P}^{\text{set}}\hat{A} = \sum_{jk \in \{ab\}} \text{Tr} \left\{ \left(|j\rangle\langle k| \otimes \hat{1}_n \right)^\dagger \hat{A} \right\} \hat{\rho}_n(0) \otimes |j\rangle\langle k|, \quad (6)$$

where $\hat{1}_n$ is the unity operator in the nuclear Hilbert space. For example, $\{\sigma_{ab}(t)\}$ may include all N_e^2 electronic reduced density matrix elements (i.e., all populations and coherences), in which case $\{\sigma_{ab}(t)\} \rightarrow \{\sigma_{11}(t), \dots, \sigma_{1N_e}(t), \dots, \sigma_{N_e1}(t), \dots, \sigma_{N_eN_e}(t)\}$; or only the diagonal electronic reduced density matrix elements (i.e., the populations of the corresponding electronic states), in which case $\{\sigma_{ab}(t)\} \rightarrow \{\sigma_{11}(t), \dots, \sigma_{N_eN_e}(t)\}$ or, just the diagonal term describing the time-dependent population of state $|1\rangle$, in which case $\{\sigma_{ab}(t)\} \rightarrow \{\sigma_{11}(t)\}$.

Substituting the projection superoperator \mathcal{P}^{set} into Eq. (5) and tracing over the nuclear and electronic Hilbert spaces, we obtain the following equation of motion for the electronic reduced density matrix elements included in the subset $[\sigma_{jk}(t) \in \{\sigma_{ab}(t)\}]$:

$$\frac{d}{dt}\sigma_{jk}(t) = -\frac{i}{\hbar} \sum_{lm \in \{ab\}} \langle \mathcal{L}_{jk,lm} \rangle_n^0 \sigma_{lm}(t) - \sum_{lm \in \{ab\}} \int_0^t d\tau \mathcal{K}_{jk,lm}^{\text{set}}(\tau) \sigma_{lm}(t - \tau) + I_{jk}^{\text{set}}(t). \quad (7)$$

Here, $\langle \mathcal{L}_{jk,lm} \rangle_n^0$, $\mathcal{K}_{jk,lm}^{\text{set}}(\tau)$, and $I_{jk}^{\text{set}}(t)$ are the matrix elements (jk, lm) of the *projected Liouvillian* superoperator, *memory kernel* superoperator, and *inhomogeneous term* operator, respectively, defined as follows:

$$\langle \mathcal{L}_{jk,lm} \rangle_n^0 = \text{Tr} \left\{ \left(|j\rangle\langle k| \otimes \hat{1}_n \right)^\dagger \mathcal{L} \hat{\rho}_n(0) \otimes |l\rangle\langle m| \right\}, \quad (8)$$

$$\mathcal{K}_{jk,lm}^{\text{set}}(\tau) = \frac{1}{\hbar^2} \text{Tr} \left\{ \left(|j\rangle\langle k| \otimes \hat{1}_n \right)^\dagger \mathcal{L} e^{-i\mathcal{Q}^{\text{set}} \mathcal{L} \tau / \hbar} \mathcal{Q}^{\text{set}} \mathcal{L} \hat{\rho}_n(0) \otimes |l\rangle\langle m| \right\}, \quad (9)$$

and

$$I_{jk}^{\text{set}}(t) = -\frac{i}{\hbar} \text{Tr} \left\{ \left(|j\rangle\langle k| \otimes \hat{1}_n \right)^\dagger \mathcal{L} e^{-i\mathcal{Q}^{\text{set}} \mathcal{L} t / \hbar} \left[\hat{\rho}(0) - \sum_{lm \in \{ab\}} \hat{\rho}_n(0) \otimes |l\rangle\langle m| \sigma_{lm}(0) \right] \right\}. \quad (10)$$

Given that N_{set} is the number of matrix elements of interest included in $\{\sigma_{ab}(t)\}$ ($1 \leq N_{\text{set}} \leq N_e^2$), the projected Liouvillian $\langle \mathcal{L} \rangle_n^0$ and memory kernel $\mathcal{K}^{\text{set}}(\tau)$ superoperators can be represented by $N_{\text{set}} \times N_{\text{set}}$ matrices, whereas the inhomogeneous term operator $\hat{I}^{\text{set}}(t)$ can be represented by an N_{set} -dimensional vector in Liouville space.

Calculating the projected Liouvillian is typically straightforward. The memory kernel and the inhomogeneous term satisfy Volterra integral equations, so they can be obtained from the PFIs.¹⁹ The Volterra equation for the memory kernel is given by

$$\begin{aligned} \mathcal{K}_{jk,lm}^{\text{set}}(\tau) &= i \dot{\mathcal{F}}_{jk,lm}(\tau) - \frac{1}{\hbar} \sum_{uv \in \{ab\}} \mathcal{F}_{jk,uv}(\tau) \langle \mathcal{L}_{uv,lm} \rangle_n^0 \\ &+ i \sum_{uv \in \{ab\}} \int_0^\tau d\tau' \mathcal{F}_{jk,uv}(\tau - \tau') \mathcal{K}_{uv,lm}^{\text{set}}(\tau'), \end{aligned} \quad (11)$$

where the PFIs are given by

$$\begin{aligned} \mathcal{F}_{jk,lm}(\tau) &= \frac{1}{\hbar} \text{Tr} \left\{ \left(|j\rangle\langle k| \otimes \hat{1}_n \right)^\dagger \mathcal{L} e^{-i\mathcal{L}\tau/\hbar} \hat{\rho}_n(0) \otimes |l\rangle\langle m| \right\}, \\ \dot{\mathcal{F}}_{jk,lm}(\tau) &= -\frac{i}{\hbar^2} \text{Tr} \left\{ \left(|j\rangle\langle k| \otimes \hat{1}_n \right)^\dagger \mathcal{L} e^{-i\mathcal{L}\tau/\hbar} \mathcal{L} \hat{\rho}_n(0) \otimes |l\rangle\langle m| \right\}. \end{aligned} \quad (12)$$

The Volterra equation for the inhomogeneous term is given by

$$I_{jk}^{\text{set}}(t) = Z_{jk}(t) + i \sum_{lm \in \{ab\}} \mathcal{F}_{jk,lm}(t) \sigma_{lm}(0) + i \sum_{uv \in \{ab\}} \int_0^t d\tau \mathcal{F}_{jk,uv}(t - \tau) I_{uv}^{\text{set}}(\tau), \quad (13)$$

where the additional PFI $Z_{jk}(t)$ is given by

$$Z_{jk}(t) = -\frac{i}{\hbar} \text{Tr} \left\{ \left(|j\rangle\langle k| \otimes \hat{1}_n \right)^\dagger \mathcal{L} e^{-i\mathcal{L}t/\hbar} \hat{\rho}(0) \right\}. \quad (14)$$

It should be noted that $Z_{jk}(t) = -i\mathcal{F}_{jk,\gamma\gamma}(t)$ when the overall initial state is of the commonly encountered form $\hat{\rho}(0) = \hat{\rho}_n(0) \otimes |\gamma\rangle\langle\gamma|$ (where $|\gamma\rangle$ is one of the electronic basis states), as is the case for the applications reported in this paper. A more detailed discussion of the derivation, properties, and significance of Eqs. (11)-(14) can be found in Ref. 19 and the SI.

Most previous studies have been based on direct calculations of the aforementioned PFIs.^{19,43,43-46} However, when using an exact input method, the PFIs can also be accurately obtained as derivatives of the propagator $\mathcal{U}(\tau) \equiv \text{Tr}_n \{ e^{-i\mathcal{L}\tau/\hbar} \hat{\rho}_n(0) \otimes \hat{1}_e \}$ that evolves the electronic reduced density operator, as follows:^{41,43}

$$\hat{\sigma}(\tau) = \mathcal{U}(\tau)\hat{\sigma}(0), \quad (15)$$

with matrix elements,

$$\mathcal{U}_{jk,lm}(\tau) = \text{Tr} \left\{ \left(|j\rangle\langle k| \otimes \hat{1}_n \right)^\dagger e^{-i\mathcal{L}\tau/\hbar} \hat{\rho}_n(0) \otimes |l\rangle\langle m| \right\}. \quad (16)$$

Specifically, we obtain the PFIs $\left\{ \mathcal{F}_{jk,lm}(\tau), \dot{\mathcal{F}}_{jk,lm}(\tau) \right\}$ from $\{ \mathcal{U}_{jk,lm}(\tau) \}$, as follows:^{41,43}

$$\mathcal{F}_{jk,lm}(\tau) = i\dot{\mathcal{U}}_{jk,lm}(\tau), \quad \dot{\mathcal{F}}_{jk,lm}(\tau) = i\ddot{\mathcal{U}}_{jk,lm}(\tau). \quad (17)$$

PFIs $\left\{ \mathcal{F}_{jk,lm}(\tau), \dot{\mathcal{F}}_{jk,lm}(\tau) \right\}$ obtained from $\mathcal{U}(\tau)$ generate exact memory kernels and inhomogeneous terms when $\mathcal{U}(\tau)$ is obtained from exact inputs. Therefore, we obtain them in terms of numerical derivatives of $\mathcal{U}(\tau)$ obtained from TT-TFD simulations, as described in Sec. 4.

4 Tensor-Train Thermo-Field Dynamics

4.1 Hamiltonian

The molecular Hamiltonian introduced by Eq. (1) can also be written as a sum of a purely electronic Hamiltonian $\hat{H}_e \otimes \hat{1}_n$ plus a purely nuclear Hamiltonian $\hat{1}_e \otimes \hat{H}_n$ and an interaction term between the electronic and nuclear DOF, \hat{H}_{en} :

$$\hat{H} = \hat{H}_e \otimes \hat{1}_n + \hat{1}_e \otimes \hat{H}_n + \hat{H}_{en}. \quad (18)$$

It should be noted that this division is not unique, in the sense that different choices of \hat{H}_e , \hat{H}_n , and \hat{H}_{en} are possible.⁴³ However, the results are invariant to those choices when a quantum-mechanically exact method like TT-TFD is applied since no physical or *ad hoc* approximation is introduced.

4.2 Thermo-field dynamics method

We start out by noting that the dynamics of $\hat{\rho}(t)$ governed by the Hamiltonian of the form of Eq. (18) is described by the quantum Liouville equation,

$$\frac{d}{dt}\hat{\rho}(t) = -\frac{i}{\hbar}[\hat{H}, \hat{\rho}(t)]. \quad (19)$$

The TT-TFD method^{53,54,56,57} provides a general, numerically exact approach to solve Eq. (19) that is particularly efficient when $\hat{\rho}(t)$ can be represented as a low rank matrix product state. In our simulations, the state is described by $\hat{\rho}^{1/2}(t)$ (instead of $\hat{\rho}(t)$), represented as a tensor-train vector in an extended Hilbert space (the so-called double Hilbert space described below). The Liouville equation given in Eq. (19) is replaced by an equivalent equation of motion for $\hat{\rho}^{1/2}(t)$, which can be written in the form of a Schrödinger-like equation in the double Hilbert space. For a high-dimensional system, computational efficiency is

achieved by using a tensor-train representation^{26,58–64} of the extended state vector $\hat{\rho}^{1/2}(t)$. The remainder of this section outlines the TT-TFD methodology used for calculating the PFIs needed to obtain the memory kernel and inhomogeneous term of the GQMEs.

The initial density operator of the overall system is of the form introduced by Eq. (2). The initial electronic density operator is given by $\hat{\sigma}(0) = |\gamma\rangle\langle\gamma|$, where $|\gamma\rangle$ is one of the electronic basis states, while the initial nuclear density operator is $\hat{\rho}_n(0) = e^{-\beta\hat{H}_n}/Z_n(\beta)$, where $Z_n(\beta) = \text{Tr}_n\{e^{-\beta H_n}\}$. Therefore,

$$\hat{\rho}(0) = |\gamma\rangle\langle\gamma| \otimes \frac{e^{-\beta\hat{H}_n}}{Z_n(\beta)}. \quad (20)$$

We note, however, that the TT-TFD method is not restricted to initial states of this simple form and can be analogously applied to propagate any arbitrary initial state.

The TFD representation is only applied to the nuclear density operator of the system since the same dynamics is obtained for the initial state introduced by Eq. (20) regardless of whether the electronic density operator is included or not in the TFD representation.⁵⁶ We let $\{|k\rangle\}$ be an orthonormal basis that spans the *physical* nuclear Hilbert space \mathcal{H}_n and $\{|\tilde{k}\rangle\}$ an orthonormal basis that spans a *fictitious* nuclear Hilbert space (also known as the tilde space) $\tilde{\mathcal{H}}_n$, which is an exact replica of \mathcal{H}_n . Next, we define the so-called *nuclear thermal vacuum state*:

$$|0_n(\beta)\rangle = \frac{e^{-\beta\hat{H}_n/2}}{\sqrt{Z(\beta)}} \sum_{\tilde{k}=k} |k\rangle \otimes |\tilde{k}\rangle, \quad (21)$$

where it should be noted that the sum includes only terms $|k\rangle \otimes |\tilde{k}\rangle$ with $\tilde{k} = k$, so that $\sum_{\tilde{k}=k} |k\rangle \otimes |\tilde{k}\rangle = |0\rangle \otimes |\tilde{0}\rangle + |1\rangle \otimes |\tilde{1}\rangle + \dots$. We note that $\hat{\rho}_n(0)$ can be obtained from $|0_n(\beta)\rangle$, upon taking the outer product with its dual and tracing out the fictional degrees of freedom as follows:

$$\text{Tr}_f\{|0_n(\beta)\rangle\langle 0_n(\beta)|\} = \hat{\rho}_n(0), \quad (22)$$

where $\text{Tr}_f\{\cdot\}$ is the partial trace over states $|\tilde{k}\rangle$ in the tilde space $\tilde{\mathcal{H}}_n$.

Substituting Eq. (22) into Eq. (20), we obtain the initial density operator of the overall system $\hat{\rho}(0)$ represented in terms of the ket vector $|\psi_\gamma(\beta, 0)\rangle \equiv |\gamma\rangle \otimes |0_n(\beta)\rangle$, as follows:

$$\hat{\rho}(0) = \text{Tr}_f \left\{ |\psi_\gamma(\beta, 0)\rangle \langle \psi_\gamma(\beta, 0)| \right\}. \quad (23)$$

Note that in Eq. (23), only the initially thermalized nuclear density operator is represented by a ket vector in the double space $\mathcal{H}_n \otimes \tilde{\mathcal{H}}_n$; whereas the initial electronic density operator $|\gamma\rangle \langle \gamma|$ corresponds to a pure state in the electronic Hilbert space.

We define the overall system ket vector $|\psi_\gamma(\beta, t)\rangle$ such that

$$\hat{\rho}(t) = \text{Tr}_f \left\{ |\psi_\gamma(\beta, t)\rangle \langle \psi_\gamma(\beta, t)| \right\}, \quad (24)$$

where $\hat{\rho}(t)$ evolves according to the Liouville equation Eq. (19). This can be fulfilled by evolving $|\psi_\gamma(\beta, t)\rangle$ according to the so-called TFD Schrödinger equation (as shown in the SI),

$$\frac{d}{dt} |\psi_\gamma(\beta, t)\rangle = -\frac{i}{\hbar} \bar{H} |\psi_\gamma(\beta, t)\rangle, \quad (25)$$

where $\bar{H} = \hat{H} \otimes \tilde{\mathbf{1}}_n$, with $\tilde{\mathbf{1}}_n = \sum_{\tilde{k}} |\tilde{k}\rangle \langle \tilde{k}|$ the identity operator of the tilde space. Moreover, we note that the same physical system dynamics can be obtained by defining \bar{H} in Eq. (25), as follows:

$$\bar{H} = \hat{H} \otimes \tilde{\mathbf{1}}_n - \hat{\mathbf{1}} \otimes \tilde{H}_n, \quad (26)$$

where $\hat{\mathbf{1}} = \hat{\mathbf{1}}_n \otimes \hat{\mathbf{1}}_e$. Remarkably, \tilde{H}_n can be *any* operator in the nuclear tilde space since \tilde{H}_n does not impact kets in the physical space and its effect on the dynamics vanishes upon taking the partial trace over states in the tilde space.⁵⁶

The preparation of the initial thermal wavepacket $|\psi_\gamma(\beta, 0)\rangle$, according to Eqs. (22) and (21), requires the explicit evaluation of the quantum Boltzmann operator, which can be computationally challenging for systems with high dimensionality. However, when the initial nuclear Hamiltonian is harmonic, the initial thermal wavepacket can be obtained by

taking advantage of the *thermal Bogoliubov transformation*. Therefore, we can generate the nuclear thermal vacuum state from the double space ground state $|0_n, \tilde{0}_n\rangle$ using the following unitary transformation,

$$|\psi_\gamma(\beta, 0)\rangle = |\gamma\rangle \otimes e^{-i\hat{G}}|0_n, \tilde{0}_n\rangle, \quad (27)$$

where \hat{G} is given by: [53,54,65](#)

$$\hat{G} = -i \sum_j \theta_j (\hat{a}_j \tilde{a}_j - \hat{a}_j^\dagger \tilde{a}_j^\dagger), \quad (28)$$

with $\theta_j = \text{arctanh}(e^{-\beta\omega_j/2})$, where $\{\hat{a}_j, \hat{a}_j^\dagger\}$ and $\{\tilde{a}_j, \tilde{a}_j^\dagger\}$ are the creation and annihilation operators associated with the j -th nuclear DOF in the physical and tilde Hilbert spaces, respectively.

Substituting Eqs. (27) and (28) into Eq. (25) we obtain:

$$\frac{d}{dt} |\psi_{\theta,\gamma}(\beta, t)\rangle = -\frac{i}{\hbar} \bar{H}_\theta |\psi_{\theta,\gamma}(\beta, t)\rangle, \quad (29)$$

with $|\psi_{\theta,\gamma}(\beta, 0)\rangle = |\gamma\rangle \otimes |0, \tilde{0}\rangle$, $|\psi_{\theta,\gamma}(\beta, t)\rangle = e^{i\hat{G}} |\psi_\gamma(\beta, t)\rangle$, and \bar{H}_θ is defined as:

$$\bar{H}_\theta = e^{i\hat{G}} \bar{H} e^{-i\hat{G}}. \quad (30)$$

The time-dependent thermal state $|\psi_{\theta,\gamma}(\beta, t)\rangle$ is represented as:

$$|\psi_{\theta,\gamma}(\beta, t)\rangle = \sum_{j_1, \dots, j_d}^{n_1, \dots, n_d} X(\beta, t; j_1, \dots, j_d) |j_1\rangle \otimes \dots \otimes |j_d\rangle, \quad (31)$$

where $d = 1 + 2N_n$ is the overall number of DOF and $\{|j_k\rangle\}$ is the basis set with $k = 1, \dots, d$. We determined the size of the basis according to the convergence test, including two electronic state eigenvectors and the 10 nuclear harmonic eigenvectors for the nuclear DOF.

The time- and temperature-dependent expansion coefficients $\{X(\beta, t; j_1, \dots, j_d)\}$ correspond to an $n_1 \times \dots \times n_d$ complex array which requires storage space and computational effort that grows exponentially with d . Thus, we avoid the curse of dimensionality by imple-

menting the TFD wavepacket in the tensor-train (TT) format.^{26,58–64}

4.3 TT Format

The TT format of $X \in \mathbb{C}^{n_1 \times \dots \times n_d}$ involves a train-like product of d tensor cores which are 3-mode tensors $X_i \in \mathbb{C}^{r_{i-1} \times n_i \times r_i}$, with $r_0 = r_d = 1$. Any particular element $X(j_1, \dots, j_d)$ can be evaluated by multiplication of the cores, as follows:

$$X(j_1, \dots, j_d) = \sum_{a_0=1}^{r_0} \sum_{a_1=1}^{r_1} \dots \sum_{a_d=1}^{r_d} X_1(a_0, j_1, a_1) X_2(a_1, j_2, a_2) \dots X_d(a_{d-1}, j_d, a_d). \quad (32)$$

This can also be written in compact matrix product notation, as follows:

$$X(j_1, \dots, j_d) = \mathbf{X}_1(j_1) \mathbf{X}_2(j_2) \dots \mathbf{X}_d(j_d), \quad (33)$$

with matrix $\mathbf{X}_i(j_i) \in \mathbb{C}^{r_{i-1} \times r_i}$ defining the j_i^{th} slice of X_i .

The central idea of the TT format is to generalize the concept of factorization. Each physical dimension i is factorized as an individual core (i.e., X_i). Entanglement with other physical dimensions is established through the auxiliary indices a_{i-1} and a_i . The TT-ranks r_0, \dots, r_d introduced by Eq. (32) remain small for a low level of entanglement and when they are $r_0 = \dots = r_d = 1$, the TT format of X is a factorizable product.

Eq. (32) shows that the TT format allows for compressed representations of X since it requires storage of X_1, \dots, X_d , with $dn\tilde{r}^2$ elements when $r_1 = \dots = r_{d-1} = \tilde{r}$ and $n_1 = \dots = n_d = n$. For small \tilde{r} , such a representation bypasses the need to explicitly store all n^d elements of X , thus offering an exponential advantage in storage and computational effort.

In TT-TFD, the initial state $|\psi_{\theta,\gamma}(\beta, 0)\rangle = |\gamma\rangle \otimes |0, \tilde{0}\rangle$ takes an initial single-product form and is prepared as a rank-1 tensor train. The transformed TFD Schrödinger equation is then solved with the TT-KSL method.^{66,67} The TT-KSL propagator evolves the wavepacket according to the time-dependent variational principle (TDVP) by evolving the time-dependent

state on a fixed-rank TT manifold. Comparisons to other TT propagators have shown that TT-KSL is quite accurate and efficient.^{62,68}

4.4 Projection-free inputs from TT-TFD

The PFIs required for calculating the memory kernel and inhomogeneous term of the GQME are computed by using the TT-TFD methodology. According to Eq. (16), the matrix elements $\mathcal{U}_{jk,lm}(\tau)$ are obtained, as follows:

$$\mathcal{U}_{jk,lm}(\tau) = \text{Tr}_{e,n} \left\{ e^{-i\hat{H}\tau/\hbar} \hat{\rho}_n(0) |l\rangle\langle m| e^{i\hat{H}\tau/\hbar} (|k\rangle\langle j| \otimes \hat{1}_n) \right\}. \quad (34)$$

Since TT-TFD requires an initial electronic state that is in a pure state $|\gamma\rangle$, in the following we write $|l\rangle\langle m|$ as $|\gamma\rangle\langle\gamma|$; however, we note that all $\mathcal{U}(\tau)$ elements with off-diagonal initial electronic density matrices can be expressed as linear combinations of pure-state populations (see the SI).

With Eqs. (27) and (29), we use $|k\rangle\langle j|j\rangle\langle j| = |k\rangle\langle j|$ to rewrite $\mathcal{U}_{jk,\gamma\gamma}(\tau)$ as

$$\begin{aligned} \mathcal{U}_{jk,\gamma\gamma}(\tau) &= \text{Tr}_{e,n} \left\{ e^{-i\hat{H}\tau/\hbar} \hat{\rho}_n(0) |\gamma\rangle\langle\gamma| e^{i\hat{H}\tau/\hbar} (|k\rangle\langle j| \otimes \hat{1}_n) \right\} \\ &= \text{Tr}_{e,n} \left\{ e^{-i\hat{H}\tau/\hbar} \hat{\rho}_n(0) |\gamma\rangle\langle\gamma| e^{i\hat{H}\tau/\hbar} (|k\rangle\langle j| \otimes \hat{1}_n) (|j\rangle\langle j| \otimes \hat{1}_n) \right\}. \end{aligned} \quad (35)$$

From this equation, noting that $\text{Tr}_f \left\{ |\psi_\gamma(\beta, \tau)\rangle\langle\psi_\gamma(\beta, \tau)| \right\} = e^{-i\hat{H}\tau/\hbar} \hat{\rho}_n(0) |\gamma\rangle\langle\gamma| e^{i\hat{H}\tau/\hbar}$, we perform a cyclic permutation to obtain

$$\mathcal{U}_{jk,\gamma\gamma}(\tau) = \text{Tr}_{e,n} \left\{ \text{Tr}_f \left\{ (|j\rangle\langle j| \otimes \hat{1}_n) |\psi_\gamma(\beta, t)\rangle\langle\psi_\gamma(\beta, \tau)| (|k\rangle\langle j| \otimes \hat{1}_n) \right\} \right\}. \quad (36)$$

From here, we use $|\psi_{jk,\gamma\gamma}(\tau)\rangle = (|k\rangle\langle j| \otimes \hat{1}_n) |\psi_\gamma(\beta, \tau)\rangle$ and $|\psi_{\theta,jk\gamma\gamma}(\tau)\rangle = e^{iG} |\psi_{jk,\gamma\gamma}(\tau)\rangle =$

$(|k\rangle\langle j| \otimes \hat{1}_n)|\psi_{\gamma,\theta}(\beta, \tau)\rangle$ to obtain,

$$\begin{aligned}
\mathcal{U}_{jk,\gamma\gamma}(\tau) &= \text{Tr}_{e,n,f} \left\{ |\psi_{jj,\gamma\gamma}(\beta, \tau)\rangle\langle\psi_{jk,\gamma\gamma}(\beta, \tau)| \right\}, \\
&= \langle\psi_{jj,\gamma\gamma}(\tau)|\psi_{jk,\gamma\gamma}(\tau)\rangle, \\
&= \langle\psi_{\theta,jj\gamma\gamma}(\tau)|\psi_{\theta,jk\gamma\gamma}(\tau)\rangle,
\end{aligned}
\tag{37}$$

which provides the elements of $\mathcal{U}(\tau)$ after obtaining $|\psi_{\gamma,\theta}(\beta, \tau)\rangle$ by integrating Eq. (29).

5 Applications

In this section, we report simulations of electronic population dynamics based on four types of GQMEs. The equations correspond to different subsets of electronic reduced density matrix elements used to describe the underlying dynamics (see Sec. 3). As described in Sec. 4, the memory kernels and inhomogeneous terms are calculated from PFIs obtained via the quantum-mechanically exact TT-TFD method (see Sec. 4) as applied to five different realizations of a benchmark spin-boson model Hamiltonian. We also compare the quantum-mechanically exact memory kernels and inhomogeneous terms obtained with TT-TFD inputs to calculations based on an approximate linearized semiclassical (LSC) method.¹⁹

The reduced electronic density matrix for the spin-boson model, introduced in Sec. 5.1, consists of four matrix elements, $\{\sigma_{DD}, \sigma_{DA}, \sigma_{AD}, \sigma_{AA}\}$, where $|D\rangle$ and $|A\rangle$ correspond to the *donor* and *acceptor* electronic states, respectively. We consider GQMEs for the following four subsets of matrix elements: (1) $\{\sigma_{DD}, \sigma_{DA}, \sigma_{AD}, \sigma_{AA}\}$ (the full density matrix); (2) $\{\sigma_{DD}, \sigma_{AA}\}$ (the populations-only subset); (3) $\{\sigma_{DD}\}$ (the donor single-population subset); and (4) $\{\sigma_{AA}\}$ (the acceptor single-population subset). The TT-TFD-based PFIs, obtained by taking numerical derivatives of the time evolution operator $\mathcal{U}(\tau)$ [see Eq. (16)], are compared to PFIs obtained via an LSC-based method denoted LSCII [sometimes also referred to as the LSC initial value representation (LSC-IVR) method⁶⁹]. Ref. 44 provides a detailed discussion of the protocols used for calculating PFIs via LSCII.

5.1 Spin-Boson Models

The spin-boson model provides a useful framework for studying molecular systems where the dynamics involves two coupled electronic states. In the simplest form, the electronic coupling is independent of the nuclear coordinates (the so-called Condon approximation). The nuclear motion in each electronic state is described by harmonic potential energy surfaces (PESs) with distinct equilibrium energies and equilibrium positions. As such, the spin-boson model has been widely used for describing a wide range of chemical dynamical processes, including charge and energy transfer (e.g., Marcus theory), nonadiabatic dynamics, photochemistry, spin energy relaxation and dephasing, vibrational energy relaxation, and, more recently, polaritonic chemistry where the photonic DOF can be described as harmonic oscillators and therefore grouped with the nuclear DOF.^{13–16,70}

The spin-boson Hamiltonian is defined according to Eq. (1) with $\{\hat{H}_j\}$ and $\{\hat{V}_{jk} \rightarrow V_{jk}\}$ defined, as follows:

$$\begin{aligned}\hat{H}_1 &\equiv \hat{H}_D = \epsilon + \sum_{k=1}^{N_n} \frac{\hat{P}_k^2}{2} + \frac{1}{2}\omega_k^2 \hat{R}_k^2 - c_k \hat{R}_k, \\ \hat{H}_2 &\equiv \hat{H}_A = -\epsilon + \sum_{k=1}^{N_n} \frac{\hat{P}_k^2}{2} + \frac{1}{2}\omega_k^2 \hat{R}_k^2 + c_k \hat{R}_k, \\ V_{12} &\equiv V_{DA} = V_{21} \equiv V_{AD} = \Gamma.\end{aligned}\tag{38}$$

Here, 2ϵ is the energy difference between the donor (D) and acceptor (A) states with nuclear coordinates at equilibrium, and the electronic coupling between donor and acceptor states is defined by the positive constant Γ (Condon approximation).

The frequencies $\{\omega_k\}$ and electron-phonon coupling coefficients, $\{c_k\}$ of the nuclear modes are sampled from an Ohmic spectral density with an exponential cutoff:

$$J(\omega) = \frac{\pi}{2} \sum_{k=1}^{N_n} \frac{c_k^2}{\omega_k} \delta(\omega - \omega_k) \xrightarrow{N_n \rightarrow \infty} \frac{\pi \hbar}{2} \xi \omega e^{-\omega/\omega_c}.\tag{39}$$

Here, ξ is the Kondo parameter, which determines the electron-phonon coupling strength, and ω_c is the cutoff frequency which determines the characteristic vibrational frequency. A discrete set of N_n nuclear mode frequencies, $\{\omega_k\}$, and coupling coefficients, $\{c_k\}$, are sampled from the spectral density, introduced by Eq. (39).⁴³ The Hamiltonian introduced by Eqs. (1) and (38) can be rewritten in terms of the harmonic oscillator raising and lowering operators, as follows:

$$\hat{H} = \epsilon \hat{\sigma}_z + \Gamma \hat{\sigma}_x + \sum_{k=1}^{N_n} \omega_k \hat{a}_k^\dagger \hat{a}_k - \sigma_z \frac{c_k}{\sqrt{2\omega_k}} (\hat{a}_k + \hat{a}_k^\dagger). \quad (40)$$

The corresponding rotated double space Hamiltonian \bar{H}_θ introduced by Eq. (30) can then be obtained in closed form, as follows:^{54,71}

$$\bar{H}_\theta = \epsilon \hat{\sigma}_z + \Gamma \hat{\sigma}_x + \sum_{k=1}^{N_n} \omega_k (\hat{a}_k^\dagger \hat{a}_k - \tilde{a}_k^\dagger \tilde{a}_k) - \frac{\sigma_z c_k}{\sqrt{2\omega_k}} \left((\hat{a}_k + \hat{a}_k^\dagger) \cosh(\theta_k) + (\tilde{a}_k + \tilde{a}_k^\dagger) \sinh(\theta_k) \right), \quad (41)$$

where $\hat{\sigma}_x$ and $\hat{\sigma}_z$ are the x - and z -Pauli matrices. Using Eq. (41) in place of the mathematically equivalent Eq. (30) facilitates the implementation of TT-TFD by avoiding the need to calculate $e^{i\hat{G}}$ and $e^{-i\hat{G}}$ numerically.

The initial state is defined according to Eq. (2) with the initial electronic state $\hat{\sigma}(0) = |D\rangle\langle D|$ and the initial nuclear state:

$$\hat{\rho}_n(0) = \frac{e^{-\beta(\hat{H}_D + \hat{H}_A)/2}}{\text{Tr}_n \left\{ e^{-\beta(\hat{H}_D + \hat{H}_A)/2} \right\}}. \quad (42)$$

Five different models are analyzed, as defined by the sets of parameters listed in Table 1, corresponding to models 1, 2, 3, 4, and 6 of Refs. 43, 44, and 19. Model 5 was not included because the reference exact results are known only for short final times compared to the lifetime of the electronic relaxation dynamics. Models 1-3 correspond to systems with a finite energy bias between the donor and acceptor states ($\epsilon = 1.0$), differing with respect to the value of ω_c . Model 4 corresponds to a biased system ($\epsilon = 1.0$) with a higher Kondo parameter

($\xi = 0.4$) relative to models 1-3 ($\xi = 0.1$). Model 6 corresponds to a unbiased system ($\epsilon = 0.0$). All results are obtained using an integration time step $\Delta t = 1.50083 \times 10^{-3} \Gamma^{-1}$. Quantum-mechanically exact QuAPI results for models 1-4 are from Ref. 39, and for model 6 from Ref. 35.

Table 1: **Spin-Boson Model and Simulation Parameters**

Model #	Model Parameters					Numerical Parameters		
	ϵ	Γ	β	ξ	ω_c	ω_{\max}	N_n	Δt
1	1.0	1.0	5.0	0.1	1.0	5	60	1.50083×10^{-3}
2	1.0	1.0	5.0	0.1	2.0	10	60	1.50083×10^{-3}
3	1.0	1.0	5.0	0.1	7.5	36	60	1.50083×10^{-3}
4	1.0	1.0	5.0	0.4	2.0	10	60	1.50083×10^{-3}
6	0.0	1.0	5.0	0.2	2.5	12	60	1.50083×10^{-3}

5.2 GQMEs

The following subsections outline four types of GQMEs examined by our simulations, corresponding to the analysis of quantum dynamics for different subsets of electronic reduced density matrix elements.

5.2.1 Full Set: GQME for All Electronic Density Matrix Elements

Here, we consider the GQME when the quantities of interest include all four reduced electronic density matrix elements, $\{\sigma_{ab}(t)\} = \{\sigma_{DD}(t), \sigma_{DA}(t), \sigma_{AD}(t), \sigma_{AA}(t)\}$:

$$\frac{d}{dt}\sigma_{jk}(t) = -\frac{i}{\hbar} \sum_{l,m=1}^{N_e=2} \langle \mathcal{L}_{jk,lm} \rangle_n^0 \sigma_{lm}(t) - \sum_{l,m=1}^{N_e=2} \int_0^t d\tau \mathcal{K}_{jk,lm}^{\text{full}}(\tau) \sigma_{lm}(t - \tau), \quad (43)$$

where $jk \in \{DD, DA, AD, AA\}$. The memory kernel superoperator $\mathcal{K}^{\text{full}}(\tau)$ is represented by an $N_e^2 \times N_e^2 = 4 \times 4$ time-dependent matrix whose matrix elements are obtained by solving

the following Volterra equation:

$$\mathcal{K}_{jk,lm}^{\text{full}}(\tau) = i\dot{\mathcal{F}}_{jk,lm}(\tau) - \frac{1}{\hbar} \sum_{u,v=1}^{N_e=2} \mathcal{F}_{jk,uv}(\tau) \langle \mathcal{L}_{uv,lm} \rangle_n^0 + i \sum_{u,v=1}^{N_e=2} \int_0^\tau d\tau' \mathcal{F}_{jk,uv}(\tau - \tau') \mathcal{K}_{uv,lm}^{\text{full}}(\tau'), \quad (44)$$

where the PFIs $\{\mathcal{F}_{jk,lm}(\tau)\}$ and $\{\dot{\mathcal{F}}_{jk,lm}(\tau)\}$ are introduced by Eq. (12).

5.2.2 Populations-Only: GQME for Diagonal Elements of the Reduced Electronic Density Matrix

Here, we consider the GQME for the quantities of interest that includes only the diagonal matrix elements of the reduced electronic density matrix (i.e., the populations-only GQME), such that $\{\sigma_{ab}(t)\} = \{\sigma_{DD}(t), \sigma_{AA}(t)\}$:

$$\frac{d}{dt} \sigma_{jj}(t) = - \sum_{k=1}^{N_e=2} \int_0^t d\tau \mathcal{K}_{jj,kk}^{\text{POP}}(\tau) \sigma_{kk}(t - \tau), \quad (45)$$

where $j \in \{D, A\}$. The memory kernel superoperator $\mathcal{K}^{\text{POP}}(\tau)$ is represented by an $N_e \times N_e = 2 \times 2$ time-dependent matrix, with individual matrix elements obtained by solving the following Volterra equation:

$$\mathcal{K}_{jj,kk}^{\text{POP}}(\tau) = i\dot{\mathcal{F}}_{jj,kk}(\tau) + i \sum_{\lambda=1}^{N_e} \int_0^\tau d\tau' \mathcal{F}_{jj,\lambda\lambda}(\tau - \tau') \mathcal{K}_{\lambda\lambda,kk}^{\text{POP}}(\tau'), \quad (46)$$

where the PFIs $\{\mathcal{F}_{jj,kk}(\tau)\}$ and $\{\dot{\mathcal{F}}_{jj,kk}(\tau)\}$ are introduced by Eq. (12).

5.2.3 Single-Population Scalar: GQMEs for One Diagonal Element of the Reduced Electronic Density Matrix

Finally, we consider the two single-population scalar GQMEs for the case where the subset includes either only the population of the donor state (σ_{DD}) or only the population of the

acceptor state (σ_{AA}), such that $\{\sigma_{ab}(t)\} = \{\sigma_{DD}(t)\}$ or $\{\sigma_{ab}(t)\} = \{\sigma_{AA}(t)\}$, respectively:

$$\frac{d}{dt}\sigma_{DD}(t) = -\int_0^t d\tau \mathcal{K}_{DD,DD}^{\text{donor}}(\tau)\sigma_{DD}(t-\tau), \quad (47)$$

$$\frac{d}{dt}\sigma_{AA}(t) = -\int_0^t d\tau \mathcal{K}_{AA,AA}^{\text{acceptor}}(\tau)\sigma_{AA}(t-\tau) + I_{AA}^{\text{acceptor}}(t). \quad (48)$$

It should be noted that the inhomogeneous term does not vanish in the case where $\{\sigma_{ab}(t)\} = \{\sigma_{AA}(t)\}$. It should also be noted that the memory kernels $\mathcal{K}_{DD,DD}^{\text{donor}}(\tau)$ and $\mathcal{K}_{AA,AA}^{\text{acceptor}}(\tau)$, as well the inhomogeneous term $I_{AA}^{\text{acceptor}}(t)$, are scalar in this case and can be obtained by solving the following Volterra equations:

$$\mathcal{K}_{DD,DD}^{\text{donor}}(\tau) = i\dot{\mathcal{F}}_{DD,DD}(\tau) + i\int_0^\tau d\tau' \mathcal{F}_{DD,DD}(\tau-\tau')\mathcal{K}_{DD,DD}^{\text{donor}}(\tau'), \quad (49)$$

$$\mathcal{K}_{AA,AA}^{\text{acceptor}}(\tau) = i\dot{\mathcal{F}}_{AA,AA}(\tau) + i\int_0^\tau d\tau' \mathcal{F}_{AA,AA}(\tau-\tau')\mathcal{K}_{AA,AA}^{\text{acceptor}}(\tau'), \quad (50)$$

$$I_{AA}^{\text{acceptor}}(t) = -i\mathcal{F}_{AA,DD}(t) + i\int_0^t d\tau \mathcal{F}_{AA,AA}(t-\tau)I_{AA}^{\text{acceptor}}(\tau), \quad (51)$$

where the PFIs $\mathcal{F}_{DD,DD}$, $\mathcal{F}_{AA,AA}$, $\dot{\mathcal{F}}_{DD,DD}$, $\dot{\mathcal{F}}_{AA,AA}$, and $\mathcal{F}_{AA,DD}(\tau)$ are defined by Eq. (12).

5.3 Input Methods

It is important to note that the four types of GQMEs, outlined in the previous subsections, call for the same input of PFIs defined by Eq. (12). The different types of GQMEs differ only with respect to the specific matrix elements of $\mathcal{F}(\tau)$ and $\dot{\mathcal{F}}(\tau)$ that are required to calculate the memory kernel and inhomogeneous term. For example, calculating the memory kernel for evolving the full set of reduced density matrix elements according to Eq. (43) requires calculating all 16 matrix elements of $\mathcal{F}(\tau)$ and $\dot{\mathcal{F}}(\tau)$. In contrast, calculating the memory kernel of the donor single-population GQME, Eq. (47), requires only a single matrix element of each of the matrices representing $\mathcal{F}(\tau)$ and $\dot{\mathcal{F}}(\tau)$.

The matrix elements of $\mathcal{F}(\tau)$ and $\dot{\mathcal{F}}(\tau)$ can be determined using a wide range of numerically exact or approximate propagation methods. Since the matrix elements of $\mathcal{F}(\tau)$ and

$\dot{\mathcal{F}}(\tau)$ are given in terms of two-time correlation functions of the overall-system,¹⁹ the only requirement for a propagation method is that it should be able to calculate such quantities, either exactly or approximately.

In this paper, we compare and contrast two input methods: the quantum-mechanically exact TT-TFD method described in Sec. 4 and the approximate semiclassical LSCII method, previously described in Ref. 19. The inclusion of the LSCII input method is done for the sake of comparison between the memory kernels and inhomogeneous terms as obtained from an approximate input method with those obtained via an exact input method, with the intent of exploring the main sources of inaccuracy when approximate input methods are used.

For the LSCII method, we calculate $\mathcal{F}_{jk,lm}(\tau)$ and $\dot{\mathcal{F}}_{jk,lm}(\tau)$ directly as described in Ref. 19. For the TT-TFD method, we calculate the $N_e^2 \times N_e^2$ elements of the time evolution operator of the electronic reduced density matrix $\mathcal{U}(\tau)$ introduced by Eq. (16). Then, $\mathcal{F}_{jk,lm}(\tau)$ and $\dot{\mathcal{F}}_{jk,lm}(\tau)$ are obtained from numerical derivatives according to Eq. (17). For the results given in this paper, the numerical derivatives were calculated using the second-order finite central difference method available in the NumPy Python library.

Once the PFIs have been obtained with either TT-TFD or LSCII propagation, the memory kernels and inhomogeneous terms of the GQMEs are calculated via an iterative algorithm that solves the corresponding Volterra equation [see Eqs. (44), (46), (49), (50), and (51)].^{19,43} The different types of GQMEs [see Eqs. (43), (45), (47), and (48)] are then solved numerically for the electronic density matrix elements via a Runge-Kutta fourth-order (RK4) algorithm.

5.4 Results

Figs. 1-5 compare the time-dependent $\sigma_z(t) = \sigma_{DD}(t) - \sigma_{AA}(t)$, showing the differences of electronic populations for the five realizations of the spin-boson model outlined in Sec. 5.1 (see Table 1). These results are obtained by using the four different types of GQMEs outlined in Sec. 5.2, with PFIs computed with the TT-TFD method as described in Sec. 4. These results provide a clear demonstration of the rather remarkable fact that *all four GQMEs*

correspond to exact equations of motion for the electronic populations and thereby reproduce the same exact population dynamics when a quantum-mechanically exact input method like TT-TFD is used even though they are quite different in form and dimensionality.

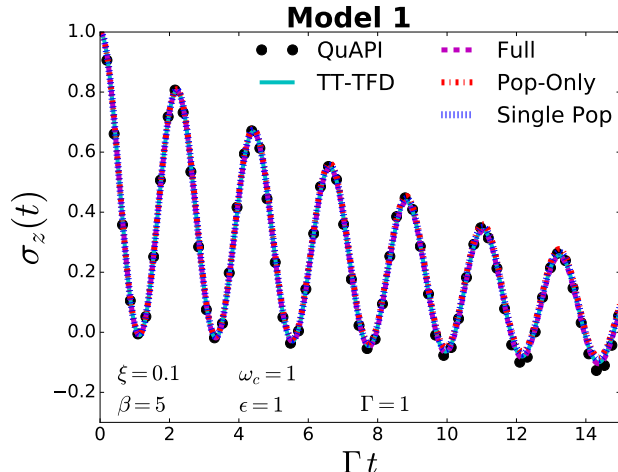


Figure 1: Electronic population difference $\sigma_z(t) = \sigma_{DD}(t) - \sigma_{AA}(t)$ as a function of time for model 1 in Table 1. Shown are exact QuAPI results (black circles) and results obtained based on: direct application of TT-TFD (solid cyan line); a combination of the two single-population scalar GQMEs of the form of Eqs. (47) and (48) for $\sigma_{DD}(t)$ and $\sigma_{AA}(t)$, respectively, with TT-TFD-based PFIs (dotted blue line); a populations-only GQME of the form of Eq. (45) with TT-TFD-based PFIs (dashed-dotted red line); and the full density matrix GQME of the form of Eq. (43) with TT-TFD-based PFIs (dashed magenta line).

Next, we focus on model 4 for a more detailed analysis, with the analogous analysis for the other models provided in the SI. Fig. 6 compares the population relaxation dynamics for model 4 (see Table 1), obtained with different types of GQMEs and memory kernels calculated by TT-TFD and LSCII input methods. The population relaxation dynamics generated via the LSCII-based populations-only GQME is in excellent agreement with the exact results. At the same time, the population relaxation dynamics generated via the LSCII-based single-population GQMEs is inaccurate. The origin of this discrepancy can be traced back to the fact that the LSCII-based single-population GQMEs do not conserve population (i.e., $\sigma_{DD}(t) + \sigma_{AA}(t) \neq 1$).

Figs. 7 and 8 show the real and imaginary parts of the TT-TFD memory kernels for model 4, as compared to the real and imaginary parts of the LSCII memory kernels for the same

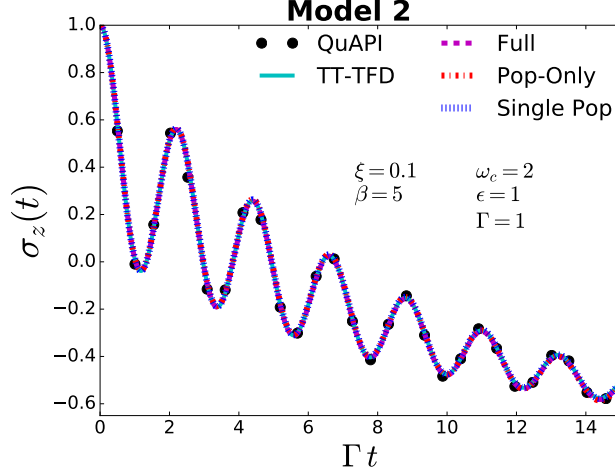


Figure 2: Electronic population difference $\sigma_z(t) = \sigma_{DD}(t) - \sigma_{AA}(t)$ as a function of time for model 2 in Table 1. Shown are exact QuAPI results (black circles) and results obtained based on: direct application of TT-TFD (solid cyan line); a combination of the two single-population scalar GQMEs of the form of Eqs. (47) and (48) for $\sigma_{DD}(t)$ and $\sigma_{AA}(t)$, respectively, with TT-TFD-based PFIs (dotted blue line); a populations-only GQME of the form of Eq. (45) with TT-TFD-based PFIs (dashed-dotted red line); and the full density matrix GQME of the form of Eq. (43) with TT-TFD-based PFIs (dashed magenta line).

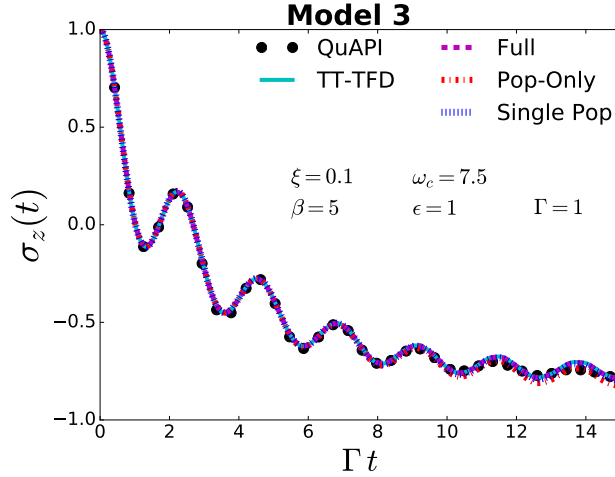


Figure 3: Electronic population difference $\sigma_z(t) = \sigma_{DD}(t) - \sigma_{AA}(t)$ as a function of time for model 3 in Table 1. Shown are exact QuAPI results (black circles) and results obtained based on: direct application of TT-TFD (solid cyan line); a combination of the two single-population scalar GQMEs of the form of Eqs. (47) and (48) for $\sigma_{DD}(t)$ and $\sigma_{AA}(t)$, respectively, with TT-TFD-based PFIs (dotted blue line); a populations-only GQME of the form of Eq. (45) with TT-TFD-based PFIs (dashed-dotted red line); and the full density matrix GQME of the form of Eq. (43) with TT-TFD-based PFIs (dashed magenta line).

model.¹⁹ Each figure includes 16 graphs, corresponding to the elements of the 4×4 memory kernel matrix. Since the memory kernel for the full electronic density matrix GQME is

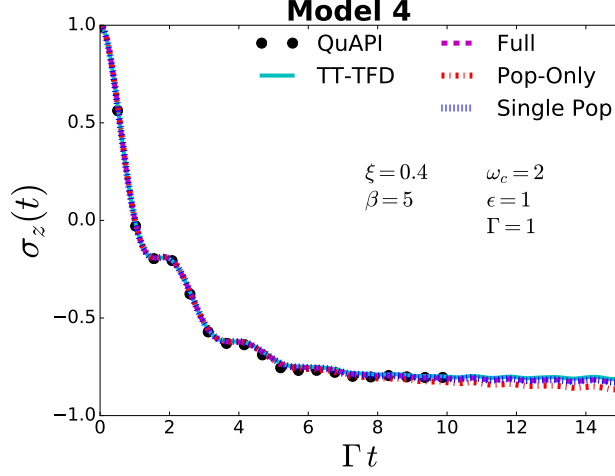


Figure 4: Electronic population difference $\sigma_z(t) = \sigma_{DD}(t) - \sigma_{AA}(t)$ as a function of time for model 4 in Table 1. Shown are exact QuAPI results (black circles) and results obtained based on: direct application of TT-TFD (solid cyan line); a combination of the two single-population scalar GQMEs of the form of Eqs. (47) and (48) for $\sigma_{DD}(t)$ and $\sigma_{AA}(t)$, respectively, with TT-TFD-based PFIs (dotted blue line); a populations-only GQME of the form of Eq. (45) with TT-TFD-based PFIs (dashed-dotted red line); and the full density matrix GQME of the form of Eq. (43) with TT-TFD-based PFIs (dashed magenta line).

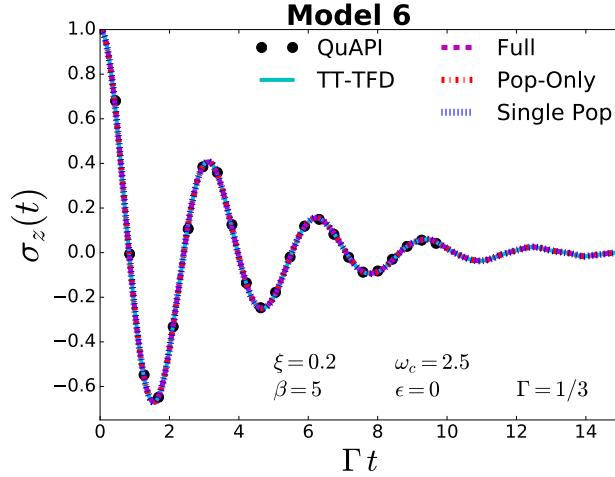


Figure 5: Electronic population difference $\sigma_z(t) = \sigma_{DD}(t) - \sigma_{AA}(t)$ as a function of time for model 6 in Table 1. Shown are exact QuAPI results (black circles) and results obtained based on: direct application of TT-TFD (solid cyan line); a combination of the two single-population scalar GQMEs of the form of Eqs. (47) and (48) for $\sigma_{DD}(t)$ and $\sigma_{AA}(t)$, respectively, with TT-TFD-based PFIs (dotted blue line); a populations-only GQME of the form of Eq. (45) with TT-TFD-based PFIs (dashed-dotted red line); and the full density matrix GQME of the form of Eq. (43) with TT-TFD-based PFIs (dashed magenta line).

represented by a 4×4 matrix, it has elements in all 16 graphs in Figs. 7 and 8. In contrast, the memory kernel of the populations-only GQME is represented by a 2×2 matrix [see

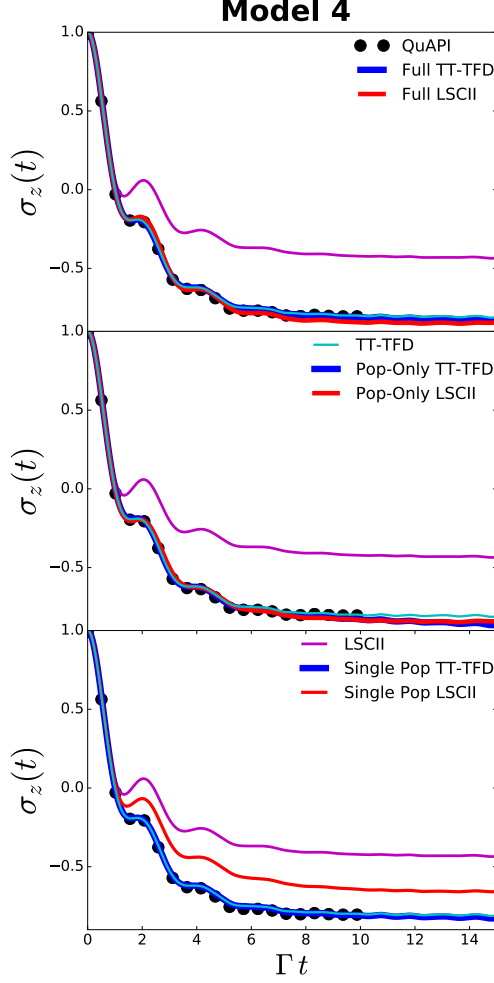


Figure 6: Electronic population difference $\sigma_z(t) = \sigma_{DD}(t) - \sigma_{AA}(t)$ as a function of time for model 4 in Table 1. Shown are exact QuAPI (black circles) and TT-TFD (green lines) results; LSCII result (purple lines); and full GQME (upper plot), populations-only GQME (middle plot) and combination of two single-population scalar GQMEs (lower plot) results obtained with TT-TFD-based PFIs (blue line) and LSCII based PFIs (red line).

Eqs. (45) and (46)]. The real and imaginary parts of the four elements of the populations-only memory kernel are shown in Figs. 9 and 10. The memory kernels of the two single population scalar GQMEs are scalar [see Eqs. (47)-(50)] and their real and imaginary parts are each therefore shown in one graph (the top left corner for the donor single-population GQME and the bottom right corner for the acceptor single-population GQME in Figs. 9 and 10, respectively).

We start the analysis with the memory kernel in the case of the GQME for the full electronic density matrix, $\mathcal{K}^{\text{full}}(\tau)$. In this case, all the corner memory kernel elements ($\mathcal{K}_{DDDD}^{\text{full}}$,

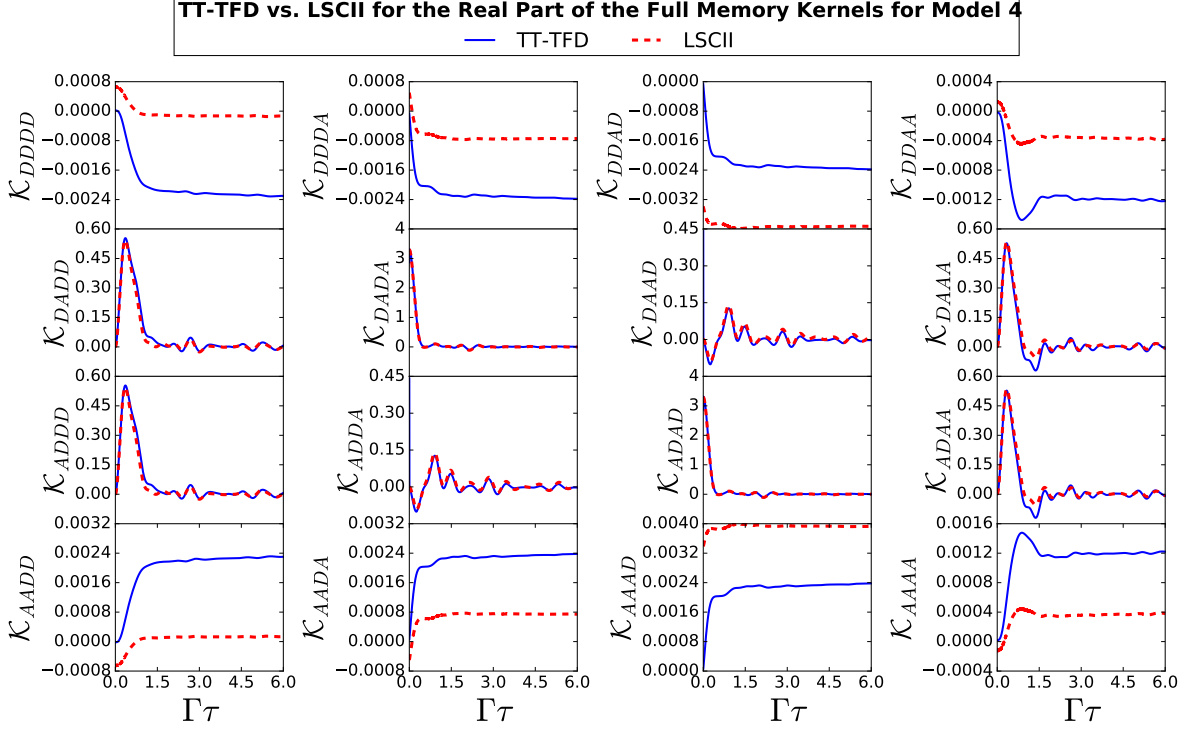


Figure 7: Real parts of the matrix elements of the memory kernel of the GQME for the full electronic density matrix [$\mathcal{K}^{\text{full}}(\tau)$ in Eq. (44)] for model 4 as obtained from TT-TFD-based PFIs (solid blue lines) and LSCII-based PFIs (dashed red lines). Similar graphs for the other four models are provided in the SI.

$\mathcal{K}_{DDAA}^{\text{full}}$, $\mathcal{K}_{AADD}^{\text{full}}$ and $\mathcal{K}_{AAAA}^{\text{full}}$) can be shown to vanish for the TT-TFD-based memory kernels. This implies that, in this case, the memory kernel does not give rise to direct coupling terms between populations but population transfer is mediated by coherences. More specifically, within this GQME type, population transfer from the donor (σ_{DD}) to the acceptor (σ_{AA}) corresponds to a two-step process. It starts with population-to-coherence transfer induced by coupling between σ_{DD} and σ_{DA} or σ_{AD} and then proceeds to coherence-to-population transfer induced by coupling between σ_{DA} or σ_{AD} and σ_{AA} .

Comparison of the eight matrix elements of the memory kernel that couple populations and coherences, namely $\{\mathcal{K}_{DADD}^{\text{full}}, \mathcal{K}_{DDDA}^{\text{full}}, \mathcal{K}_{ADDD}^{\text{full}}, \mathcal{K}_{DDAD}^{\text{full}}, \mathcal{K}_{DAAA}^{\text{full}}, \mathcal{K}_{AADA}^{\text{full}}, \mathcal{K}_{ADAA}^{\text{full}}, \mathcal{K}_{AAAD}^{\text{full}}\}$, reveals several trends:

- The agreement between TT-TFD and LSCII is significantly better for the matrix elements $\{\mathcal{K}_{DADD}^{\text{full}}, \mathcal{K}_{ADDD}^{\text{full}}, \mathcal{K}_{DAAA}^{\text{full}}, \mathcal{K}_{ADAA}^{\text{full}}\}$ than for the matrix elements

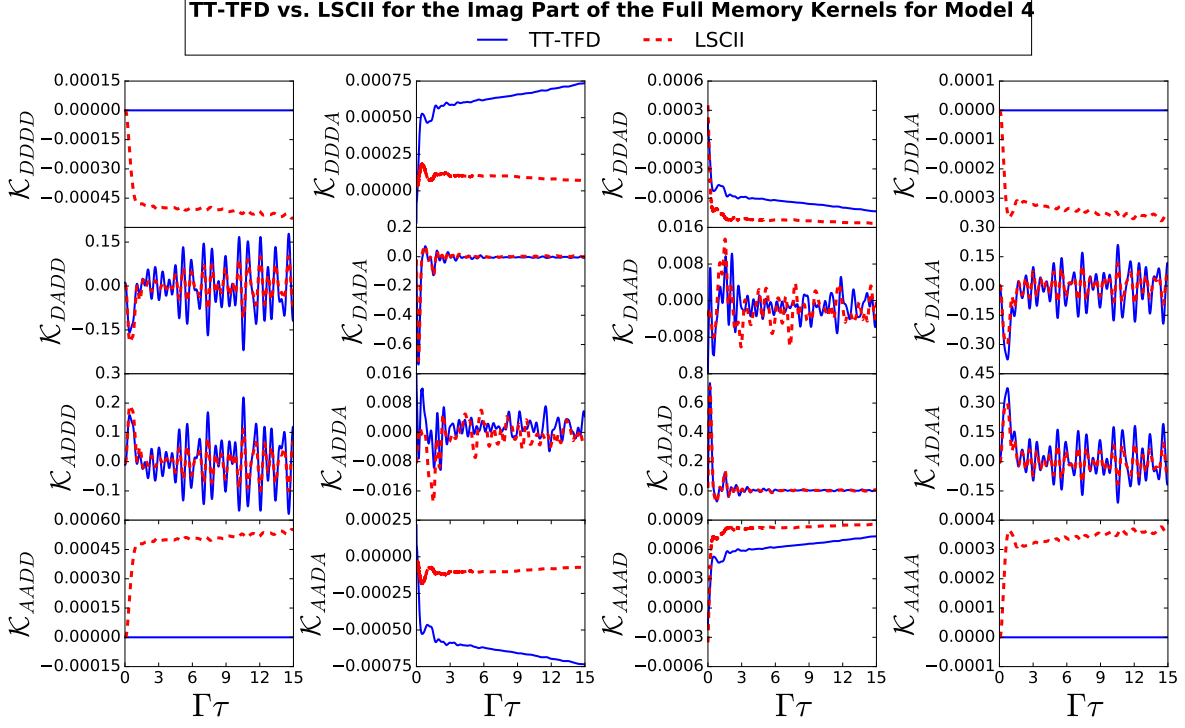


Figure 8: Imaginary parts of the matrix elements of the memory kernel of the GQME for the full electronic density matrix [$\mathcal{K}^{\text{full}}(\tau)$ in Eq. (44)] for model 4 as obtained from TT-TFD-based PFIs (solid blue lines) and LSCII-based PFIs (dashed red lines). Similar graphs for the other four models are provided in the SI.

$\{\mathcal{K}_{DDDA}^{\text{full}}, \mathcal{K}_{DDAD}^{\text{full}}, \mathcal{K}_{AADA}^{\text{full}}, \mathcal{K}_{AAAD}^{\text{full}}\}$. At the same time, the four matrix elements $\{\mathcal{K}_{DDDA}^{\text{full}}, \mathcal{K}_{DDAD}^{\text{full}}, \mathcal{K}_{AADA}^{\text{full}}, \mathcal{K}_{AAAD}^{\text{full}}\}$ are significantly smaller than the remaining four matrix elements $\{\mathcal{K}_{DADD}^{\text{full}}, \mathcal{K}_{ADDD}^{\text{full}}, \mathcal{K}_{DAAA}^{\text{full}}, \mathcal{K}_{ADAA}^{\text{full}}\}$. Thus, LSCII appears to capture the larger-amplitude matrix elements better than the smaller ones. Given the expectation that the larger-amplitude matrix elements would play a more significant role in the dynamics, this observation is consistent with the relative accuracy of the LSCII-based GQME.

- Whereas the real parts of the larger matrix elements $\{\mathcal{K}_{DADD}^{\text{full}}, \mathcal{K}_{ADDD}^{\text{full}}, \mathcal{K}_{DAAA}^{\text{full}}, \mathcal{K}_{ADAA}^{\text{full}}\}$ are seen to be relatively short-lived (compared to the population relaxation time scale, see Figs. 1-5) and exhibit a monotonic decay, the imaginary parts are seen to be oscillatory and do not appear to decay. It should be noted that the oscillatory behavior of the imaginary parts obtained via LSCII is damped compared to exact results obtained via

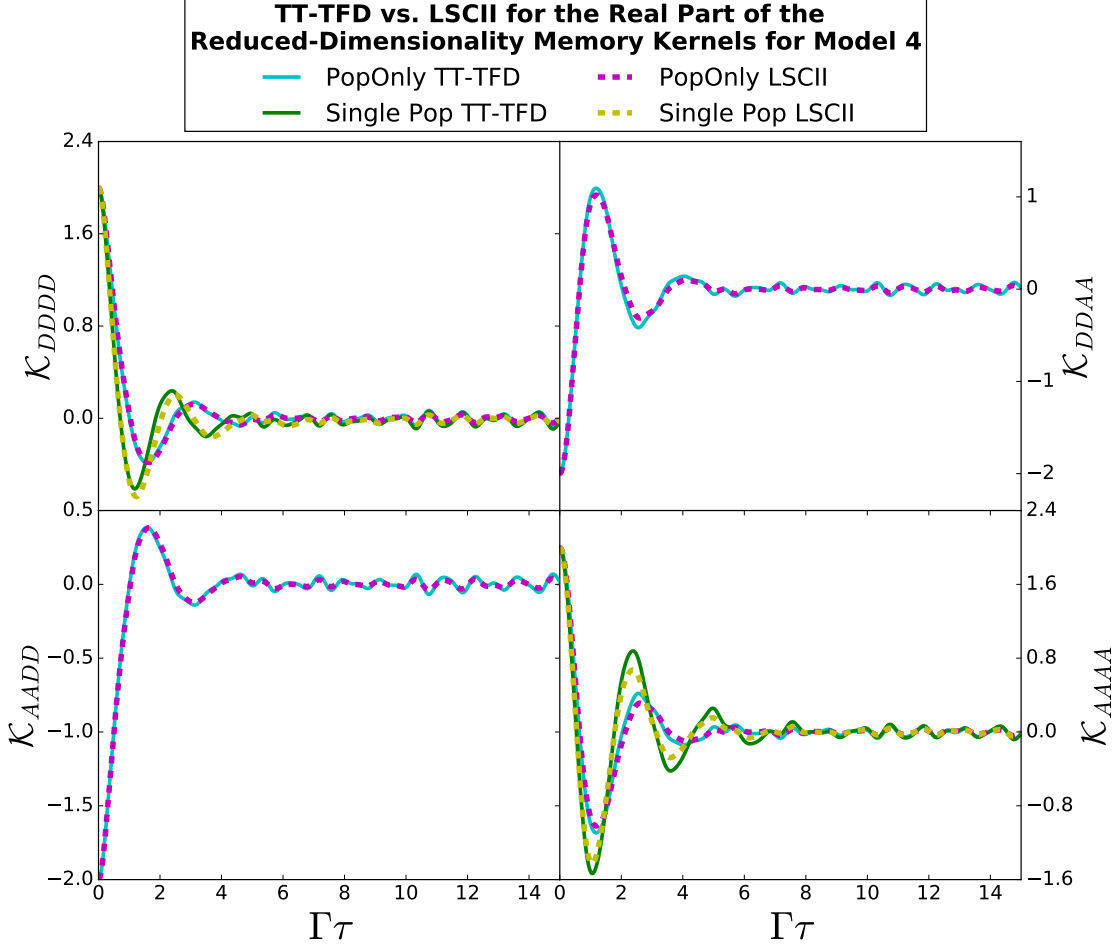


Figure 9: The real parts of the matrix elements of the memory kernels for the populations-only and single-population GQMEs for model 4 as obtained from TT-TFD-based PFIs and LSCII-based PFIs. Shown are the matrix elements of three different memory kernels: (1) The memory kernel of the populations-only GQME [$\mathcal{K}^{\text{Pop}}(\tau)$ in Eq. (46)], which has four elements ($DDDD, DDAA, AADD, AAAA$) and is depicted with solid cyan lines for the results from TT-TFD-based PFIs and dashed magenta lines for the results from LSCII-based PFIs; (2) and (3) The single-element memory kernels of the scalar single-population GQMEs [$\mathcal{K}_{DD,DD}^{\text{donor}}(\tau)$ and $\mathcal{K}_{AA,AA}^{\text{acceptor}}(\tau)$, in Eqs. (49) and (50), respectively], which are depicted in the $DDDD$ and $AAAA$ panels, respectively, with solid green lines for the results from TT-TFD-based PFIs and dashed yellow lines for the results from LSCII-based PFIs. Graphs with the results for the other four models are provided in the SI.

TT-TFD. The observed damping is likely a manifestation of the quasiclassical nature of LSCII, which limits its ability to accurately capture coherent quantum dynamics. Since one expects the real parts to dominate population relaxation rates, the relative accuracy of the LSCII-based GQME can be attributed to the ability of LSCII to

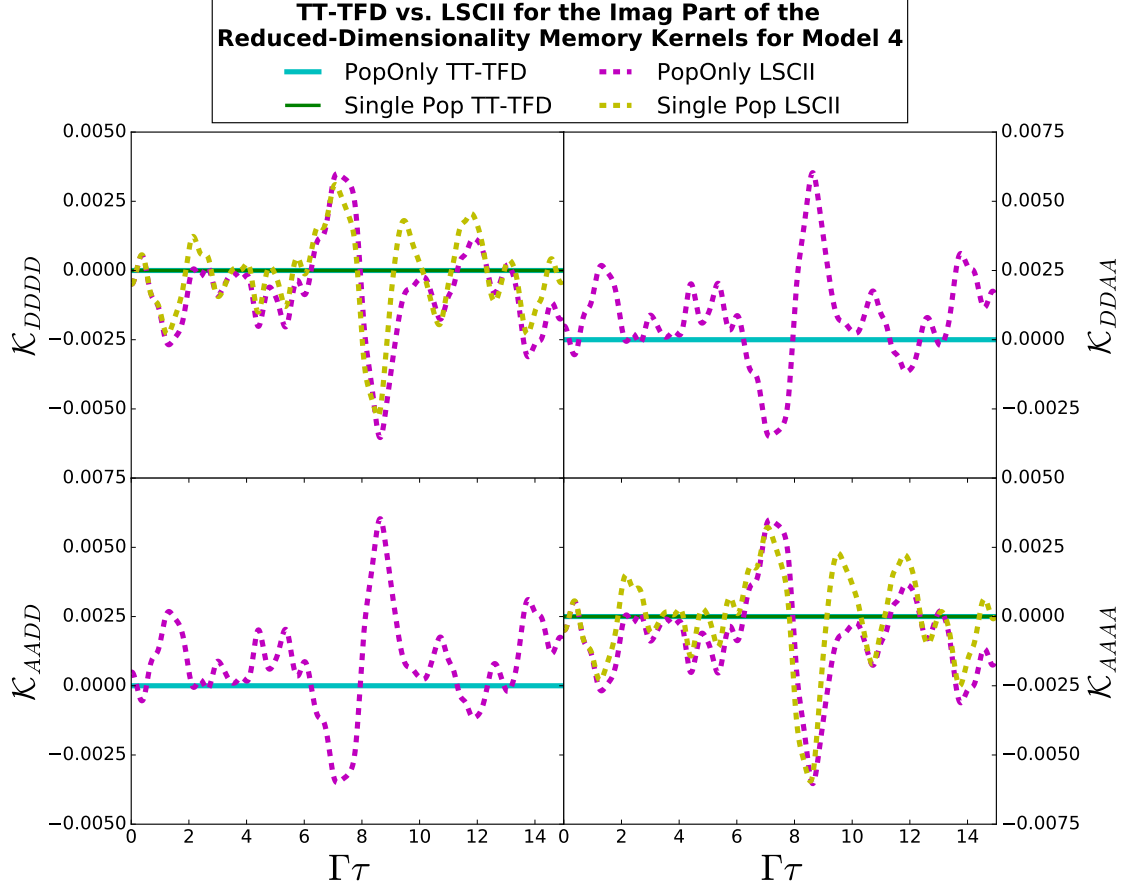


Figure 10: The imaginary parts of the matrix elements of the memory kernels for the populations-only and single-population GQMEs for model 4 as obtained from TT-TFD-based PFIs and LSCII-based PFIs. Shown are the matrix elements of three different memory kernels: (1) The memory kernel of the populations-only GQME [$\mathcal{K}^{\text{pop}}(\tau)$ in Eq. (46)], which has four elements ($DDDD$, $DDAA$, $AADD$, $AAAA$) and is depicted with solid cyan lines for the results from TT-TFD-based PFIs and dashed magenta lines for the results from LSCII-based PFIs; (2) and (3) The single-element memory kernels of the scalar single-population GQMEs [$\mathcal{K}_{DD,DD}^{\text{donor}}(\tau)$ and $\mathcal{K}_{AA,AA}^{\text{acceptor}}(\tau)$, in Eqs. (49) and (50), respectively], which are depicted in the $DDDD$ and $AAAA$ panels, respectively, with solid green lines for the results from TT-TFD-based PFIs and dashed yellow lines for the results from LSCII-based PFIs. Graphs with the results for the other four models are provided in the SI.

capture the real parts rather well.

Examination of the remaining nonvanishing matrix elements, $\{\mathcal{K}_{DADA}^{\text{full}}, \mathcal{K}_{DAAD}^{\text{full}}, \mathcal{K}_{ADDA}^{\text{full}}, \mathcal{K}_{ADAD}^{\text{full}}\}$, reveals the following trends:

- The real parts of $\mathcal{K}_{DADA}^{\text{full}}$ and $\mathcal{K}_{ADAD}^{\text{full}}$ are significantly larger and less oscillatory than the real parts of $\mathcal{K}_{DAAD}^{\text{full}}$ and $\mathcal{K}_{ADDA}^{\text{full}}$. This implies that the dynamics of the coherences

σ_{DA} and σ_{AD} is dominated by dephasing (with rates dictated by $\mathcal{K}_{DADA}^{\text{full}}$ and $\mathcal{K}_{ADAD}^{\text{full}}$) and that coherence-to-coherence transfer (with rates dictated by $\mathcal{K}_{DAAD}^{\text{full}}$ and $\mathcal{K}_{ADDA}^{\text{full}}$) is significantly slower than dephasing. This is consistent with the secular approximation (also called rotating wave approximation), which is often invoked to eliminate coherence transfer terms from perturbative quantum master equations.⁷²

- LSCII appears to capture the real parts of $\{\mathcal{K}_{DADA}^{\text{full}}, \mathcal{K}_{ADAD}^{\text{full}}, \mathcal{K}_{DAAD}^{\text{full}}, \mathcal{K}_{ADDA}^{\text{full}}\}$ rather accurately. LSCII also appears to be less accurate when it comes to capturing the corresponding imaginary parts, with the inaccuracy manifested by an over-damping of the oscillatory behavior. This behavior is similar to that noted above regarding other matrix elements and is consistent with the quasiclassical nature of the approximations on which LSCII is based.

Given that population transfer is mediated by the coherences in the case of the full density matrix GQME, the accuracy of the real parts of the LSCII-based $\{\mathcal{K}_{DADA}^{\text{full}}, \mathcal{K}_{DAAD}^{\text{full}}, \mathcal{K}_{ADDA}^{\text{full}}, \mathcal{K}_{ADAD}^{\text{full}}\}$ likely plays an important role in the ability of the LSCII-based GQME to accurately predict the population relaxation dynamics (see Figs. 1 - 5).

We next consider the memory kernel in the case of the GQME for the electronic populations, $\mathcal{K}^{\text{pop}}(\tau)$ [see Eqs. (45) and (46)]. In this case, the memory kernel is given in terms of a 2×2 matrix that consists of only the corner memory kernel elements in Figs. 7 and 8: $\{\mathcal{K}_{DDDD}^{\text{pop}}, \mathcal{K}_{DDAA}^{\text{pop}}, \mathcal{K}_{AADD}^{\text{pop}}, \mathcal{K}_{AAAA}^{\text{pop}}\}$. The dimensionality of $\mathcal{K}^{\text{pop}}(\tau)$ should be contrasted with the $\mathcal{K}^{\text{full}}(\tau)$, for which the same four matrix elements vanish. Since the coherences have been projected out in this case, for this GQME, the memory kernel gives rise to direct coupling between populations, as opposed to population transfer being mediated by the coherences. As a result, donor-to-acceptor population transfer corresponds to a one-step process.

Comparison of the TT-TFD-based and LSCII-based real and imaginary parts of $\{\mathcal{K}_{DDDD}^{\text{pop}}, \mathcal{K}_{DDAA}^{\text{pop}}, \mathcal{K}_{AADD}^{\text{pop}}, \mathcal{K}_{AAAA}^{\text{pop}}\}$ reveals the following notable trends:

- The real parts of those four memory kernel matrix elements are comparable in size

and exhibit a damped oscillatory behavior that is longer-lived than the non-vanishing matrix elements of $\mathcal{K}^{\text{full}}(\tau)$. This behavior is consistent with previous studies^{19,38} and can be traced back to the fact that in this case, the memory kernel also needs to account for the impact of the projected-out electronic coherences on the electronic populations.

- LSCII is highly accurate when it comes to reproducing the real parts of the exact TT-TFD-based $\{\mathcal{K}_{DDDD}^{\text{pop}}, \mathcal{K}_{DDAA}^{\text{pop}}, \mathcal{K}_{AADD}^{\text{pop}}, \mathcal{K}_{AAAA}^{\text{pop}}\}$. Given that the real parts of the $\mathcal{K}^{\text{pop}}(\tau)$ matrix elements dominate the population transfer kinetics, this observation is consistent with the previously made observation that the LSCII-based populations-only GQME can reproduce the population relaxation rather well.¹⁹
- Whereas the imaginary parts of $\{\mathcal{K}_{DDDD}^{\text{pop}}, \mathcal{K}_{DDAA}^{\text{pop}}, \mathcal{K}_{AADD}^{\text{pop}}, \mathcal{K}_{AAAA}^{\text{pop}}\}$ computed with TT-TFD vanish, the corresponding LSCII values do not. The discrepancy is due to errors in the calculation of $\dot{\mathcal{F}}_{jj,mm}(\tau)$ elements with LSCII, which generates a small real part for the $\dot{\mathcal{F}}_{jj,mm}(\tau)$ elements, which should be purely imaginary. However, the failure of LSCII to accurately predict the imaginary parts does not appear to impact the accuracy of the population transfer kinetics since the imaginary parts are two orders of magnitude smaller than the real parts.

Finally, we consider the scalar memory kernels in the donor and acceptor single-population GQMEs, $\mathcal{K}_{DDDD}^{\text{donor}}(\tau)$ and $\mathcal{K}_{AAAA}^{\text{acceptor}}(\tau)$, respectively [see Eqs. (47)-(50)]. In this case, $\mathcal{K}_{DDDD}^{\text{donor}}(\tau)$ is given by the top-left corner element and $\mathcal{K}_{AAAA}^{\text{acceptor}}(\tau)$ is given by the bottom-left corner element in Figs. 9 and 10. Comparison of the real and imaginary parts of $\mathcal{K}_{DDDD}^{\text{donor}}(\tau)$ and $\mathcal{K}_{AAAA}^{\text{acceptor}}(\tau)$ computed with TT-TFD and LSCII reveals the following notable trends:

- The real parts of $\mathcal{K}_{DDDD}^{\text{donor}}(\tau)$ and $\mathcal{K}_{AAAA}^{\text{acceptor}}(\tau)$ are comparable in size and exhibit a damped oscillatory behavior with a lifetime similar to that of the populations-only memory kernel elements.

- LSCII is highly accurate for reproducing the real part of the exact TT-TFD-based $\mathcal{K}_{DDDD}^{\text{donor}}(\tau)$. The accuracy is somewhat lower for reproducing the real part of $\mathcal{K}_{AAAA}^{\text{acceptor}}(\tau)$.
- While the imaginary parts of $\mathcal{K}_{DDDD}^{\text{donor}}(\tau)$ and $\mathcal{K}_{AAAA}^{\text{acceptor}}(\tau)$ computed with TT-TFD vanish, the corresponding LSCII values do not. However, the failure of LSCII to accurately predict the imaginary parts does not appear to impact the accuracy of the population transfer kinetics since the imaginary parts are two orders of magnitude smaller than the real parts.

In Fig. 11, we show the real part of the inhomogeneous term of the acceptor single-population GQME, $\hat{I}_{AA}(t)$, which is the only GQME with an inhomogeneous term considered in this paper. The imaginary component is not shown because it is zero for the results from both TT-TFD- and LSCII-based PFIs. In the figure, we see that the inhomogeneous term from LSCII-based PFIs is slightly overdamped compared to the inhomogeneous term from the TT-TFD-based PFIs.

To understand the origin of the inaccuracies in the LSCII-based single-population GQMEs relative to the populations-only GQME, we note that any such inaccuracies must come from inaccuracies in $\mathcal{F}(\tau)$ and $\dot{\mathcal{F}}(\tau)$, as the subsequent steps of the GQME approach are exact. To this end, we show in Fig. 12 the imaginary components of the matrix elements of $\mathcal{F}(\tau)$ and in Figs. 13 and 14, the real and imaginary components of the matrix elements of $\dot{\mathcal{F}}(\tau)$ that are used as PFIs to obtain the memory kernels for the single-population and populations-only GQMEs. The real parts of $\mathcal{F}(\tau)$ are not shown because they are zero for these elements from both LSCII and TT-TFD. These figures clearly show that, although the LSCII-based $\mathcal{F}(\tau)$ and $\dot{\mathcal{F}}(\tau)$ matrix elements can be rather accurate, there are significant deviations from the exact ones. The deviations are the origin of any inaccuracies in the memory kernels obtained from them.

We now show that, although the errors in $\mathcal{F}(\tau)$ affect the memory kernels of both single-population and populations-only GQMEs, the effect is weaker on the latter due to error

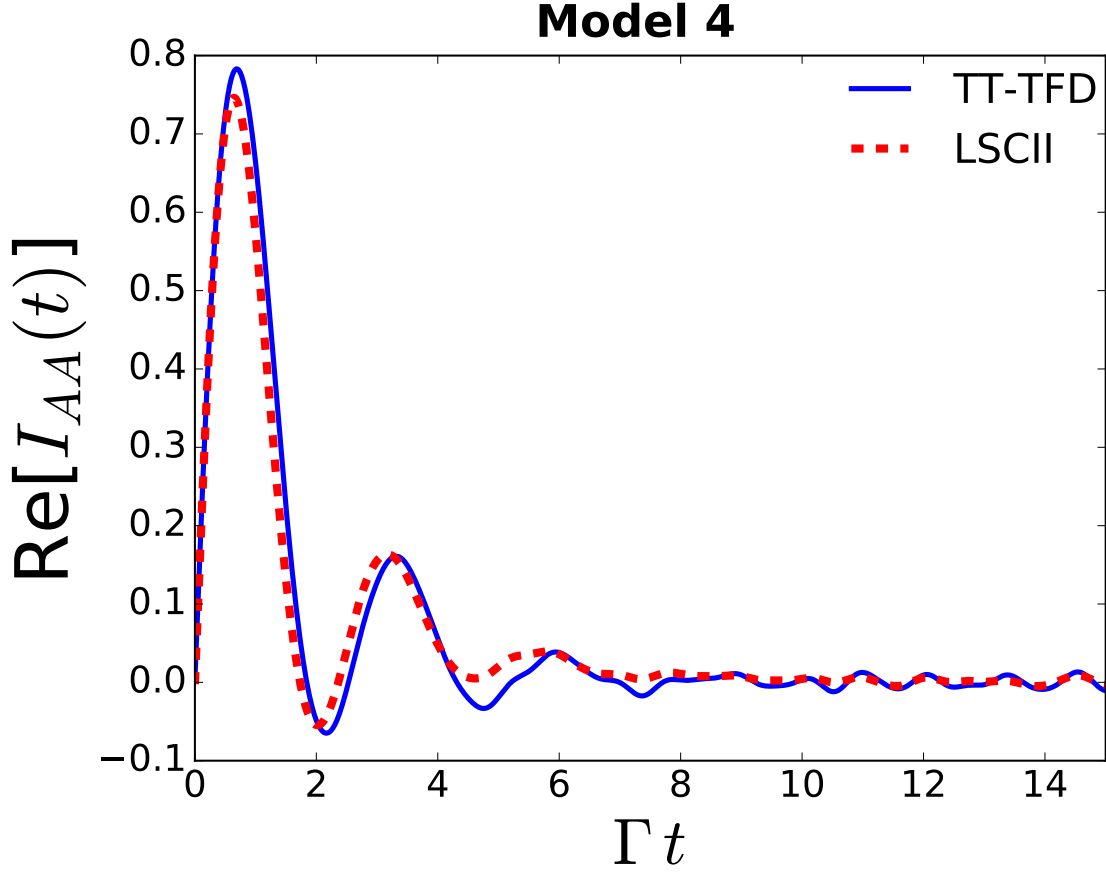


Figure 11: Real part of $\hat{I}_{AA}(\tau)$ [see Eq. (51)] for model 4, as obtained from TT-TFD-based PFIs (solid blue lines) and LSCII-based PFIs (dashed red lines). Similar graphs for the other four models are included in the SI.

cancellation. To see this difference in effect, we note that $K_{DD,DD}^{\text{pop}}(\tau)$ and $K_{DD,DD}^{\text{donor}}(\tau)$ are obtained from the PFIs via Eq. (11):

$$K_{DD,DD}^{\text{pop}}(\tau) = i\dot{\mathcal{F}}_{DD,DD}(\tau) + i \int_0^\tau d\tau' \left[\mathcal{F}_{DD,DD}(\tau - \tau') K_{DD,DD}^{\text{pop}}(\tau') + \mathcal{F}_{DD,AA}(\tau - \tau') K_{AA,DD}^{\text{pop}}(\tau') \right], \quad (52)$$

$$K_{DD,DD}^{\text{donor}}(\tau) = i\dot{\mathcal{F}}_{DD,DD}(\tau) + i \int_0^\tau d\tau' \mathcal{F}_{DD,DD}(\tau - \tau') K_{DD,DD}^{\text{donor}}(\tau'), \quad (53)$$

where the term that involves the reduced system Liouvillian $\langle \mathcal{L} \rangle_n^0$ is dropped because $\langle \mathcal{L}_{jj,kk} \rangle_n^0 = 0$. Importantly, the integrand on the right-hand side of Eq. (52) gives rise to incoherent error cancellation, since $K_{DD,DD}^{\text{pop}}(\tau)$ and $K_{AA,DD}^{\text{pop}}(\tau)$ are of opposite sign, which causes

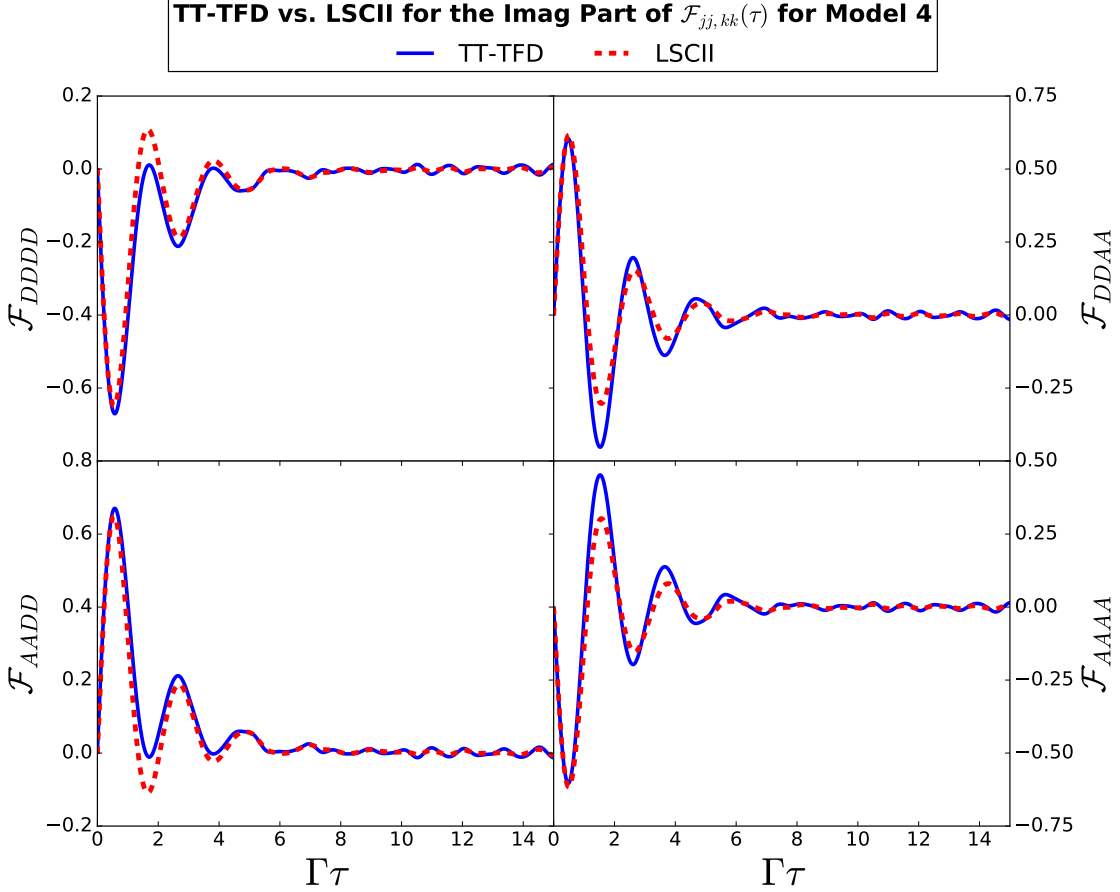


Figure 12: Imaginary parts of the $DDDD$, $DDAA$, $AADD$ and $AAAA$ matrix elements of $\mathcal{F}(\tau)$ [see Eq. (12)] for model 4, as obtained via TT-TFD (solid blue lines) and LSCII (dashed red lines). Similar graphs for the other four models are included in the SI.

errors in $\mathcal{F}(\tau)$ to cancel. On the other hand, Eq. (53) does not allow for such error cancellation, thereby making the single-population GQMEs less accurate than the populations-only GQME.

5.5 Computational Cost

In this section, we examine the scaling of the computational cost of the GQME approach with TT-TFD as the input method with respect to GQME type.

We begin by considering the time step used to calculate the TT-TFD-based PFIs to obtain converged memory kernel and the inhomogeneous term. In contrast to LSCII which required a similar time step for all GQMEs,¹⁹ the time step needed for convergence is found

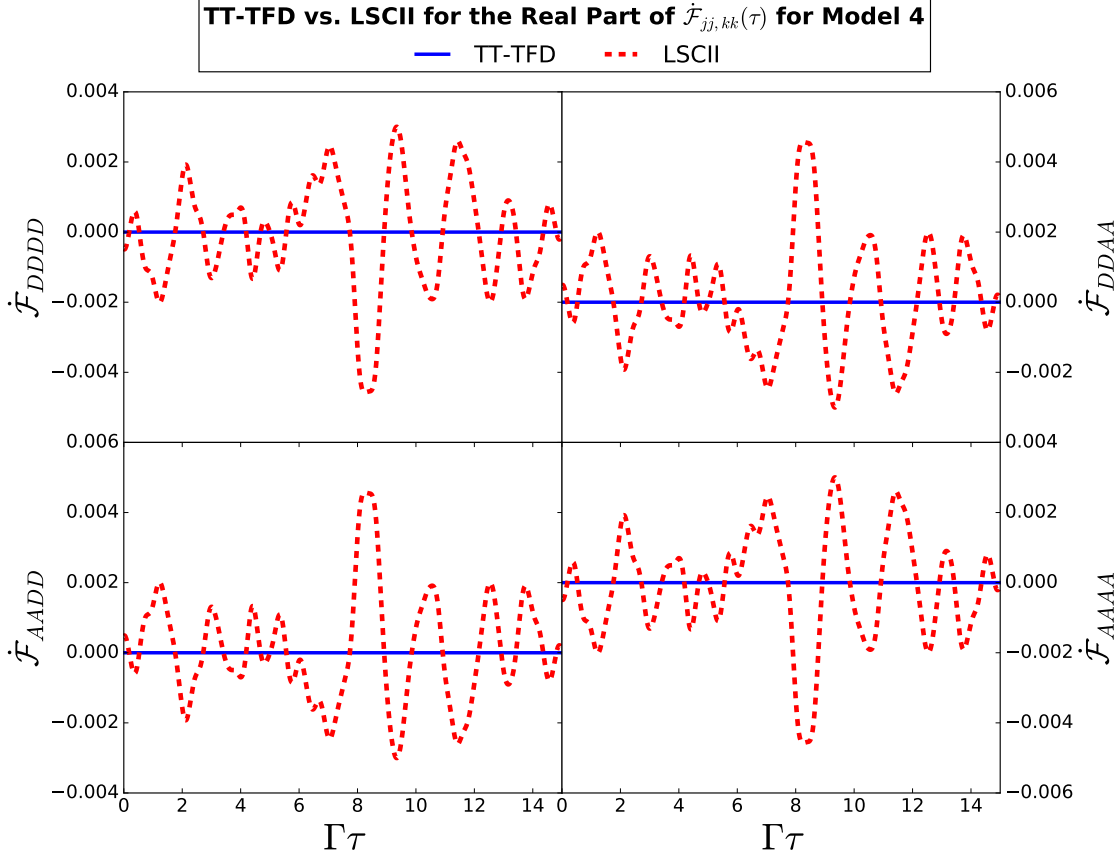


Figure 13: Real parts of the $DDDD$, $DDAA$, $AADD$ and $AAAA$ matrix elements of $\dot{\mathcal{F}}(\tau)$ [see Eq. (12)] for model 4, as obtained via TT-TFD (solid blue lines) and LSCII (dashed red lines). Similar graphs for the other four models are included in the SI.

to decrease with decreasing dimensionality. More specifically, whereas the results shown above are all for a time step of $\Delta t = 0.00150083 \Gamma^{-1}$, the time step needed for convergence for the full density matrix GQME is in the range of $\Delta t = (0.00300166 - 0.00450249) \Gamma^{-1}$ in contrast to the time step of $\Delta t = 0.00150083 \Gamma^{-1}$ required in the case of the populations-only and single-population GQMEs.

In Ref. 19, we noted that the direct calculation of $\dot{\mathcal{F}}_{jk,lm}(\tau)$ given in Eq. (12) requires calculating the dynamics for more electronic initial conditions than only $|j\rangle\langle k|$ due to terms involving off-diagonal components of the Hamiltonian in the initial state. However, although direct calculation of $\dot{\mathcal{F}}_{jk,lm}(\tau)$ is necessary when using approximate input methods; when using exact input methods, we can obtain $\dot{\mathcal{F}}_{jk,lm}(\tau)$ from $\mathcal{U}_{jk,lm}(\tau)$ as described in Eq. (17).

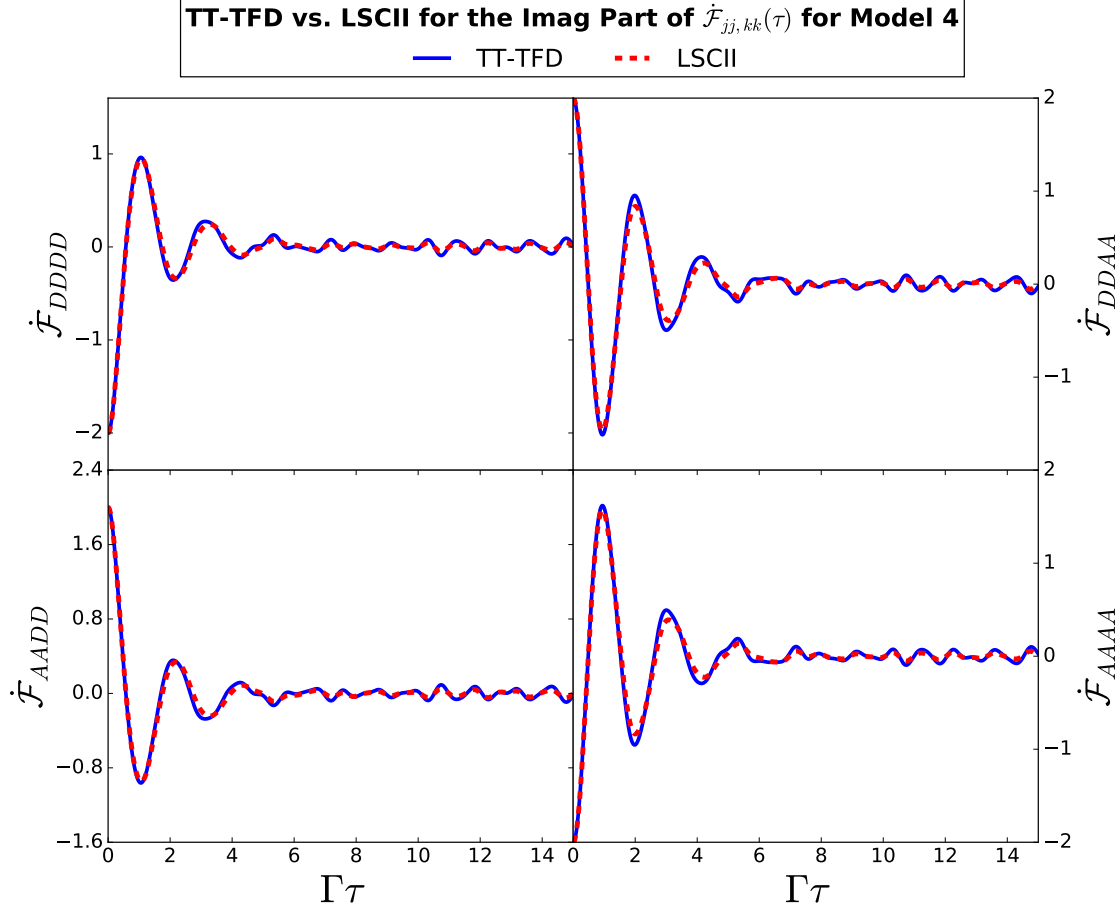


Figure 14: Imaginary parts of the $DDDD$, $DDAA$, $AADD$ and $AAAA$ matrix elements of $\dot{\mathcal{F}}(\tau)$ [see Eq. (12)] for model 4, as obtained via TT-TFD (solid blue lines) and LSCII (dashed red lines). Similar graphs for the other four models are included in the SI.

We therefore only need to calculate the dynamics for the initial electronic state $|j\rangle\langle k|$ to obtain $\mathcal{U}_{jk,lm}(\tau)$ and subsequently $\mathcal{F}_{jk,lm}(\tau)$ and $\dot{\mathcal{F}}_{jk,lm}(\tau)$ through Eq. (17). As a result, there is a significant reduction in the number of initial electronic states necessary for calculating the PFIs needed for the reduced-dimensionality GQMEs compared to the full GQME. More specifically, although the full GQME approach requires simulating the dynamics for 4 initial electronic states in the case of a two-state system, the populations-only GQME requires only 2 initial electronic states, the acceptor single-population GQME approach requires 2 initial electronic states (with one of them due to the inhomogeneous term), and the donor single-population GQME requires only one initial electronic state. Thus, reduced-dimensionality GQMEs significantly enhance computational efficiency with regards to the number of initial

states that need to be simulated when exact input methods like TT-TFD are used.

Next, we consider the cost of obtaining the memory kernels from the PFIs. The computational complexity of each iteration in the Volterra algorithm for the memory kernel is expected to be $O(N_{\text{mat}}^3)$, where N_{mat} is the number of matrix elements in a row of the memory kernel matrix (e.g., $N_{\text{mat}} = N_e^2$ for the full GQME, $N_{\text{mat}} = N_e$ for the populations-only GQME, and $N_{\text{mat}} = 1$ for the single-population GQMEs). This is true regardless of the input method used and therefore the cost of each iteration of the Volterra algorithm increases dramatically with memory kernel size. The computational complexity of each iteration in the Volterra algorithm for the inhomogeneous term scales more favorably at $O(N_{\text{mat}}^2)$ but may still become restrictive with increasing dimensionality. However, it should be noted that the inhomogeneous term often is not needed for the larger-dimensional full and populations-only GQME approaches.

The number of iterations required for the iterative Volterra algorithm for the memory kernel to converge is also rather sensitive to the type of GQME and the dimensionality of the electronic observable of interest. More specifically, whereas 2 iterations are required for calculating the single-population memory kernels and 2-3 iterations are needed in the case of the populations-only memory kernel for all the models, 5-7 iterations are required for the full GQME approach.

An inhomogeneous term is only required for the acceptor single-population GQME approach and would be required for any GQME approach where the set of electronic states that it projects onto does not include the initial electronic state. Because of the scaling of the Volterra algorithm for the inhomogeneous term, it is generally only favorable to use a GQME approach that requires an inhomogeneous term where the dimensionality of the set of electronic states projected onto is small.

The converged memory time for each of the models and GQME types is found using the algorithm outlined in the SI of Ref. 19. The basic premise of the algorithm is to first calculate the dynamics at the highest possible memory time, $t_{\text{mem, max}}$, based on the maximum time

Table 2: **Memory Time of Each GQME Approach for Each Model**

In this table, the colors are provide a visual aid, with red indicating a memory time above $12 \Gamma^{-1}$, yellow indicating a memory time from $9 - 12 \Gamma^{-1}$, and green indicating a memory tie below $9 \Gamma^{-1}$.

Model #	Input Method	Full GQME	Populations-Only GQME	Donor GQME	Acceptor GQME
1	TT-TFD	5.5034	14.7534	14.7534	14.5034
	LSCII	5.25415	14.7541	14.5041	14.5041
2	TT-TFD	1.65348	14.4035	14.9035	14.4035
	LSCII	3.00415	14.2541	14.2541	14.2541
3	TT-TFD	9.5034	13.7534	13.5034	14.0034
	LSCII	7.25415	9.25415	12.0041	11.5041
4	TT-TFD	14.6535	5.65348	14.9035	11.9035
	LSCII	8.50415	6.00415	13.5041	11.7541
6	TT-TFD	9.65348	10.4035	13.9035	13.6535
	LSCII	12.7541	14.7541	14.2541	13.5041

of the PFI dynamics and then proceed backwards in memory time to find the shortest memory time that keeps each element and time step of the electronic density matrix within a convergence parameter when compared to the same element and time step of the dynamics with the highest possible memory time. For the models studied in this paper, the highest possible memory time was $t_{\text{mem}, \text{max}} = 15 \Gamma^{-1}$. The converged memory time for each model and GQME approach is given Table 2. In agreement with the results for LSCII in Ref. 19, the full GQME typically corresponds to the shortest memory time and the reduced-dimensionality GQMEs requires significantly longer memory times, particularly the scalar single-population GQMEs. Whereas the RK4 algorithm is expected to have computational complexity $O(t_{\text{mem}})$, the cost of a single iteration of the Volterra algorithm for the memory kernel has quadratic computational complexity $O(t_{\text{mem}}^2)$. Thus, situations where the reduced dimensionality of the electronic observable of interest leads to longer memory time increases computational cost.

The computational cost of the GQME approaches with respect to dimensionality therefore depends on several factors with different and at times opposing scaling trends. Thus,

the computational cost benefits of reduced-dimensionality GQMEs depends on the balance between these trends and further work is needed to determine whether using a reduced-dimensionality GQME provides a way to significantly reduce computational cost.

6 Concluding Remarks

We have implemented the TT-TFD method to obtain quantum-mechanically exact memory kernels and inhomogeneous terms for different types of GQMEs describing the dynamics of electronic DOF for the spin-boson model. We have analyzed a GQME for the 4-element full electronic reduced density matrix, a populations-only GQME for the two diagonal elements, and single-population scalar GQMEs for single diagonal elements. We have also demonstrated that all four GQMEs are exact equations of motion and thus reproduce the same exact population dynamics when parametrized by a quantum-mechanically exact input method such as TT-TFD, although the four GQMEs are different in form and dimensionality.

Advancing the capability to calculate quantum-mechanically exact memory kernels and inhomogeneous terms for different types of GQMEs is highly desirable for multiple reasons:

- First, it should be noted that the memory kernels and inhomogeneous terms in the case of quantum open systems serve a similar role to that of the Hamiltonian in the case of closed quantum systems. More specifically, similar to how analyzing the properties of the Hamiltonian is often used to shed light on the closed quantum system dynamics it gives rise to, one expects that knowing what the quantum-mechanically exact memory kernel and inhomogeneous term look like and how they depend on various parameters and different choices of projections could shed light on the open quantum system dynamics they give rise to.
- Second, quantum-mechanically exact memory kernels and inhomogeneous terms are particularly valuable to evaluate the capabilities of PFIs obtained with approximate input methods as shown in our comparisons of memory kernels and inhomogeneous

terms obtained with exact TT-TFD and approximate LSCH simulation methods.

- Third, quantum-mechanically exact memory kernels can be used as benchmarks to assess the accuracy of various types of perturbative quantum master equations (QMEs).^{72–83} More specifically, while the GQMEs correspond to the exact equations of motion of the subset of dynamical quantities of interest, the derivation of perturbative QMEs relies on approximate expressions for the memory kernels that are based on treating various terms in the Hamiltonian, such as the system-bath coupling or electronic coupling, as small perturbations. Thus, comparisons of the perturbative memory kernels to the exact kernels can provide a better understanding of the accuracy of perturbative methods and their range of validity.
- Fourth, in certain situations, simulating the quantum dynamics via a GQME may be more cost-effective than the direct use of the numerically-exact quantum dynamics method. More specifically, restricting the use of a quantum-mechanically exact method to calculating the PFIs can provide a more efficient route to obtain the dynamics of the quantity of interest compared to extracting it from the overall system dynamics. The computational cost analysis of the TT-TFD-based GQME approach provided in this paper constitutes the first step towards understanding when and how simulating the quantum dynamics via a GQME approach is advantageous compared to the direct use of the numerically-exact quantum dynamics method.

Various extensions of this study would be highly desirable, including combining the GQME approach with other quantum-mechanically exact and approximate input methods, calculating memory kernels and inhomogeneous terms for other types of dynamical quantities of interest and exploring the capabilities of the GQMEs on other benchmark models. Work on such extensions is currently underway and will be reported in future publications.

Acknowledgments

EG and VSB acknowledge support from the NSF grant 2124511 [CCI Phase I: NSF Center for Quantum Dynamics on Modular Quantum Devices (CQD-MQD)]. MBS acknowledges support from the Yale Quantum Institute Postdoctoral Fellowship. Also acknowledged are computational resources and services provided by the Advanced Research Computing at the University of Michigan, Ann Arbor. We thank Paul Bergold for stimulating discussions.

Data Availability

The code for the TT-TFD + GQME simulation of Model 1 is available at <https://github.com/NingyiLyu/TT-TFD-GQME>. The data that supports the findings of this study are available within the article and SI.

References

- (1) Xu, D.; Schulten, K. Coupling of protein motion to electron transfer in a photosynthetic reaction center: investigating the low temperature behavior in the framework of the spin-boson model. *Chem. Phys.* **1994**, *182*, 91–117.
- (2) Ishizaki, A.; Fleming, G. R. Quantum Coherence in Photosynthetic Light Harvesting. *Annu. Rev. Condens. Matter Phys.* **2012**, *3*, 333–361.
- (3) Liddell, P. A.; Kuciauskas, D.; Sumida, J. P.; Nash, B.; Nguyen, D.; Moore, A. L.; Moore, T. A.; Gust, D. Photoinduced charge separation and charge recombination to a triplet state in a carotene-porphyrin-fullerene triad. *J. Am. Chem. Soc.* **1997**, *119*, 1400–1405.
- (4) Liddell, P. A.; Kodis, G.; Moore, A. L.; Moore, T. A.; Gust, D. Photo switching of

- photoinduced electron transfer in a dithienylethene-porphyrin-fullerene triad molecule. *J. Am. Chem. Soc.* **2002**, *124*, 7668–7669.
- (5) Brédas, J.-L.; Beljonne, D.; Coropceanu, V.; Cornil, J. Charge-Transfer and Energy-Transfer Processes in π -Conjugated Oligomers and Polymers: A Molecular Picture. *Chem. Rev.* **2004**, *104*, 4971–5004.
- (6) Rizzi, A. C.; van Gestel, M.; Liddell, P. A.; Palacios, R. E.; Moore, G. F.; Kodis, G.; Moore, A. L.; Moore, T. A.; Gust, D.; Braslavsky, S. E. Entropic changes control the charge separation process in triads mimicking photosynthetic charge separation. *J. Phys. Chem. A* **2008**, *112*, 4215–4223.
- (7) Tian, H.; Yu, Z.; Hagfeldt, A.; Kloo, L.; Sun, L. Organic Redox Couples and Organic Counter Electrode for Efficient Organic Dye-Sensitized Solar Cells. *J. Am. Chem. Soc.* **2011**, *133*, 9413–9422.
- (8) Mishra, A.; Fischer, M. K. R.; Bäuerle, P. Metal-Free Organic Dyes for Dye-Sensitized Solar Cells: From Structure: Property Relationships to Design Rules. *Angew. Chem. Int. Ed.* **2009**, *48*, 2474–2499.
- (9) Feldt, S. M.; Gibson, E. A.; Gabrielsson, E.; Sun, L.; Boschloo, G.; Hagfeldt, A. Design of Organic Dyes and Cobalt Polypyridine Redox Mediators for High-Efficiency Dye-Sensitized Solar Cells. *J. Am. Chem. Soc.* **2010**, *132*, 16714–16724.
- (10) Zhao, Y.; Liang, W. Charge transfer in organic molecules for solar cells: Theoretical perspective. *Chem. Soc. Rev.* **2012**, *41*, 1075–1087.
- (11) Lee, M. H.; Dunietz, B. D.; Geva, E. Calculation From First Principles of Intramolecular Golden-Rule Rate Constants for Photo-Induced Electron Transfer in Molecular Donor-Acceptor Systems. *J. Phys. Chem. C* **2013**, *117*, 23391–23401.

- (12) Lee, M. H.; Dunietz, B. D.; Geva, E. Donor-to-Donor vs. Donor-to-Acceptor Interfacial Charge Transfer States in the Phthalocyanine-Fullerene Organic Photovoltaic System. *J. Phys. Chem. Lett.* **2014**, *5*, 3810–3816.
- (13) Leggett, A. J.; Chakravarty, S.; Dorsey, A. T.; Fisher, M. P. A.; Garg, A.; Zwerger, W. Dynamics of the dissipative two-state system. *Rev. Mod. Phys.* **1987**, *59*, 1–85.
- (14) Breuer, H.-P.; Petruccione, F. *The Theory of Open Quantum Systems*; Oxford Press: Oxford, 2002.
- (15) Nitzan, A. *Chemical Dynamics in Condensed Phases*; Oxford University Press: New York, 2006.
- (16) Weiss, U. *Quantum Dissipative Systems*, 4th ed.; WORLD SCIENTIFIC, 2012.
- (17) Nakajima, S. On the quantum theory of transport phenomena. *Prog. Theor. Phys.* **1958**, *20*, 948–959.
- (18) Zwanzig, R. Ensemble method in the theory of irreversibility. *J. Chem. Phys.* **1960**, *33*, 1338–1341.
- (19) Mulvihill, E.; Geva, E. Simulating the dynamics of electronic observables via reduced-dimensionality generalized quantum master equations. *J. Chem. Phys.* **2022**, *156*, 044119.
- (20) Meyer, H.-D.; Gatti, F.; Worth, G. A. *Multidimensional Quantum Dynamics*; MCTDH Theory and Applications; John Wiley & Sons, 2009.
- (21) Makri, N. Time-dependent quantum methods for large systems. *Annu. Rev. Phys. Chem.* **1999**, *50*, 167.
- (22) Jin, J.; Zheng, X.; Yan, Y. Exact dynamics of dissipative electronic systems and quantum transport: Hierarchical equations of motion approach. *J. Chem. Phys.* **2008**, *128*, 234703–16.

- (23) Tanimura, Y.; Kubo, R. Time evolution of a quantum system in contact with a nearly Gaussian-Markoffian noise bath. *J. Phys. Soc. Jpn.* **1989**, *58*, 101.
- (24) Tanimura, Y. Nonperturbative expansion method for a quantum system coupled to a harmonic-oscillator bath. *Phys. Rev. A* **1990**, *41*, 6676–6687.
- (25) Tanimura, Y. Stochastic Liouville, Langevin, Fokker–Planck, and Master Equation Approaches to Quantum Dissipative Systems. *J. Phys. Soc. Jpn.* **2006**, *75*, 082001–39.
- (26) Greene, S. M.; Batista, V. S. Tensor-Train Split-Operator Fourier Transform (TT-SOFT) Method: Multidimensional Nonadiabatic Quantum Dynamics. *J. Chem. Theory Comput.* **2017**, *13*, 4034–4042.
- (27) Shi, Q.; Geva, E. A new approach to calculating the memory kernel of the generalized quantum master equation for an arbitrary system-bath coupling. *J. Chem. Phys.* **2003**, *119*, 12063–12076.
- (28) Shi, Q.; Geva, E. A semiclassical generalized quantum master equation for an arbitrary system-bath coupling. *J. Chem. Phys.* **2004**, *120*, 10647–10658.
- (29) Zhang, M.-L.; Ka, B. J.; Geva, E. Nonequilibrium quantum dynamics in the condensed phase via the generalized quantum master equation. *J. Chem. Phys.* **2006**, *125*, 044106–12.
- (30) Ka, B. J.; Zhang, M.-L.; Geva, E. Homogeneity and Markovity of electronic dephasing in liquid solutions. *J. Chem. Phys.* **2006**, *125*, 124509.
- (31) Cohen, G.; Rabani, E. Memory effects in nonequilibrium quantum impurity models. *Phys. Rev. B* **2011**, *84*, 075150.
- (32) Wilner, E. Y.; Wang, H.; Cohen, G.; Thoss, M.; Rabani, E. Bistability in a nonequilibrium quantum system with electron-phonon interactions. *Phys. Rev. B* **2013**, *88*, 045137.

- (33) Cohen, G.; Wilner, E. Y.; Rabani, E. Generalized projected dynamics for non-system observables of non-equilibrium quantum impurity models. *New Journal of Physics* **2013**, *15*, 073018.
- (34) Cohen, G.; Gull, E.; Reichman, D. R.; Millis, A. J.; Rabani, E. Numerically exact long-time magnetization dynamics at the nonequilibrium Kondo crossover of the Anderson impurity model. *Phys. Rev. B* **2013**, *87*, 195108.
- (35) Kelly, A.; Markland, T. E. Efficient and accurate surface hopping for long time nonadiabatic quantum dynamics. *J. Chem. Phys.* **2013**, *139*, 014104–10.
- (36) Kidon, L.; Wilner, E. Y.; Rabani, E. Exact calculation of the time convolutionless master equation generator: Application to the nonequilibrium resonant level model. *J. Chem. Phys.* **2015**, *143*, 234110–9.
- (37) Pfalzgraff, W. C.; Kelly, A.; Markland, T. E. Nonadiabatic Dynamics in Atomistic Environments: Harnessing Quantum-Classical Theory with Generalized Quantum Master Equations. *J. Phys. Chem. Lett.* **2015**, 4743–4748.
- (38) Montoya-Castillo, A.; Reichman, D. R. Approximate but accurate quantum dynamics from the Mori formalism: I. Nonequilibrium dynamics. *J. Chem. Phys.* **2016**, *144*, 184104–16.
- (39) Kelly, A.; Brackbill, N.; Markland, T. E. Accurate nonadiabatic quantum dynamics on the cheap: Making the most of mean field theory with master equations. *J. Chem. Phys.* **2015**, *142*, 094110–9.
- (40) Kelly, A.; Montoya-Castillo, A.; Wang, L.; Markland, T. E. Generalized quantum master equations in and out of equilibrium: When can one win? *J. Chem. Phys.* **2016**, *144*, 184105.

- (41) Kidon, L.; Wang, H.; Thoss, M.; Rabani, E. On the memory kernel and the reduced system propagator. *J. Chem. Phys.* **2018**, *149*, 104105–4.
- (42) Pfalzgraff, W.; Montoya-Castillo, A.; Kelly, A.; Markland, T. Efficient construction of generalized master equation memory kernels for multi-state systems from nonadiabatic quantum-classical dynamics. *J. Chem. Phys.* **2019**, *150*, 244109–16.
- (43) Mulvihill, E.; Schubert, A.; Sun, X.; Dunietz, B. D.; Geva, E. A modified approach for simulating electronically nonadiabatic dynamics via the generalized quantum master equation. *J. Chem. Phys.* **2019**, *150*, 034101.
- (44) Mulvihill, E.; Gao, X.; Liu, Y.; Schubert, A.; Dunietz, B. D.; Geva, E. Combining the mapping Hamiltonian linearized semiclassical approach with the generalized quantum master equation to simulate electronically nonadiabatic molecular dynamics. *J. Chem. Phys.* **2019**, *151*, 074103.
- (45) Mulvihill, E.; Lenn, K. M.; Gao, X.; Schubert, A.; Dunietz, B. D.; Geva, E. Simulating energy transfer dynamics in the Fenna-Matthews-Olson complex via the modified generalized quantum master equation. *J. Chem. Phys.* **2021**, *154*, 204109.
- (46) Mulvihill, E.; Geva, E. A Road Map to Various Pathways for Calculating the Memory Kernel of the Generalized Quantum Master Equation. *J. Phys. Chem. B* **2021**, *125*, 9834–9852.
- (47) Xu, M.; Yan, Y.; Liu, Y.; Shi, Q. Convergence of high order memory kernels in the Nakajima-Zwanzig generalized master equation and rate constants: Case study of the spin-boson model. *J. Chem. Phys.* **2018**, *148*, 164101.
- (48) Liu, Y.-y.; Yan, Y.-m.; Xu, M.; Song, K.; Shi, Q. Exact generator and its high order expansions in time-convolutionless generalized master equation: Applications to spin-boson model and excitation energy transfer. *Chin. J. Chem. Phys.* **2018**, *31*, 575–583.

- (49) Yan, Y.; Xu, M.; Liu, Y.; Shi, Q. Theoretical study of charge carrier transport in organic molecular crystals using the Nakajima-Zwanzig-Mori generalized master equation. *J. Chem. Phys.* **2019**, *150*, 234101.
- (50) Dan, X.; Xu, M.; Yan, Y.; Shi, Q. Generalized master equation for charge transport in a molecular junction: Exact memory kernels and their high order expansion. *J. Chem. Phys.* **2022**, *156*, 134114.
- (51) Chatterjee, S.; Makri, N. Real-Time Path Integral Methods, Quantum Master Equations, and Classical vs Quantum Memory. *J. Phys. Chem. B* **2019**, *123*, 10470–10482.
- (52) Brian, D.; Sun, X. Generalized quantum master equation: A tutorial review and recent advances. *Chin. J. Chem. Phys.* **2021**, *34*, 497–524.
- (53) Gelin, M. F.; Borrelli, R. Thermal Schrödinger Equation: Efficient Tool for Simulation of Many-Body Quantum Dynamics at Finite Temperature. *Annalen der Physik* **2017**, *529*, 1700200.
- (54) Borrelli, R.; Gelin, M. F. Finite temperature quantum dynamics of complex systems: Integrating thermo-field theories and tensor-train methods. *WIREs Comput Mol Sci.* **2021**, *11*, e1539.
- (55) Ng, N.; Limmer, D. T.; Rabani, E. Nonuniqueness of generalized quantum master equations for a single observable. *J. Chem. Phys.* **2021**, *155*, 156101.
- (56) Borrelli, R.; Gelin, M. F. Quantum electron-vibrational dynamics at finite temperature: Thermo field dynamics approach. *Journal of Chemical Physics* **2016**, *145*.
- (57) Borrelli, R.; Gelin, M. F. Simulation of Quantum Dynamics of Excitonic Systems at Finite Temperature: An efficient method based on Thermo Field Dynamics. *Scientific Reports* **2017**, *7*.

- (58) Oseledets, I. V. Tensor-train decomposition. *SIAM Journal on Scientific Computing* **2011**, *33*, 2295–2317.
- (59) Oseledets, I.; Tyrtshnikov, E. TT-cross approximation for multidimensional arrays. *Linear Algebra and Its Applications* **2010**, *432*, 70–88.
- (60) Grasedyck, L. Hierarchical singular value decomposition of tensors. *SIAM Journal on Matrix Analysis and Applications* **2009**, *31*, 2029–2054.
- (61) Hackbusch, W.; Kühn, S. A new scheme for the tensor representation. *Journal of Fourier Analysis and Applications* **2009**, *15*, 706–722.
- (62) Lyu, N.; Soley, M. B.; Batista, V. S. Tensor-Train Split-Operator KSL (TT-SOKSL) Method for Quantum Dynamics Simulations. *Journal of Chemical Theory and Computation* **2022**, *18*, 3327–3346.
- (63) Soley, M. B.; Bergold, P.; Gorodetsky, A. A.; Batista, V. S. Functional Tensor-Train Chebyshev Method for Multidimensional Quantum Dynamics Simulations. *Journal of Chemical Theory and Computation* **2021**, *18*, 25–36.
- (64) Soley, M. B.; Bergold, P.; Batista, V. S. Iterative Power Algorithm for Global Optimization with Quantics Tensor Trains. *Journal of Chemical Theory and Computation* **2021**, *17*, 3280–3291.
- (65) Takahashi, Y.; Suzuki, H. Thermo Field Dynamics. *International Journal of Modern Physics B* **1996**, *10*, 1755–1805.
- (66) Lubich, C.; Oseledets, I. V.; Vandereycken, B. Time integration of tensor trains. *SIAM Journal on Numerical Analysis* **2015**, *53*, 917–941.
- (67) Lubich, C.; Oseledets, I. V. A projector-splitting integrator for dynamical low-rank approximation. *BIT Numerical Mathematics* **2014**, *54*, 171–188.

- (68) Li, W.; Ren, J.; Shuai, Z. Numerical assessment for accuracy and GPU acceleration of TD-DMRG time evolution schemes. *J. Chem. Phys.* **2020**, *152*, 024127.
- (69) Sun, X.; Wang, H.; Miller, W. H. On the semiclassical description of quantum coherence in thermal rate constants. *J. Chem. Phys.* **1998**, *109*, 4190–4200.
- (70) Saller, M. A. C.; Lai, Y.; Geva, E. An Accurate Linearized Semiclassical Approach for Calculating Cavity-Modified Charge Transfer Rate Constants. *The Journal of Physical Chemistry Letters* **2022**, *13*, 2330–2337, PMID: 35245071.
- (71) Ren, J.; Li, W.; Jiang, T.; Wang, Y.; Shuai, Z. Time-dependent density matrix renormalization group method for quantum dynamics in complex systems. *Wiley Interdisciplinary Reviews: Computational Molecular Science* **2022**, e1614.
- (72) Baiz, C. R.; Kubarych, K. J.; Geva, E. Molecular theory and simulation of coherence transfer in metal carbonyls and its signature on multidimensional infrared spectra. *J. Phys. Chem. B* **2011**, *115*, 5322–5339.
- (73) Redfield, A. G. On the theory of relaxation processes. *IBM Jr.* **1957**, *1*, 19.
- (74) Pollard, W. T.; Friesner, R. A. Solution of the Redfield equation for the dissipative quantum dynamics of multilevel systems. *J. Chem. Phys.* **1994**, *100*, 5054.
- (75) Pollard, W. T.; Felts, A. K.; Friesner, R. A. The Redfield equation in condensed-phase quantum dynamics. *Adv. Chem. Phys.* **1996**, *XCIII*, 77.
- (76) Meier, C.; Tannor, D. Non-Markovian evolution of the density operator in presence of strong laser fields. *J. Chem. Phys.* **1999**, *111*, 3365.
- (77) Egorova, D.; Kühn, A.; Domcke, W. Modeling of ultrafast electron-transfer dynamics: Multi-level Redfield theory and validity of approximation. *Chem. Phys.* **2001**, *268*, 105.
- (78) Laird, B. B.; Budimir, J.; Skinner, J. L. *J. Chem. Phys.* **1991**, *94*, 4391.

- (79) Zhang, W. M.; Meier, T.; Chernyak, V.; Mukamel, S. Exciton-migration and three-pulse femtosecond optical spectroscopies of photosynthetic antenna complexes. *J. Chem. Phys.* **1998**, *108*, 7763–7774.
- (80) Novoderezhkin, V. I.; Yakovlev, A. G.; van Grondelle, R.; Shuvalov, V. A. Coherent Nuclear and Electronic Dynamics in Primary Charge Separation in Photosynthetic Reaction Centers: A Redfield Theory Approach. *J. Phys. Chem. B* **2004**, *108*, 7445–7457.
- (81) Trushechkin, A. Calculation of coherences in Förster and modified Redfield theories of excitation energy transfer. *J. Chem. Phys.* **2019**, *151*, 074101–19.
- (82) Jang, S. J. *Dynamics of Molecular Excitons*; Elsevier, 2020.
- (83) Lai, Y.; Geva, E. On simulating the dynamics of electronic populations and coherences via quantum master equations based on treating off-diagonal electronic coupling terms as a small perturbation. *J. Chem. Phys.* **2021**, *155*, 204101.

Tensor-train thermo-field memory kernels for generalized quantum master equations

Supplementary Material

Ningyi Lyu^{1,§}, Ellen Mulvihill^{1,§}, Micheline Soley^{1,2,3}, Eitan Geva^{4,*}, and Victor Batista^{1,2,*}

¹*Department of Chemistry, Yale University, New Haven, Connecticut 06520, United States*

²*Yale Quantum Institute, Yale University, New Haven, Connecticut 06511, United States*

³*Department of Chemistry, University of Wisconsin-Madison, Madison, Wisconsin 53706, United States*

⁴*Department of Chemistry, University of Michigan, Ann Arbor, Michigan 48109, United States*

[§]*These authors contributed equally.*

***E-mail:** eitan@umich.edu, victor.batista@yale.edu

This supplementary material includes a thorough derivation of the QGME reduced-dimensionality approach and a description of the linear combinations used within the TT-TFD approach to obtain elements of the time evolution operator of the reduced electronic density operator, $\mathcal{U}(t)$, for off-diagonal initial states along with graphs of the PFIs, memory kernels, and inhomogeneous terms that are not included in the main text.

Table of Contents

S.I	QGME Derivation	S1
S.I.1	Modified Approach to the QGME (M-QGME)	S3
S.I.2	Reduced-Dimensionality QGMEs	S6
S.II	Projection-Free Inputs	S11
S.III	Equivalence between the TFD Schrödinger equation and the quantum Liouville equation	S16
S.IV	Linear Combinations for Off-Diagonal Initial States of $\mathcal{U}(t)$	S16
S.V	Graphs of the Projection-Free Inputs	S18
S.VI	Graphs of the Memory Kernels	S30
S.VII	Graphs of the Inhomogeneous Terms of All of the Models	S46
	References	S49

S.I QGME Derivation

The derivation of the QGME starts with the quantum Liouville equation (sometimes also called the von Neumann equation) for the density operator of the overall system $\hat{\rho}(t)$:

$$\frac{d}{dt}\hat{\rho}(t) = -\frac{i}{\hbar}\mathcal{L}\hat{\rho}(t), \quad (\text{S.1})$$

where the $\mathcal{L} = [\hat{H}, \cdot]$ is the Liouvillian superoperator and \hat{H} is the Hamiltonian of the overall system and is assumed to be time-independent for simplicity. Throughout these notes, boldfaced variables, e.g., \mathbf{A} , indicate vector quantities; a hat over a variable, e.g., \hat{B} , indicates an operator quantity; and calligraphic font, e.g., \mathcal{L} , indicates a superoperator.

The derivation of the QME equation uses projection operator techniques. A projection operator is an operator that satisfies idempotence, i.e., additional applications of the operator do not change the result beyond the initial application of operator (e.g., $\hat{A}^2 = \hat{A}$), and is used to project on to a certain subspace of the system.

We use any projection superoperator \mathcal{P} , apply it to both sides of Eq. (S.1), and use its complimentary projection superoperator $\mathcal{Q} = 1 - \mathcal{P}$ (i.e., \mathcal{Q} projects onto what \mathcal{P} projects out) to reach:

$$\begin{aligned} \frac{d}{dt} \mathcal{P} \hat{\rho}(t) &= -\frac{i}{\hbar} \mathcal{P} \mathcal{L} \hat{\rho}(t) \\ &= -\frac{i}{\hbar} \mathcal{P} \mathcal{L} (\mathcal{P} + \mathcal{Q}) \hat{\rho}(t) \\ &= -\frac{i}{\hbar} \mathcal{P} \mathcal{L} \mathcal{P} \hat{\rho}(t) - \frac{i}{\hbar} \mathcal{P} \mathcal{L} \mathcal{Q} \hat{\rho}(t). \end{aligned} \quad (\text{S.2})$$

The same can be done for $\mathcal{Q} \hat{\rho}(t)$:

$$\frac{d}{dt} \mathcal{Q} \hat{\rho}(t) = -\frac{i}{\hbar} \mathcal{Q} \mathcal{L} \mathcal{P} \hat{\rho}(t) - \frac{i}{\hbar} \mathcal{Q} \mathcal{L} \mathcal{Q} \hat{\rho}(t), \quad (\text{S.3})$$

which, when considered as an inhomogeneous first-order differential equation, can be solved explicitly to give

$$\mathcal{Q} \hat{\rho}(t) = e^{-i\mathcal{Q}\mathcal{L}t/\hbar} \mathcal{Q} \hat{\rho}(0) - \frac{i}{\hbar} \int_0^t dt' e^{-i\mathcal{Q}\mathcal{L}(t-t')/\hbar} \mathcal{Q} \mathcal{L} \mathcal{P} \hat{\rho}(t'). \quad (\text{S.4})$$

The proof of Eq. (S.4) is done by first plugging the RHS of Eq. (S.4) into the LHS of Eq. (S.3) and evaluating the derivative, using the identity $\frac{d}{dt} \int_0^t dt' f(t, t') = f(t, t) + \int_0^t dt' \frac{\partial f(t, t')}{\partial t}$:

$$\begin{aligned} &\frac{d}{dt} \left\{ e^{-i\mathcal{Q}\mathcal{L}t/\hbar} \mathcal{Q} \hat{\rho}(0) - \frac{i}{\hbar} \int_0^t dt' e^{-i\mathcal{Q}\mathcal{L}(t-t')/\hbar} \mathcal{Q} \mathcal{L} \mathcal{P} \hat{\rho}(t') \right\} \\ &= -\frac{i}{\hbar} \mathcal{Q} \mathcal{L} e^{-i\mathcal{Q}\mathcal{L}t/\hbar} \mathcal{Q} \hat{\rho}(0) - \frac{i}{\hbar} \mathcal{Q} \mathcal{L} \mathcal{P} \hat{\rho}(t) - \frac{1}{\hbar^2} \int_0^t dt' \mathcal{Q} \mathcal{L} e^{-i\mathcal{Q}\mathcal{L}(t-t')/\hbar} \mathcal{Q} \mathcal{L} \mathcal{P} \hat{\rho}(t'). \end{aligned} \quad (\text{S.5})$$

We then substitute the RHS of Eq. (S.4) into the second term on the RHS of Eq. (S.3):

$$-\frac{i}{\hbar} \mathcal{Q} \mathcal{L} \mathcal{Q} \hat{\rho}(t) = -\frac{i}{\hbar} \mathcal{Q} \mathcal{L} e^{-i\mathcal{Q}\mathcal{L}t/\hbar} \mathcal{Q} \hat{\rho}(0) - \frac{1}{\hbar^2} \int_0^t dt' \mathcal{Q} \mathcal{L} e^{-i\mathcal{Q}\mathcal{L}(t-t')/\hbar} \mathcal{Q} \mathcal{L} \mathcal{P} \hat{\rho}(t'). \quad (\text{S.6})$$

If we combine the RHS of the above equation with the first, and only other, term of the RHS of Eq. (S.3), $-\frac{i}{\hbar}\mathcal{Q}\mathcal{L}\mathcal{P}\hat{\rho}(t)$, we can see that it is equivalent to Eq. (S.5) [which is the evaluation of the LHS of Eq. (S.3)], proving Eq. (S.4).

We then change the integration variable of Eq. (S.4) with $t' = t - \tau$, giving

$$\mathcal{Q}\hat{\rho}(t) = e^{-i\mathcal{Q}\mathcal{L}t/\hbar}\mathcal{Q}\hat{\rho}(0) - \frac{i}{\hbar}\int_0^t d\tau e^{-i\mathcal{Q}\mathcal{L}(\tau)/\hbar}\mathcal{Q}\mathcal{L}\mathcal{P}\hat{\rho}(t - \tau). \quad (\text{S.7})$$

Plugging Eq. (S.7) into Eq. (S.2) leads to the the Nakajima-Zwanzig equation:¹⁻⁴

$$\begin{aligned} \frac{d}{dt}\mathcal{P}\hat{\rho}(t) &= -\frac{i}{\hbar}\mathcal{P}\mathcal{L}\mathcal{P}\hat{\rho}(t) - \frac{i}{\hbar}\mathcal{P}\mathcal{L}\left[e^{-i\mathcal{Q}\mathcal{L}t/\hbar}\mathcal{Q}\hat{\rho}(0) - \frac{i}{\hbar}\int_0^t d\tau e^{-i\mathcal{Q}\mathcal{L}(\tau)/\hbar}\mathcal{Q}\mathcal{L}\mathcal{P}\hat{\rho}(t - \tau)\right] \\ &= -\frac{i}{\hbar}\mathcal{P}\mathcal{L}\mathcal{P}\hat{\rho}(t) - \frac{i}{\hbar}\mathcal{P}\mathcal{L}e^{-i\mathcal{Q}\mathcal{L}t/\hbar}\mathcal{Q}\hat{\rho}(0) - \frac{1}{\hbar^2}\int_0^t d\tau\mathcal{P}\mathcal{L}e^{-i\mathcal{Q}\mathcal{L}\tau/\hbar}\mathcal{Q}\mathcal{L}\mathcal{P}\hat{\rho}(t - \tau). \end{aligned} \quad (\text{S.8})$$

Importantly, there is a lot of flexibility when it comes to the choice of projection superoperator, \mathcal{P} , and thereby observables of interest. Each such choice would in turn give rise to a different equation of motion, or GQME, for the observable quantity of interest, as dictated by the choice of projection superoperator. In Ref. 5, we explored several different projection operators that gave different GQMEs for the reduced electronic density operator and found that the modified approach to the GQME (previously introduced in Ref. 6) was the best choice. In Ref. 7, we outlined different projection operators that resulted in reduced-dimensionality GQMEs for subsets of electronic populations and/or coherences. The next two subsections will outline the modified approach to the GQME (M-GQME) and the general reduced-dimensionality GQME for any subset of the elements of the electronic reduced density matrix.

S.I.1 Modified Approach to the GQME (M-GQME)

The modified approach to the GQME (M-GQME) gives an equation of motion for the full electronic reduced density matrix. We will assume the initial state of the overall system has the commonly-encountered factorized form

$$\hat{\rho}(0) = \hat{\rho}_n(0) \otimes \hat{\sigma}(0), \quad (\text{S.9})$$

where $\hat{\rho}_n(0) = \text{Tr}_e\{\hat{\rho}(0)\}$ and $\hat{\sigma}(0) = \text{Tr}_n\{\hat{\rho}(0)\}$ are the reduced density operators that describe the initial states of the nuclear DOF and electronic DOF, respectively, and $\text{Tr}_e\{\cdot\}$ and $\text{Tr}_n\{\cdot\}$ stand for partially tracing over the electronic Hilbert space and the nuclear Hilbert space, respectively. It should be noted that this initial state is not required for the GQME and Ref. 6 outlines a method of using the GQME approach for an entangled initial state. The M-GQME is based on the following

choice of projection superoperator:

$$\mathcal{P}^{\text{full}}(\hat{A}) = \hat{\rho}_n(0) \otimes \text{Tr}_n\{\hat{A}\} . \quad (\text{S.10})$$

Here, \hat{A} is an arbitrary overall system operator that the projection superoperator \mathcal{P} operates on and $\hat{\rho}_n(0)$ must satisfy the condition $\text{Tr}_n\{\hat{\rho}_n(0)\} = 1$. If it does not, a different nuclear reference density operator can be used, as outlined in Ref. 6.

Breaking down each term in Eq. (S.8), we substitute in $\mathcal{P}^{\text{full}} = \hat{\rho}_n(0) \otimes \text{Tr}_n\{\cdot\}$ and $\mathcal{Q}^{\text{full}} = 1 - \mathcal{P}^{\text{full}}$ (always substituting the furthest right projection operator first, for ease of derivation) and perform a partial trace over the nuclear Hilbert space (Tr_n) for each term:

- LHS:

$$\begin{aligned} \text{Tr}_n \left\{ \frac{d}{dt} \mathcal{P}^{\text{full}} \hat{\rho}(t) \right\} &= \frac{d}{dt} \text{Tr}_n \left\{ \hat{\rho}_n(0) \otimes \underbrace{\text{Tr}_n\{\hat{\rho}(t)\}}_{\hat{\sigma}(t)} \right\} = \frac{d}{dt} \underbrace{\text{Tr}_n \left\{ \hat{\rho}_n(0) \right\}}_1 \otimes \hat{\sigma}(t) \\ &= \boxed{\frac{d}{dt} \hat{\sigma}(t)} \end{aligned}$$

- First term RHS:

$$\text{Tr}_n \left\{ -\frac{i}{\hbar} \mathcal{P}^{\text{full}} \mathcal{L} \mathcal{P}^{\text{full}} \hat{\rho}(t) \right\} = -\frac{i}{\hbar} \text{Tr}_n \left\{ \mathcal{P}^{\text{full}} \mathcal{L} \hat{\rho}_n(0) \otimes \underbrace{\text{Tr}_n\{\hat{\rho}(t)\}}_{\hat{\sigma}(t)} \right\}$$

then we operate the first projection superoperator

$$= -\frac{i}{\hbar} \text{Tr}_n \left\{ \hat{\rho}_n(0) \otimes \text{Tr}_n \left\{ \mathcal{L} \hat{\rho}_n(0) \otimes \hat{\sigma}(t) \right\} \right\}$$

$\hat{\sigma}(t)$ is purely electronic so it can be pulled out of the Tr_n and the inner trace can be pulled out of the outer trace (since it will be purely electronic)

$$\begin{aligned} &= -\frac{i}{\hbar} \underbrace{\text{Tr}_n \left\{ \hat{\rho}_n(0) \right\}}_1 \otimes \text{Tr}_n \left\{ \mathcal{L} \hat{\rho}_n(0) \right\} \hat{\sigma}(t) \\ &= \boxed{-\frac{i}{\hbar} \langle \mathcal{L} \rangle_n^0 \hat{\sigma}(t)} \end{aligned}$$

- Second term RHS:

$$\begin{aligned}
\text{Tr}_n \left\{ \frac{i}{\hbar} \mathcal{P}^{\text{full}} \mathcal{L} e^{-i\mathcal{Q}^{\text{full}} \mathcal{L} t / \hbar} \mathcal{Q}^{\text{full}} \hat{\rho}(0) \right\} &= \text{Tr}_n \left\{ \frac{i}{\hbar} \mathcal{P}^{\text{full}} \mathcal{L} e^{-i\mathcal{Q}^{\text{full}} \mathcal{L} t / \hbar} (1 - \mathcal{P}^{\text{full}}) \hat{\rho}(0) \right\} \\
&= \text{Tr}_n \left\{ \frac{i}{\hbar} \mathcal{P}^{\text{full}} \mathcal{L} e^{-i\mathcal{Q}^{\text{full}} \mathcal{L} t / \hbar} \left(\hat{\rho}(0) - \hat{\rho}_n(0) \otimes \underbrace{\text{Tr}_n \{ \hat{\rho}(0) \}}_{\hat{\sigma}(t)} \right) \right\} \\
&= \text{Tr}_n \left\{ \frac{i}{\hbar} \mathcal{P}^{\text{full}} \mathcal{L} e^{-i\mathcal{Q}^{\text{full}} \mathcal{L} t / \hbar} \left(\underbrace{\hat{\rho}(0)}_{\hat{\rho}_n(0) \otimes \hat{\sigma}(0)} - \hat{\rho}_n(0) \otimes \hat{\sigma}(0) \right) \right\} \\
&= \boxed{0}
\end{aligned}$$

- Third term RHS:

$$\begin{aligned}
&\text{Tr}_n \left\{ \frac{1}{\hbar^2} \int_0^t d\tau \mathcal{P}^{\text{full}} \mathcal{L} e^{-i\mathcal{Q}^{\text{full}} \mathcal{L} \tau / \hbar} \mathcal{Q}^{\text{full}} \mathcal{L} \mathcal{P}^{\text{full}} \hat{\rho}(t - \tau) \right\} \\
&= \int_0^t d\tau \frac{1}{\hbar^2} \text{Tr}_n \left\{ \mathcal{P}^{\text{full}} \mathcal{L} e^{-i\mathcal{Q}^{\text{full}} \mathcal{L} \tau / \hbar} \mathcal{Q}^{\text{full}} \mathcal{L} \hat{\rho}_n(0) \otimes \underbrace{\text{Tr}_n \{ \hat{\rho}(t - \tau) \}}_{\hat{\sigma}(t - \tau)} \right\}
\end{aligned}$$

next we substitute the furthest left projection operator

$$= \int_0^t d\tau \frac{1}{\hbar^2} \text{Tr}_n \left\{ \hat{\rho}_n(0) \otimes \text{Tr}_n \left\{ \mathcal{L} e^{-i\mathcal{Q}^{\text{full}} \mathcal{L} \tau / \hbar} \mathcal{Q}^{\text{full}} \mathcal{L} \hat{\rho}_n(0) \right\} \right\} \hat{\sigma}(t - \tau)$$

taking the inner trace out of the outer trace and using $\text{Tr}_n \{ \hat{\rho}_n(0) \} = 1$ leads to

$$= \int_0^t d\tau \frac{1}{\hbar^2} \underbrace{\text{Tr}_n \left\{ \mathcal{L} e^{-i\mathcal{Q}^{\text{full}} \mathcal{L} \tau / \hbar} \mathcal{Q}^{\text{full}} \mathcal{L} \hat{\rho}_n(0) \right\}}_{\mathcal{K}^{\text{full}}(\tau)} \hat{\sigma}(t - \tau)$$

Putting these terms back together yields the following equation of motion, or GQME, for $\hat{\sigma}(t)$.⁶

$$\frac{d}{dt} \hat{\sigma}(t) = -\frac{i}{\hbar} \langle \mathcal{L} \rangle_n^0 \hat{\sigma}(t) - \int_0^t d\tau \mathcal{K}^{\text{full}}(\tau) \hat{\sigma}(t - \tau). \quad (\text{S.11})$$

Within this GQME, the effect of the projected-out nuclear DOF on the dynamics of $\hat{\sigma}(t)$ is fully accounted for by two electronic superoperators:

- *The projected Liouvillian,*

$$\langle \mathcal{L} \rangle_n^0 \equiv \text{Tr}_n \{ \hat{\rho}_n(0) \mathcal{L} \} \quad (\text{S.12})$$

which can be represented by a *time-independent* $N_e^2 \times N_e^2$ matrix, and

- *The memory kernel,*

$$\mathcal{K}^{\text{full}}(\tau) = \frac{1}{\hbar^2} \text{Tr}_n \left\{ \mathcal{L} e^{-i\mathcal{Q}^{\text{full}}\mathcal{L}\tau/\hbar} \mathcal{Q}^{\text{full}} \mathcal{L} \hat{\rho}_n(0) \right\}, \quad (\text{S.13})$$

which can be represented by a *time-dependent* $N_e^2 \times N_e^2$ matrix.

While calculating the matrix elements of $\langle \mathcal{L} \rangle_n^0$ is straightforward, this is not the case for the matrix elements of $\mathcal{K}^{\text{full}}(\tau)$. The memory kernel of the GQME cannot be obtained directly due to its projected dynamics, seen in the presence of the projection operator \mathcal{Q} in its exponential, $e^{-i\mathcal{Q}\mathcal{L}\tau/\hbar}$ [see Eq. (S.13)]. Significant effort over the last two decades has been directed at developing, testing, and applying various computational schemes for calculating $\mathcal{K}^{\text{full}}(\tau)$. Those schemes were all based on the fact that $\mathcal{K}^{\text{full}}(\tau)$ can be obtained from projection-free inputs (PFIs) by solving integral Volterra equations, as was first shown in Refs. 8–11. The PFIs can be calculated using either quantum-mechanically exact or approximate semiclassical and mixed quantum-classical input methods.^{8–23,6,24,25,5} Additional studies advanced the understanding of the pros and cons of different implementations and expanded the range of applications of such GQMEs.^{12–23,6,24,25,5} Further details on obtaining the M-GQME memory kernel from projection-free inputs will be outlined in Sec. S.II.

S.I.2 Reduced-Dimensionality GQMEs

In this section, we explore an alternative approach for scaling up the GQME approach which is based on utilizing the flexibility offered by the GQME formalism with respect to the choice of projection operator. To this end, we use the fact that it is possible to derive a GQME for *any* subset of electronic reduced density matrix elements of one's choice. It should be noted that a similar approach has been previously discussed in Refs. 26 and 19.

In this subsection, we consider the case where the electronic observables of interest correspond to a subset of the electronic reduced density matrix elements, $\{\sigma_{ab}(t)\}$. The equation of motion for $\{\sigma_{ab}(t)\}$ is obtained by using the following projection superoperator:

$$\mathcal{P}^{\text{set}} \hat{A} = \sum_{jk \in \{ab\}} \mathcal{P}^{jk} \hat{A} = \sum_{jk \in \{ab\}} \hat{\rho}_n(0) \otimes |j\rangle \langle k| \text{Tr} \left\{ \left(|k\rangle \langle j| \otimes \hat{\mathbb{I}}_n \right) \hat{A} \right\}. \quad (\text{S.14})$$

For ease of the derivation later, we note that this projection operator when applied to the overall

system density operator gives

$$\begin{aligned}
\mathcal{P}^{\text{set}} \hat{\rho}(t) &= \sum_{jk \in \{ab\}} \hat{\rho}_n(0) \otimes |j\rangle\langle k| \text{Tr} \left\{ \left(|k\rangle\langle j| \otimes \hat{1}_n \right) \hat{\rho}(t) \right\} \\
&= \sum_{jk \in \{ab\}} \hat{\rho}_n(0) \otimes |j\rangle\langle k| \text{Tr}_e \left\{ \langle j| \text{Tr}_n \left\{ \hat{1}_n \hat{\rho}(t) \right\} |k\rangle \right\} \\
&= \sum_{jk \in \{ab\}} \hat{\rho}_n(0) \otimes |j\rangle\langle k| \text{Tr}_e \left\{ \langle j| \hat{\sigma}(t) |k\rangle \right\} \\
&= \hat{\rho}_n(0) \otimes |j\rangle\langle k| \sigma_{jk}(t)
\end{aligned} \tag{S.15}$$

For the derivation of the subset GQME, we first write Eq. (S.8) with \mathcal{P}^{set} and split into terms:

$$\begin{aligned}
\underbrace{\frac{d}{dt} \mathcal{P}^{\text{set}} \hat{\rho}(t)}_{(1)} &= \underbrace{-\frac{i}{\hbar} \mathcal{P}^{\text{set}} \mathcal{L} \mathcal{P}^{\text{set}} \hat{\rho}(t)}_{(2)} - \underbrace{\frac{1}{\hbar^2} \int_0^t d\tau \mathcal{P}^{\text{set}} \mathcal{L} e^{-i\mathcal{Q}^{\text{set}} \mathcal{L} \tau / \hbar} \mathcal{Q}^{\text{set}} \mathcal{L} \mathcal{P}^{\text{set}} \hat{\rho}(t - \tau)}_{(3)} \\
&\quad - \underbrace{\frac{i}{\hbar} \mathcal{P}^{\text{set}} \mathcal{L} e^{-i\mathcal{Q}^{\text{set}} \mathcal{L} t / \hbar} \mathcal{Q}^{\text{set}} \hat{\rho}(0)}_{(4)},
\end{aligned} \tag{S.16}$$

where $\mathcal{Q}^{\text{set}} = 1 - \mathcal{P}^{\text{set}}$ is the complimentary projection operator to \mathcal{P}^{set} (i.e., \mathcal{Q}^{set} projects-in what \mathcal{P}^{set} projects-out).

Plugging in the projection operator from Eq. (S.14) [always starting with the furthest right projection operator and using Eq. (S.15): $\mathcal{P}^{\text{set}} \hat{\rho}(t) = \hat{\rho}_n(0) \otimes |j\rangle\langle k| \sigma_{jk}(t)$] and tracing over the nuclear DOF, we get the following for each term:

$$\begin{aligned}
(1) \quad \text{Tr}_n \left\{ \frac{d}{dt} \mathcal{P}^{\text{set}} \hat{\rho}(t) \right\} &= \frac{d}{dt} \text{Tr}_n \left\{ \sum_{jk \in \{ab\}} \hat{\rho}_n(0) \otimes |j\rangle\langle k| \sigma_{jk}(t) \right\} \\
&= \frac{d}{dt} \sum_{jk \in \{ab\}} \text{Tr}_n \left\{ \hat{\rho}_n(0) \right\} |j\rangle\langle k| \sigma_{jk}(t) \\
&= \boxed{\sum_{jk \in \{ab\}} |j\rangle\langle k| \frac{d}{dt} \sigma_{jk}(t)}
\end{aligned} \tag{S.17}$$

(2)

$$\begin{aligned}
\text{Tr}_n \left\{ -\frac{i}{\hbar} \mathcal{P}^{\text{set}} \mathcal{L} \mathcal{P}^{\text{set}} \hat{\rho}(t) \right\} &= -\frac{i}{\hbar} \text{Tr}_n \left\{ \mathcal{P}^{\text{set}} \mathcal{L} \sum_{lm \in \{ab\}} \hat{\rho}_n(0) \otimes |l\rangle\langle m| \sigma_{lm}(t) \right\} \\
&= -\frac{i}{\hbar} \sum_{\substack{jk \in \{ab\} \\ lm \in \{ab\}}} \text{Tr}_n \left\{ |j\rangle\langle k| \otimes \hat{\rho}_n(0) \underbrace{\text{Tr} \left\{ \left(|k\rangle\langle j| \otimes \hat{\mathbf{I}}_n \right) \mathcal{L} \hat{\rho}_n(0) |l\rangle\langle m| \right\}}_{\left\langle \mathcal{L}_{jk,lm} \right\rangle_n^0} \right\} \sigma_{lm}(t) \right\}
\end{aligned}$$

the Tr_n can pass over $|j\rangle\langle k|$ because it is purely electronic and it can pass over $\langle \mathcal{L}_{jk,lm} \rangle_n^0$ and $\sigma_{lm}(t)$ because they are numbers

$$\begin{aligned}
&= -\frac{i}{\hbar} \sum_{\substack{jk \in \{ab\} \\ lm \in \{ab\}}} |j\rangle\langle k| \underbrace{\text{Tr}_n \left\{ \hat{\rho}_n(0) \right\}}_1 \left\langle \mathcal{L}_{jk,lm} \right\rangle_n^0 \sigma_{lm}(t) \\
&= \boxed{-\frac{i}{\hbar} \sum_{\substack{jk \in \{ab\} \\ lm \in \{ab\}}} |j\rangle\langle k| \left\langle \mathcal{L}_{jk,lm} \right\rangle_n^0 \sigma_{lm}(t)} \tag{S.18}
\end{aligned}$$

(3)

$$\begin{aligned} \text{Tr}_n \left\{ -\frac{1}{\hbar^2} \int_0^t d\tau \mathcal{P}^{\text{set}} \mathcal{L} e^{-i\mathcal{Q}^{\text{set}} \mathcal{L} \tau / \hbar} \mathcal{Q}^{\text{set}} \mathcal{L} \mathcal{P}^{\text{set}} \hat{\rho}(t - \tau) \right\} \\ = - \int_0^t d\tau \frac{1}{\hbar^2} \text{Tr}_n \left\{ \mathcal{P}^{\text{set}} \mathcal{L} e^{-i\mathcal{Q}^{\text{set}} \mathcal{L} \tau / \hbar} \mathcal{Q}^{\text{set}} \mathcal{L} \sum_{lm \in \{ab\}} \hat{\rho}_n(0) \otimes |l\rangle\langle m| \sigma_{lm}(t - \tau) \right\} \end{aligned}$$

next, plugging in the furthest left projection operator

$$\begin{aligned} = - \int_0^t d\tau \sum_{\substack{jk \in \{ab\} \\ lm \in \{ab\}}} \frac{1}{\hbar^2} \text{Tr}_n \left\{ |j\rangle\langle k| \otimes \hat{\rho}_n(0) \right. \\ \left. \times \text{Tr} \left\{ \left(|k\rangle\langle j| \otimes \hat{1}_n \right) \mathcal{L} e^{-i\mathcal{Q}^{\text{set}} \mathcal{L} \tau / \hbar} \mathcal{Q}^{\text{set}} \mathcal{L} \hat{\rho}_n(0) \otimes |l\rangle\langle m| \sigma_{lm}(t - \tau) \right\} \right\} \end{aligned}$$

the Tr_n can pass over $|j\rangle\langle k|$ because it is purely electronic and

it can pass over the full trace because it is a number

$$\begin{aligned} = - \int_0^t d\tau \sum_{\substack{jk \in \{ab\} \\ lm \in \{ab\}}} |j\rangle\langle k| \underbrace{\text{Tr}_n \left\{ \hat{\rho}_n(0) \right\}}_1 \\ \times \frac{1}{\hbar^2} \text{Tr} \left\{ \left(|k\rangle\langle j| \otimes \hat{1}_n \right) \mathcal{L} e^{-i\mathcal{Q}^{\text{set}} \mathcal{L} \tau / \hbar} \mathcal{Q}^{\text{set}} \mathcal{L} \hat{\rho}_n(0) \otimes |l\rangle\langle m| \sigma_{lm}(t - \tau) \right\} \end{aligned}$$

the $\sigma_{lm}(t - \tau)$ can be taken out of the full trace because it is a number

$$\begin{aligned} = - \sum_{\substack{jk \in \{ab\} \\ lm \in \{ab\}}} |j\rangle\langle k| \int_0^t d\tau \frac{1}{\hbar^2} \text{Tr} \left\{ \underbrace{\left(|k\rangle\langle j| \otimes \hat{1}_n \right) \mathcal{L} e^{-i\mathcal{Q}^{\text{set}} \mathcal{L} \tau / \hbar} \mathcal{Q}^{\text{set}} \mathcal{L} \left(\hat{\rho}_n(0) \otimes |l\rangle\langle m| \right)}_{\mathcal{K}_{jk,lm}^{\text{set}}(\tau)} \right\} \sigma_{lm}(t - \tau) \end{aligned}$$

(S.19)

(4)

$$\begin{aligned}
\text{Tr}_n \left\{ -\frac{i}{\hbar} \mathcal{P}^{\text{set}} \mathcal{L} e^{-i\mathcal{Q}^{\text{set}} \mathcal{L} t / \hbar} \mathcal{Q}^{\text{set}} \hat{\rho}(0) \right\} &= -\frac{i}{\hbar} \text{Tr}_n \left\{ \mathcal{P}^{\text{set}} \mathcal{L} e^{-i\mathcal{Q}^{\text{set}} \mathcal{L} t / \hbar} (1 - \mathcal{P}^{\text{set}}) \hat{\rho}(0) \right\} \\
&\quad \text{distributing } (1 - \mathcal{P}^{\text{set}}) \hat{\rho}(0) \\
&= -\frac{i}{\hbar} \text{Tr}_n \left\{ \mathcal{P}^{\text{set}} \mathcal{L} e^{-i\mathcal{Q}^{\text{set}} \mathcal{L} t / \hbar} \left[\hat{\rho}(0) - \sum_{lm \in \{ab\}} \hat{\rho}_n(0) \otimes |l\rangle \langle m| \sigma_{lm}(0) \right] \right\} \\
&\quad \text{plugging in the furthest left projection operator} \\
&= -\frac{i}{\hbar} \sum_{jk \in \{ab\}} \text{Tr}_n \left\{ |j\rangle \langle k| \otimes \hat{\rho}_n(0) \text{Tr} \left\{ (|k\rangle \langle j| \otimes \hat{1}_n) \mathcal{L} e^{-i\mathcal{Q}^{\text{set}} \mathcal{L} t / \hbar} \left[\hat{\rho}(0) - \sum_{lm \in \{ab\}} \hat{\rho}_n(0) \otimes |l\rangle \langle m| \sigma_{lm}(0) \right] \right\} \right\} \\
&\quad \text{the } \text{Tr}_n \text{ can pass over } |j\rangle \langle k| \text{ because it is purely electronic and} \\
&\quad \text{it can pass over the full trace because it is a number} \\
&= -\frac{i}{\hbar} \sum_{jk \in \{ab\}} |j\rangle \langle k| \underbrace{\text{Tr}_n \left\{ \hat{\rho}_n(0) \right\}}_1 \text{Tr} \left\{ (|k\rangle \langle j| \otimes \hat{1}_n) \mathcal{L} e^{-i\mathcal{Q}^{\text{set}} \mathcal{L} t / \hbar} \left[\hat{\rho}(0) - \sum_{lm \in \{ab\}} \hat{\rho}_n(0) \otimes |l\rangle \langle m| \sigma_{lm}(0) \right] \right\} \\
&= \sum_{jk \in \{ab\}} |j\rangle \langle k| \underbrace{\left[-\frac{i}{\hbar} \text{Tr} \left\{ (|k\rangle \langle j| \otimes \hat{1}_n) \mathcal{L} e^{-i\mathcal{Q}^{\text{set}} \mathcal{L} t / \hbar} \left[\hat{\rho}(0) - \sum_{lm \in \{ab\}} \hat{\rho}_n(0) \otimes |l\rangle \langle m| \sigma_{lm}(0) \right] \right\} \right]}_{I_{jk}^{\text{set}}(t)} \\
\end{aligned} \tag{S.20}$$

So this term goes to zero if $\hat{\rho}_n(0) = \sum_{lm \in \{ab\}} \hat{\rho}_n(0) \otimes \sigma_{lm}(0) |l\rangle \langle m|$. This can often easily be true if the system starts in one population, with the rest equal to zero, and this population is included in the subset of states of interest. In other words, if $\hat{\rho}(0) = \hat{\rho}_n(0) \otimes |\alpha\rangle \langle \alpha|$ and $\alpha \in \{ab\}$, then $I_{jk}^{\text{set}}(t) = 0$.

Therefore, the overall GQME is given by

$$\begin{aligned}
\sum_{jk \in \{ab\}} |j\rangle \langle k| \frac{d}{dt} \sigma_{jk}(t) &= -\frac{i}{\hbar} \sum_{\substack{jk \in \{ab\} \\ lm \in \{ab\}}} |j\rangle \langle k| \langle \mathcal{L}_{jk,lm} \rangle_n^0 \sigma_{lm}(t) \\
&\quad - \sum_{\substack{jk \in \{ab\} \\ lm \in \{ab\}}} |j\rangle \langle k| \int_0^t d\tau \mathcal{K}_{jk,lm}^{\text{set}}(\tau) \sigma_{lm}(t - \tau) + \sum_{jk \in \{ab\}} |j\rangle \langle k| \hat{I}_{jk}^{\text{set}}(t),
\end{aligned} \tag{S.21}$$

where the memory kernel matrix elements are given by

$$\mathcal{K}_{jk,lm}^{\text{set}}(\tau) = \frac{1}{\hbar^2} \text{Tr} \left\{ \left(|k\rangle\langle j| \otimes \hat{1}_n \right) \mathcal{L} e^{-i\mathcal{Q}^{\text{set}} \mathcal{L} \tau / \hbar} \mathcal{Q}^{\text{set}} \mathcal{L} \hat{\rho}_n(0) \otimes |l\rangle\langle m| \right\} \quad (\text{S.22})$$

and the inhomogeneous term vector elements are given by

$$\hat{I}_{jk}^{\text{set}}(t) = -\frac{i}{\hbar} \text{Tr} \left\{ \left(|k\rangle\langle j| \otimes \hat{1}_n \right) \mathcal{L} e^{-i\mathcal{Q}^{\text{set}} \mathcal{L} t / \hbar} \left[\hat{\rho}(0) - \sum_{lm \in \{ab\}} \hat{\rho}_n(0) \otimes |l\rangle\langle m| \sigma_{lm}(0) \right] \right\}. \quad (\text{S.23})$$

Given N_{set} equal to the number of elements in $\{\sigma_{ab}(t)\}$, the memory kernel and inhomogeneous term in this case correspond to an $N_{\text{set}} \times N_{\text{set}}$ matrix and an N_{set} -dimensional vector, respectively. If the initial state is of the commonly encountered factored form $\hat{\rho}(0) = \hat{\rho}_n(0) \otimes |\alpha\rangle\langle\beta|$ and $\alpha\beta \in \{ab\}$, then $\hat{I}^{\text{set}}(t) = 0$.

S.II Projection-Free Inputs

The memory kernels and inhomogeneous terms of the M-GQME and reduced-dimensionality GQMEs can be found via integral Volterra equations with PFIs.

For the M-GQME, a scheme for evaluating $\mathcal{K}^{\text{full}}(\tau)$ from projection-free inputs can be developed by using the following general operator identity:^{8,10}

$$e^{-i\mathcal{B}\tau/\hbar} = e^{-i\mathcal{A}\tau/\hbar} - \frac{i}{\hbar} \int_0^\tau d\tau' e^{-i\mathcal{A}(\tau-\tau')/\hbar} (\mathcal{B} - \mathcal{A}) e^{-i\mathcal{B}\tau'/\hbar}. \quad (\text{S.24})$$

The proof of this identity can be shown by first starting with the differential equation

$$\begin{aligned} \frac{d}{d\tau} e^{i\mathcal{A}\tau/\hbar} e^{-i\mathcal{B}\tau/\hbar} &= \left(\frac{i}{\hbar} \mathcal{A} e^{i\mathcal{A}\tau/\hbar} \right) e^{-i\mathcal{B}\tau/\hbar} + e^{i\mathcal{A}\tau/\hbar} \left(-\frac{i}{\hbar} \mathcal{B} e^{-i\mathcal{B}\tau/\hbar} \right) \quad \text{product rule} \\ &= \frac{i}{\hbar} e^{i\mathcal{A}\tau/\hbar} (\mathcal{A} - \mathcal{B}) e^{-i\mathcal{B}\tau/\hbar}. \quad \mathcal{A} \text{ and } e^{i\mathcal{A}\tau/\hbar} \text{ commute, then gathering terms} \end{aligned}$$

Integrating both sides from 0 to t leads to

$$\int_0^t d\tau \frac{d}{d\tau} e^{i\mathcal{A}\tau/\hbar} e^{-i\mathcal{B}\tau/\hbar} = \int_0^t d\tau \frac{i}{\hbar} e^{i\mathcal{A}\tau/\hbar} (\mathcal{A} - \mathcal{B}) e^{-i\mathcal{B}\tau/\hbar}$$

evaluating the LHS and flipping the sign of the integral on the RHS

$$e^{i\mathcal{A}t/\hbar} e^{-i\mathcal{B}t/\hbar} - 1 = -\frac{i}{\hbar} \int_0^t d\tau e^{i\mathcal{A}\tau/\hbar} (\mathcal{B} - \mathcal{A}) e^{-i\mathcal{B}\tau/\hbar}$$

multiplying from the left with $e^{-i\mathcal{A}t/\hbar}$ and moving the second term on the LHS to the RHS

$$e^{-i\mathcal{B}t/\hbar} = e^{-i\mathcal{A}t/\hbar} - \frac{i}{\hbar} \int_0^t d\tau e^{-i\mathcal{A}(t-\tau)/\hbar} (\mathcal{B} - \mathcal{A}) e^{-i\mathcal{B}\tau/\hbar} \quad (\text{S.25})$$

This is equivalent to Eq. (S.24), proving the general operator identity.

Substituting $\mathcal{A} = \mathcal{L}$ and $\mathcal{B} = \mathcal{Q}\mathcal{L}$ into Eq. (S.24), we obtain

$$e^{-i\mathcal{Q}\mathcal{L}\tau/\hbar} = e^{-i\mathcal{L}\tau/\hbar} + \frac{i}{\hbar} \int_0^\tau d\tau' e^{-i\mathcal{L}(\tau-\tau')/\hbar} \mathcal{P} \mathcal{L} e^{-i\mathcal{Q}\mathcal{L}\tau'/\hbar}. \quad (\text{S.26})$$

Substituting Eq. (S.26) into Eq. (S.13) gives

$$\begin{aligned} \mathcal{K}^{\text{full}}(\tau) &= \frac{1}{\hbar^2} \text{Tr}_n \left\{ \mathcal{L} e^{-i\mathcal{Q}^{\text{full}}\mathcal{L}\tau/\hbar} \mathcal{Q}^{\text{full}} \mathcal{L} \hat{\rho}_n(0) \right\} \\ &= \frac{1}{\hbar^2} \text{Tr}_n \left\{ \mathcal{L} e^{-i\mathcal{L}\tau/\hbar} \mathcal{Q}^{\text{full}} \mathcal{L} \hat{\rho}_n(0) \right\} \\ &\quad + \frac{i}{\hbar^3} \int_0^\tau d\tau' \text{Tr}_n \left\{ \mathcal{L} e^{-i\mathcal{L}(\tau-\tau')/\hbar} \mathcal{P}^{\text{full}} \mathcal{L} e^{-i\mathcal{Q}^{\text{full}}\mathcal{L}\tau'/\hbar} \mathcal{Q}^{\text{full}} \mathcal{L} \hat{\rho}_n(0) \right\} \end{aligned}$$

plugging in $\mathcal{Q}^{\text{full}} = 1 - \mathcal{P}^{\text{full}}$ in the first term and $\mathcal{P}^{\text{full}}$ into the second term

$$\begin{aligned} &= \frac{1}{\hbar^2} \text{Tr}_n \left\{ \mathcal{L} e^{-i\mathcal{L}\tau/\hbar} (1 - \mathcal{P}^{\text{full}}) \mathcal{L} \hat{\rho}_n(0) \right\} \\ &\quad + \frac{i}{\hbar^3} \int_0^\tau d\tau' \text{Tr}_n \left\{ \mathcal{L} e^{-i\mathcal{L}(\tau-\tau')/\hbar} \hat{\rho}_n(0) \otimes \text{Tr}_n \left\{ \mathcal{L} e^{-i\mathcal{Q}^{\text{full}}\mathcal{L}\tau'/\hbar} \mathcal{Q}^{\text{full}} \mathcal{L} \hat{\rho}_n(0) \right\} \right\} \end{aligned}$$

distributing over the parentheses, plugging in $\mathcal{P}^{\text{full}}$ in the new second term and splitting the nuclear traces in the integral term

$$\begin{aligned} &= \underbrace{\frac{1}{\hbar^2} \text{Tr}_n \left\{ \mathcal{L} e^{-i\mathcal{L}\tau/\hbar} \mathcal{L} \hat{\rho}_n(0) \right\}}_{i\dot{\mathcal{F}}(\tau)} - \frac{1}{\hbar} \underbrace{\frac{1}{\hbar} \text{Tr}_n \left\{ \mathcal{L} e^{-i\mathcal{L}\tau/\hbar} \hat{\rho}_n(0) \right\}}_{\mathcal{F}(\tau)} \underbrace{\text{Tr}_n \left\{ \mathcal{L} \hat{\rho}_n(0) \right\}}_{\langle \mathcal{L} \rangle_n^0} \\ &\quad + i \int_0^\tau d\tau' \underbrace{\frac{1}{\hbar} \text{Tr}_n \left\{ \mathcal{L} e^{-i\mathcal{L}(\tau-\tau')/\hbar} \hat{\rho}_n(0) \right\}}_{\mathcal{F}(\tau-\tau')} \underbrace{\frac{1}{\hbar^2} \text{Tr}_n \left\{ \mathcal{L} e^{-i\mathcal{Q}^{\text{full}}\mathcal{L}\tau'/\hbar} \mathcal{Q}^{\text{full}} \mathcal{L} \hat{\rho}_n(0) \right\}}_{\mathcal{K}^{\text{full}}(\tau')} \end{aligned}$$

Therefore, the full memory kernel can be found by solving the following Volterra equation of the second kind:

$$\mathcal{K}^{\text{full}}(\tau) = i\dot{\mathcal{F}}(\tau) - \frac{1}{\hbar}\mathcal{F}(\tau)\langle\mathcal{L}\rangle_n^0 + i\int_0^\tau d\tau'\mathcal{F}(\tau-\tau')\mathcal{K}^{\text{full}}(\tau'), \quad (\text{S.27})$$

where $\mathcal{F}(\tau)$ and $\dot{\mathcal{F}}(\tau)$ are the PFIs given by

$$\begin{aligned} \mathcal{F}(\tau) &= \frac{1}{\hbar}\text{Tr}_n\left\{\mathcal{L}e^{-i\mathcal{L}\tau/\hbar}\hat{\rho}_n(0)\right\}, \\ \dot{\mathcal{F}}(\tau) &= -\frac{i}{\hbar^2}\text{Tr}_n\left\{\mathcal{L}e^{-i\mathcal{L}\tau/\hbar}\mathcal{L}\hat{\rho}_n(0)\right\}. \end{aligned} \quad (\text{S.28})$$

Thus, given the PFIs, Eq. (S.27) can be solved numerically for the projection-dependent $\mathcal{K}(\tau)$ (see Appendix D of Ref. 6). Hence, the problem of calculating $\mathcal{K}(\tau)$ translates into that of calculating $\mathcal{F}(\tau)$ and $\dot{\mathcal{F}}(\tau)$.

It should be noted that $\mathcal{F}(\tau) = i\dot{\mathcal{U}}(\tau)$, where $\mathcal{U}(\tau)$ is the time evolution operator of the electronic reduced density operator,

$$\hat{\sigma}(\tau) = \mathcal{U}(\tau)\hat{\sigma}(0) \equiv \text{Tr}_n\left\{e^{-i\mathcal{L}\tau/\hbar}\hat{\rho}_n(0)\right\}\hat{\sigma}(0). \quad (\text{S.29})$$

Thus, Eq. (S.27) can be rewritten in the following form:

$$\mathcal{K}^{\text{full}}(\tau) = -\ddot{\mathcal{U}}(\tau) - \frac{i}{\hbar}\dot{\mathcal{U}}(\tau)\langle\mathcal{L}\rangle_n^0 - \int_0^\tau d\tau'\dot{\mathcal{U}}(\tau-\tau')\mathcal{K}^{\text{full}}(\tau'). \quad (\text{S.30})$$

This implies that the memory kernel of the M-GQME, $\mathcal{K}^{\text{full}}(\tau)$, can be obtained directly from the time evolution operator of the reduced dynamics, $\mathcal{U}(\tau)$. As shown in Ref. 5, when approximate input methods are used, the PFIs $\mathcal{F}(\tau)$ and $\dot{\mathcal{F}}(\tau)$ should be calculated explicitly in order to achieve the accuracy benefit of the GQME. However, with an exact input method, the time evolution operator of the reduced dynamics, $\mathcal{U}(\tau)$, can be used along with a numerical derivative method.

For the reduced-dimensionality GQMEs, the memory kernel $\{\mathcal{K}^{\text{set}}(\tau)\}$ can also be obtained from PFIs by solving a set of N_{set}^2 coupled Volterra equations. We start with the explicit expression for the memory kernel, Eq. (S.22):

$\mathcal{K}_{jk,lm}^{\text{set}}(\tau) = \frac{1}{\hbar^2}\text{Tr}\left\{\left(|k\rangle\langle j|\otimes\hat{\mathbb{1}}_n\right)\mathcal{L}e^{-i\mathcal{Q}^{\text{set}}\mathcal{L}\tau/\hbar}\mathcal{Q}^{\text{set}}\mathcal{L}\hat{\rho}_n(0)\otimes|l\rangle\langle m|\right\}$. We then substitute the identity in Eq. (S.26) for $e^{-i\mathcal{Q}^{\text{set}}\mathcal{L}\tau/\hbar}$ (the identity is valid for any projection superoperator \mathcal{Q}). This yields

the following expression for the matrix elements of $\mathcal{K}^{\text{set}}(\tau)$:

$$\begin{aligned} \mathcal{K}_{jk,lm}^{\text{set}}(\tau) &= \frac{1}{\hbar^2} \text{Tr} \left\{ \left(|k\rangle\langle j| \otimes \hat{1}_n \right) \mathcal{L} e^{-i\mathcal{L}\tau/\hbar} \mathcal{Q}^{\text{set}} \mathcal{L} \hat{\rho}_n(0) \otimes |l\rangle\langle m| \right\} \\ &+ \frac{i}{\hbar^3} \int_0^\tau d\tau' \text{Tr} \left\{ \left(|k\rangle\langle j| \otimes \hat{1}_n \right) \mathcal{L} e^{-i\mathcal{L}(\tau-\tau')/\hbar} \mathcal{P}^{\text{set}} \mathcal{L} e^{-i\mathcal{Q}^{\text{set}}\mathcal{L}\tau'/\hbar} \mathcal{Q}^{\text{set}} \mathcal{L} \hat{\rho}_n(0) \otimes |l\rangle\langle m| \right\}. \end{aligned}$$

Plugging in $\mathcal{Q}^{\text{set}} = 1 - \mathcal{P}^{\text{set}}$ into the first term splits it into two terms. Using \mathcal{P}^{set} from Eq. (S.14) in the term that involves \mathcal{P}^{set} leads to Eq. (S.31):

$$\begin{aligned} \mathcal{K}_{jk,lm}^{\text{set}}(\tau) &= \frac{1}{\hbar^2} \text{Tr} \left\{ \left(|k\rangle\langle j| \otimes \hat{1}_n \right) \mathcal{L} e^{-i\mathcal{L}\tau/\hbar} \mathcal{L} \hat{\rho}_n(0) \otimes |l\rangle\langle m| \right\} \\ &\quad \underbrace{\hspace{10em}}_{i\dot{\mathcal{F}}_{jk,lm}(\tau)} \\ &- \frac{1}{\hbar} \sum_{uv \in \{ab\}} \frac{1}{\hbar} \text{Tr} \left\{ \left(|j\rangle\langle j| \otimes \hat{1}_n \right) \mathcal{L} e^{-i\mathcal{L}\tau/\hbar} \hat{\rho}_n(0) \otimes |u\rangle\langle v| \right\} \underbrace{\text{Tr} \left\{ \left(|v\rangle\langle u| \otimes \hat{1}_n \right) \mathcal{L} \hat{\rho}_n(0) \otimes |l\rangle\langle m| \right\}}_{\langle \mathcal{L}_{uv,lm} \rangle_n^0} \\ &+ i \sum_{uv \in \{ab\}} \int_0^\tau d\tau' \frac{1}{\hbar} \text{Tr} \left\{ \left(|k\rangle\langle j| \otimes \hat{1}_n \right) \mathcal{L} e^{-i\mathcal{L}(\tau-\tau')/\hbar} \hat{\rho}_n(0) \otimes |u\rangle\langle v| \right\} \\ &\quad \underbrace{\hspace{10em}}_{\mathcal{F}_{jk,uv}(\tau-\tau')} \\ &\quad \times \frac{1}{\hbar^2} \text{Tr} \left\{ \left(|v\rangle\langle u| \otimes \hat{1}_n \right) \mathcal{L} e^{-i\mathcal{Q}^{\text{set}}\mathcal{L}\tau'/\hbar} \mathcal{Q}^{\text{set}} \mathcal{L} \hat{\rho}_n(0) \otimes |l\rangle\langle m| \right\} \\ &\quad \underbrace{\hspace{10em}}_{\mathcal{K}_{uv,lm}^{\text{set}}(\tau')}. \end{aligned}$$

Therefore, the Volterra equation for the subset memory kernel is given by

$$\mathcal{K}_{jk,lm}^{\text{set}}(\tau) = i\dot{\mathcal{F}}_{jk,lm}(\tau) - \frac{1}{\hbar} \sum_{uv \in \{ab\}} \mathcal{F}_{jk,uv}(\tau) \langle \mathcal{L}_{uv,lm} \rangle_n^0 + i \sum_{uv \in \{ab\}} \int_0^\tau d\tau' \mathcal{F}_{jk,uv}(\tau-\tau') \mathcal{K}_{uv,lm}^{\text{set}}(\tau') \quad (\text{S.31})$$

Note that $\langle \mathcal{L}_{jj,kk} \rangle_n^0 = 0$.

Since the PFIs can be written in terms of the time evolution operator $\mathcal{U}(\tau)$, this means that Eq. (S.31) can be rewritten in terms of the time evolution operator for the reduced electronic density operator:

$$\mathcal{K}_{jk,lm}^{\text{set}}(\tau) = -\ddot{\mathcal{U}}_{jk,lm}(\tau) - \frac{i}{\hbar} \sum_{uv \in \{ab\}} \dot{\mathcal{U}}_{jk,uv}(\tau) \langle \mathcal{L}_{uv,lm} \rangle_n^0 - \sum_{uv \in \{ab\}} \int_0^\tau d\tau' \dot{\mathcal{U}}_{jk,uv}(\tau-\tau') \mathcal{K}_{uv,lm}^{\text{set}}(\tau'). \quad (\text{S.32})$$

Next, we consider the explicit expression for the inhomogeneous term, Eq. (S.23). We

substitute the identity in Eq. (S.26) for $e^{-i\mathcal{Q}^{\text{set}}\mathcal{L}\tau/\hbar}$, which yields:

$$I_{jk}^{\text{set}}(t) = -\frac{i}{\hbar} \text{Tr} \left\{ \left(|k\rangle\langle j| \otimes \hat{1}_n \right) \mathcal{L} e^{-i\mathcal{L}t/\hbar} \left[\hat{\rho}(0) - \sum_{lm \in \{ab\}} \hat{\rho}_n(0) \otimes |l\rangle\langle m| \sigma_{lm}(0) \right] \right\} \\ + \frac{1}{\hbar^2} \int_0^t d\tau \text{Tr} \left\{ \left(|k\rangle\langle j| \otimes \hat{1}_n \right) \mathcal{L} e^{-i\mathcal{L}(t-\tau)/\hbar} \mathcal{P}^{\text{set}} \mathcal{L} e^{-i\mathcal{Q}^{\text{set}}\mathcal{L}\tau/\hbar} \left[\hat{\rho}(0) - \sum_{lm \in \{ab\}} \hat{\rho}_n(0) \otimes |l\rangle\langle m| \sigma_{lm}(0) \right] \right\}.$$

Splitting the first term into two terms at the minus sign and plugging \mathcal{P}^{set} from Eq. (S.14) into the second term leads to Eq. (S.33)

$$I_{jk}^{\text{set}}(t) = \underbrace{-\frac{i}{\hbar} \text{Tr} \left\{ \left(|k\rangle\langle j| \otimes \hat{1}_n \right) \mathcal{L} e^{-i\mathcal{L}t/\hbar} \hat{\rho}(0) \right\}}_{= Z_{jk}(t)} \\ + i \sum_{lm \in \{ab\}} \frac{1}{\hbar} \text{Tr} \left\{ \left(|k\rangle\langle j| \otimes \hat{1}_n \right) \mathcal{L} e^{-i\mathcal{L}t/\hbar} \hat{\rho}_n(0) \otimes |l\rangle\langle m| \right\} \sigma_{lm}(0) \\ = \mathcal{F}_{jk,lm}(t) \\ + i \sum_{uv \in \{ab\}} \int_0^t d\tau \frac{1}{\hbar} \text{Tr} \left\{ \left(|k\rangle\langle j| \otimes \hat{1}_n \right) \mathcal{L} e^{-i\mathcal{L}(t-\tau)/\hbar} \hat{\rho}_n(0) \otimes |u\rangle\langle v| \right\} \\ = \mathcal{F}_{jk,uv}(t-\tau) \\ \times \underbrace{\left[-\frac{i}{\hbar} \text{Tr} \left\{ \left(|\lambda\rangle\langle \lambda| \otimes \hat{1}_n \right) \mathcal{L} e^{-i\mathcal{Q}^{\text{set}}\mathcal{L}\tau/\hbar} \left[\hat{\rho}(0) - \sum_{lm \in \{ab\}} \hat{\rho}_n(0) \otimes |k\rangle\langle k| \sigma_{kk}(0) \right] \right\} \right]}_{I_{uv}^{\text{set}}(\tau)}. \\ I_{jk}^{\text{set}}(t) = Z_{jk}(t) + i \sum_{lm \in \{ab\}} \mathcal{F}_{jk,lm}(t) \sigma_{lm}(0) + i \sum_{uv \in \{ab\}} \int_0^t d\tau \mathcal{F}_{jk,uv}(t-\tau) I_{uv}^{\text{set}}(\tau). \quad (\text{S.33})$$

Here, $\{Z_{jk}(t)\}$ is given by

$$Z_{jk}(t) = -\frac{i}{\hbar} \text{Tr} \left\{ \left(|k\rangle\langle j| \otimes \hat{1}_n \right) \mathcal{L} e^{-i\mathcal{L}t/\hbar} \hat{\rho}(0) \right\}. \quad (\text{S.34})$$

If the overall initial state is of the commonly encountered form $\hat{\rho}(0) = \hat{\rho}_n(0) \otimes |\alpha\rangle\langle\alpha|$, then $Z_{jk}(t)$ is equivalent to $-i\mathcal{F}_{jk,\alpha\alpha}(t) = \dot{\mathcal{U}}_{jk,\alpha\alpha}(t)$.

S.III Equivalence between the TFD Schrödinger equation and the quantum Liouville equation

In this section, we show that when the thermal wavepacket $|\psi_\gamma(\beta, t)\rangle$ is defined such that

$$\hat{\rho}(t) = \text{Tr}_f \left\{ |\psi_\gamma(\beta, t)\rangle \langle \psi_\gamma(\beta, t)| \right\}, \quad (\text{S.35})$$

and evolves according to the so-called TFD Schrödinger equation:

$$\frac{d}{dt} |\psi_\gamma(\beta, t)\rangle = -\frac{i}{\hbar} \bar{H} |\psi_\gamma(\beta, t)\rangle, \quad (\text{S.36})$$

where $\bar{H} = \hat{H} \otimes \tilde{\mathbb{I}}_n$, then $\hat{\rho}(t)$ correctly evolves according to the quantum Liouville equation.

To see this, take the time derivative on both sides of Eq. (S.35), we obtain:

$$\frac{d}{dt} \hat{\rho}(t) = \text{Tr}_f \left[\left(\frac{d}{dt} |\psi_\gamma(\beta, t)\rangle \right) \langle \psi_\gamma(\beta, t)| + |\psi_\gamma(\beta, t)\rangle \left(\frac{d}{dt} \langle \psi_\gamma(\beta, t)| \right) \right]. \quad (\text{S.37})$$

Plugging Eq. (S.36) into the right hand side of Eq. (S.37), we obtain:

$$\frac{d}{dt} \hat{\rho}(t) = \text{Tr}_f \left[-\frac{i}{\hbar} (\hat{H} \otimes \tilde{\mathbb{I}}_n) |\psi_\gamma(\beta, t)\rangle \langle \psi_\gamma(\beta, t)| + |\psi_\gamma(\beta, t)\rangle \langle \psi_\gamma(\beta, t)| \frac{i}{\hbar} (\hat{H} \otimes \tilde{\mathbb{I}}_n) \right]. \quad (\text{S.38})$$

Pulling \hat{H} out of the partial trace with $\text{Tr}_f[(\hat{H} \otimes \tilde{\mathbb{I}}_n)\bar{B}] = \hat{H}\text{Tr}_f[\bar{B}]$ for any double space operator \bar{B} ,

$$\begin{aligned} \frac{d}{dt} \hat{\rho}(t) &= -\frac{i}{\hbar} \hat{H} \text{Tr}_f[|\psi_\gamma(\beta, t)\rangle \langle \psi_\gamma(\beta, t)|] + \text{Tr}_f[|\psi_\gamma(\beta, t)\rangle \langle \psi_\gamma(\beta, t)|] \frac{i}{\hbar} \hat{H} \\ &= -\frac{i}{\hbar} [\hat{H}, \hat{\rho}(t)], \end{aligned} \quad (\text{S.39})$$

which is the quantum Liouville equation.

S.IV Linear Combinations for Off-Diagonal Initial States of $\mathcal{U}(t)$

The TT-TFD method requires the initial electronic state to be in a pure state, e.g., $|\gamma\rangle\langle\gamma|$. However, in order to obtain the time evolution operator of the electronic reduced density matrix, $\mathcal{U}(t)$, necessary for obtaining the PFIs, we need to start in off-diagonal initial states, e.g., $\hat{\sigma}(0) = |u\rangle\langle v|$ when $u \neq v$. This problem can be bypassed by starting in a set of pure states and using linear combinations to calculate the off-diagonal initial states. The choice of the set of initial states

is not unique but a relatively unbiased choice is

$$\begin{aligned}\hat{X}_{uv} &= \frac{1}{2} \left[|u\rangle\langle u| + |v\rangle\langle v| + |u\rangle\langle v| + |v\rangle\langle u| \right] , \\ \hat{Y}_{uv} &= \frac{1}{2} \left[|u\rangle\langle u| + |v\rangle\langle v| - i|u\rangle\langle v| + i|v\rangle\langle u| \right] .\end{aligned}\tag{S.40}$$

This choice is also used in Ref. 6 for PFIs obtained from the Ehrenfest method.

In practice, one starts with \hat{X}_{uv} and \hat{Y}_{uv} instead of $|u\rangle\langle v|$ and $|v\rangle\langle u|$ as initial electronic states, to obtain the TT-TFD calculations of

$$\langle \psi_{\theta, jj\hat{X}_{uv}}(t) | \psi_{\theta, jk\hat{X}_{uv}}(t) \rangle , \quad \langle \psi_{\theta, jj\hat{Y}_{uv}}(t) | \psi_{\theta, jk\hat{Y}_{uv}}(t) \rangle .\tag{S.41}$$

The corresponding results for $|u\rangle\langle v|$ and $|v\rangle\langle u|$ as the initial electronic states can then be expressed as linear combinations of the results in Eq. (S.41). More specifically,

$$\begin{aligned}\mathcal{U}_{jk,uv}(t) &= \langle \psi_{\theta, jj\hat{X}_{uv}}(t) | \psi_{\theta, jk\hat{X}_{uv}}(t) \rangle + i \langle \psi_{\theta, jj\hat{Y}_{uv}}(t) | \psi_{\theta, jk\hat{Y}_{uv}}(t) \rangle \\ &\quad - \frac{1}{2}(1+i) \left[\langle \psi_{\theta, jjuu}(t) | \psi_{\theta, jkku}(t) \rangle - \langle \psi_{\theta, jjvv}(t) | \psi_{\theta, jkvv}(t) \rangle \right],\end{aligned}\tag{S.42}$$

$$\begin{aligned}\mathcal{U}_{jk,vu}(t) &= \langle \psi_{\theta, jj\hat{X}_{uv}}(t) | \psi_{\theta, jk\hat{X}_{uv}}(t) \rangle - i \langle \psi_{\theta, jj\hat{Y}_{uv}}(t) | \psi_{\theta, jk\hat{Y}_{uv}}(t) \rangle \\ &\quad - \frac{1}{2}(1-i) \left[\langle \psi_{\theta, jjuu}(t) | \psi_{\theta, jkku}(t) \rangle - \langle \psi_{\theta, jjvv}(t) | \psi_{\theta, jkvv}(t) \rangle \right].\end{aligned}\tag{S.43}$$

S.V Graphs of the Projection-Free Inputs

Given in this section are the graphs of the imaginary part of $\mathcal{F}(\tau)$ and the real and imaginary parts of $\dot{\mathcal{F}}(\tau)$ for models 1, 2, 3, and 6. The real part of $\mathcal{F}(\tau)$ is not show because it is zero for all models for both TT-TFD and LSC.

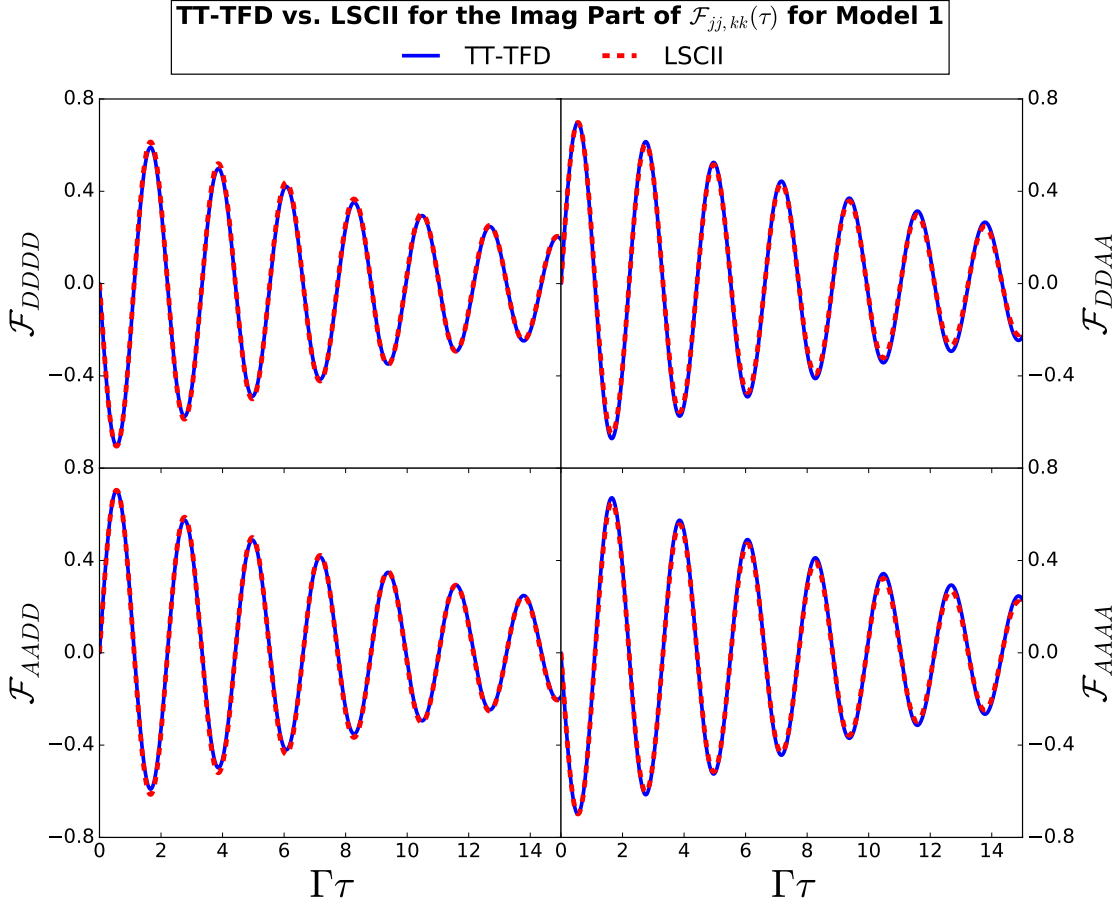


Figure S1: Imaginary parts of the $DDDD$, $DDAA$, $AADD$ and $AAAA$ matrix elements of $\mathcal{F}(\tau)$ for model 1, as obtained via TT-TFD (solid blue lines) and LSCII (dashed red lines).

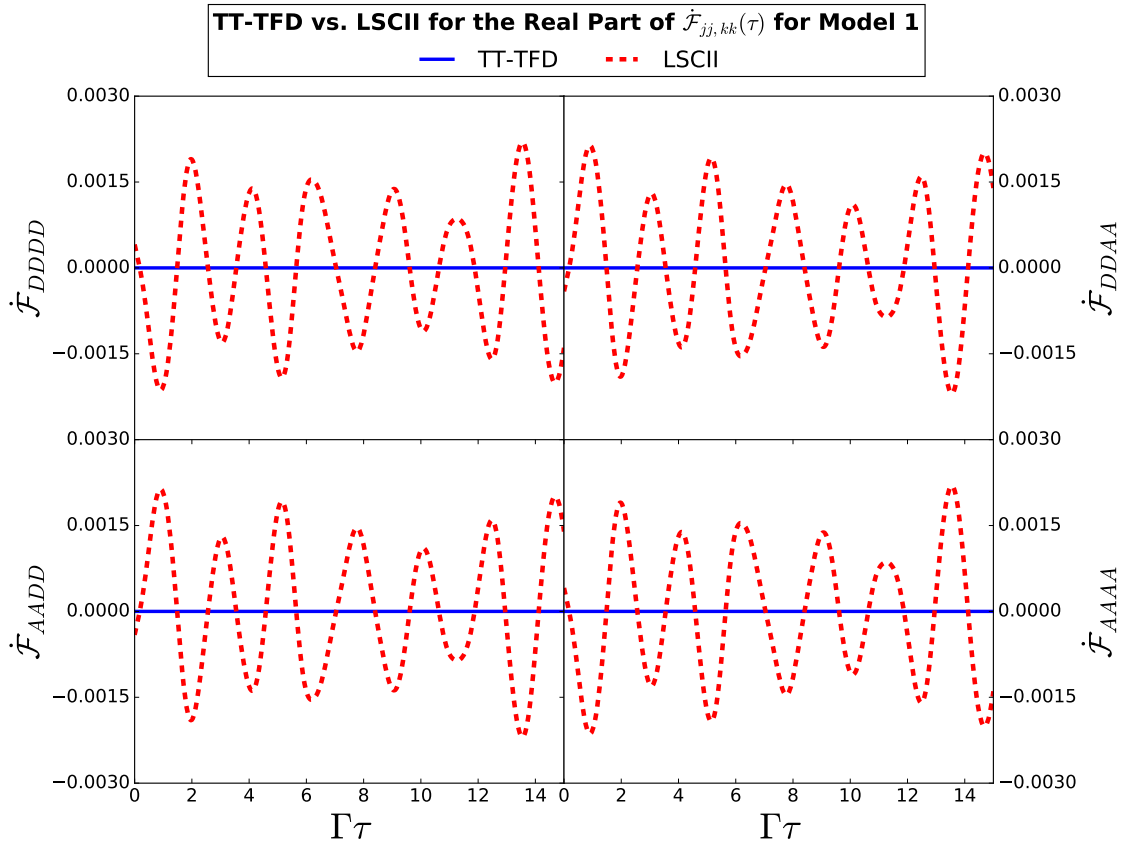


Figure S2: Real parts of the $DDDD$, $DDAA$, $AADD$ and $AAAA$ matrix elements of $\dot{\mathcal{F}}(\tau)$ for model 1, as obtained via TT-TFD (solid blue lines) and LSCII (dashed red lines).

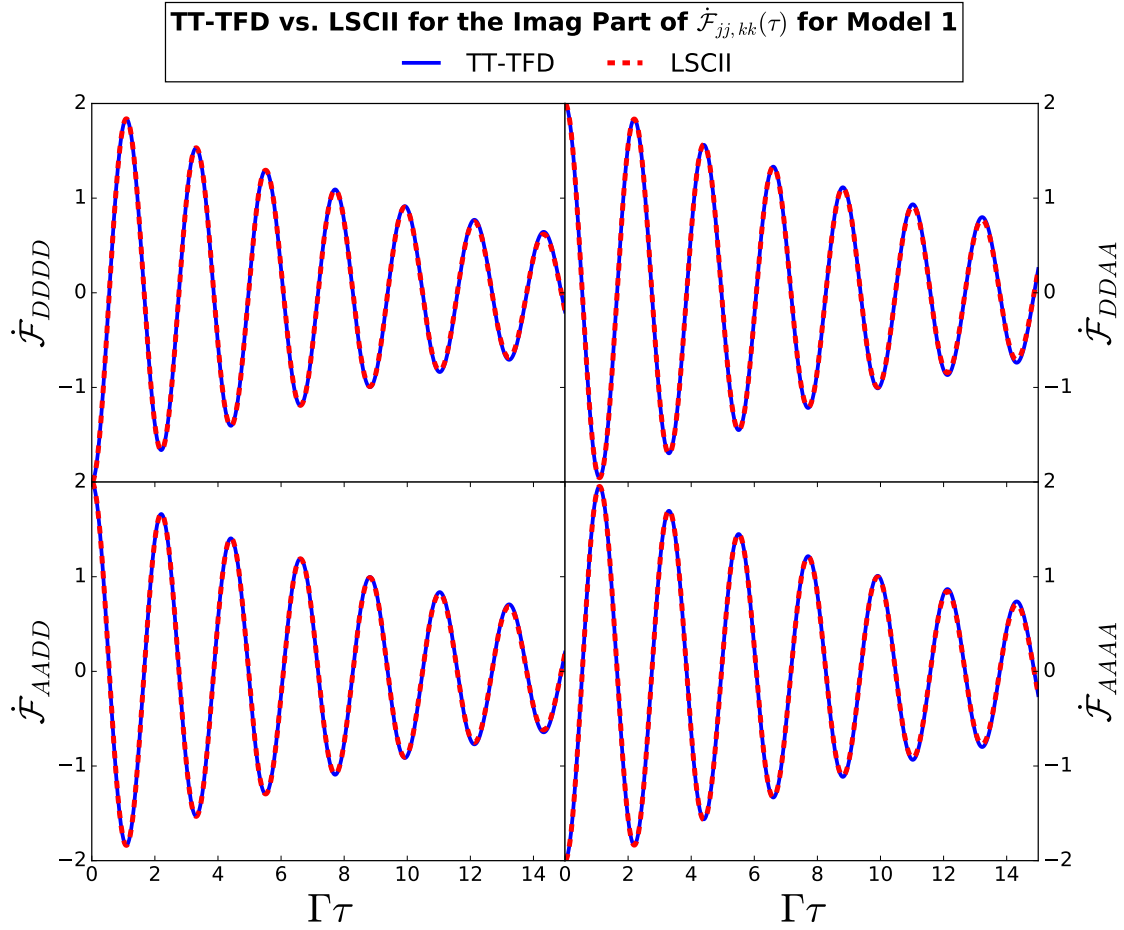


Figure S3: Imaginary parts of the $DDDD$, $DDAA$, $AADD$ and $AAAA$ matrix elements of $\dot{\mathcal{F}}(\tau)$ for model 1, as obtained via TT-TFD (solid blue lines) and LSCII (dashed red lines).

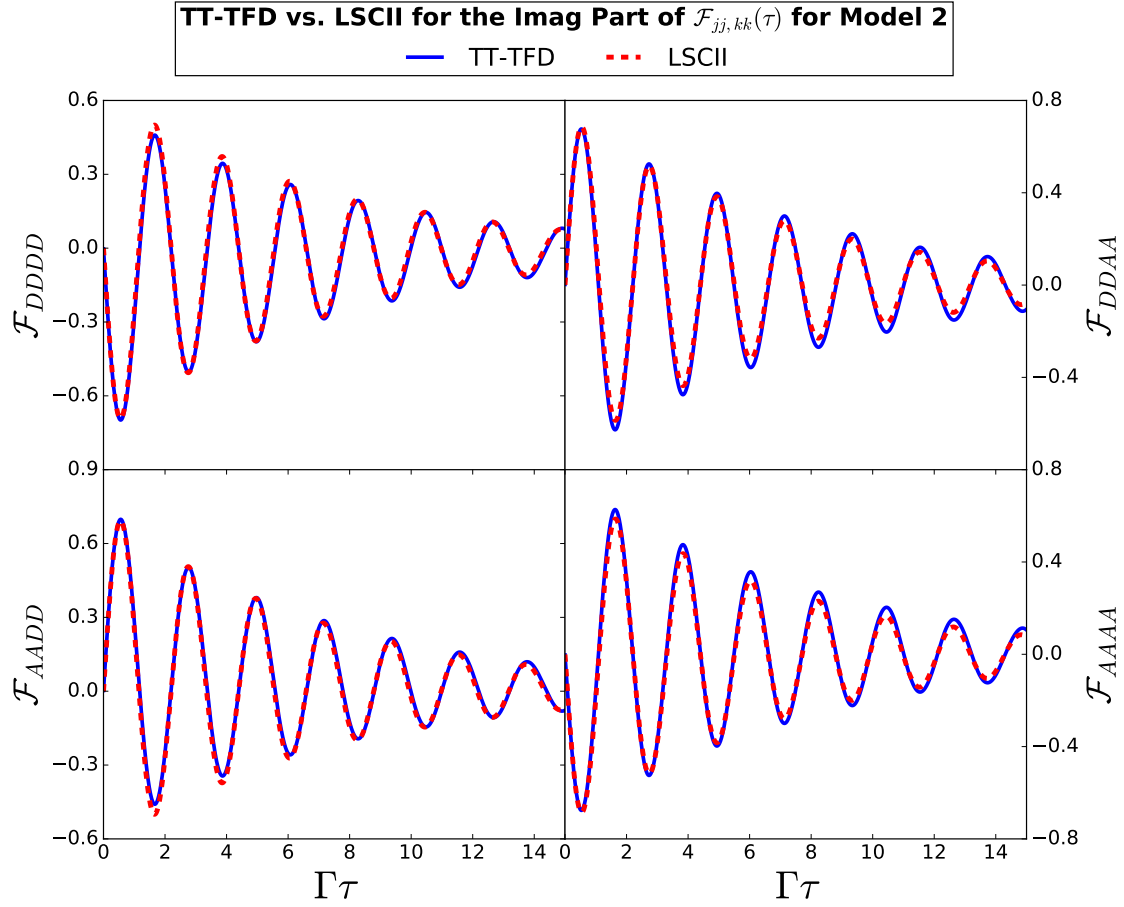


Figure S4: Imaginary parts of the $DDDD$, $DDAA$, $AADD$ and $AAAA$ matrix elements of $\mathcal{F}(\tau)$ for model 2, as obtained via TT-TFD (solid blue lines) and LSCII (dashed red lines).

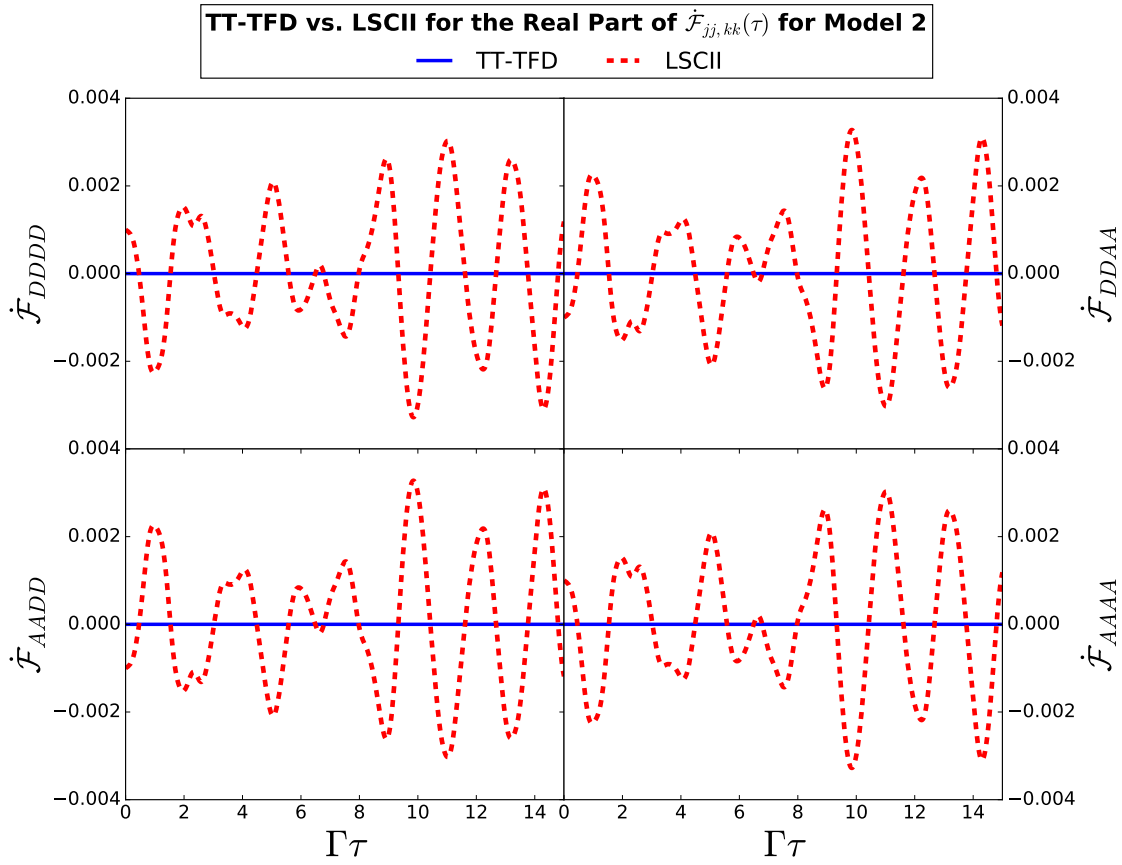


Figure S5: Real parts of the $DDDD$, $DDAA$, $AADD$ and $AAAA$ matrix elements of $\dot{\mathcal{F}}(\tau)$ for model 2, as obtained via TT-TFD (solid blue lines) and LSCII (dashed red lines).

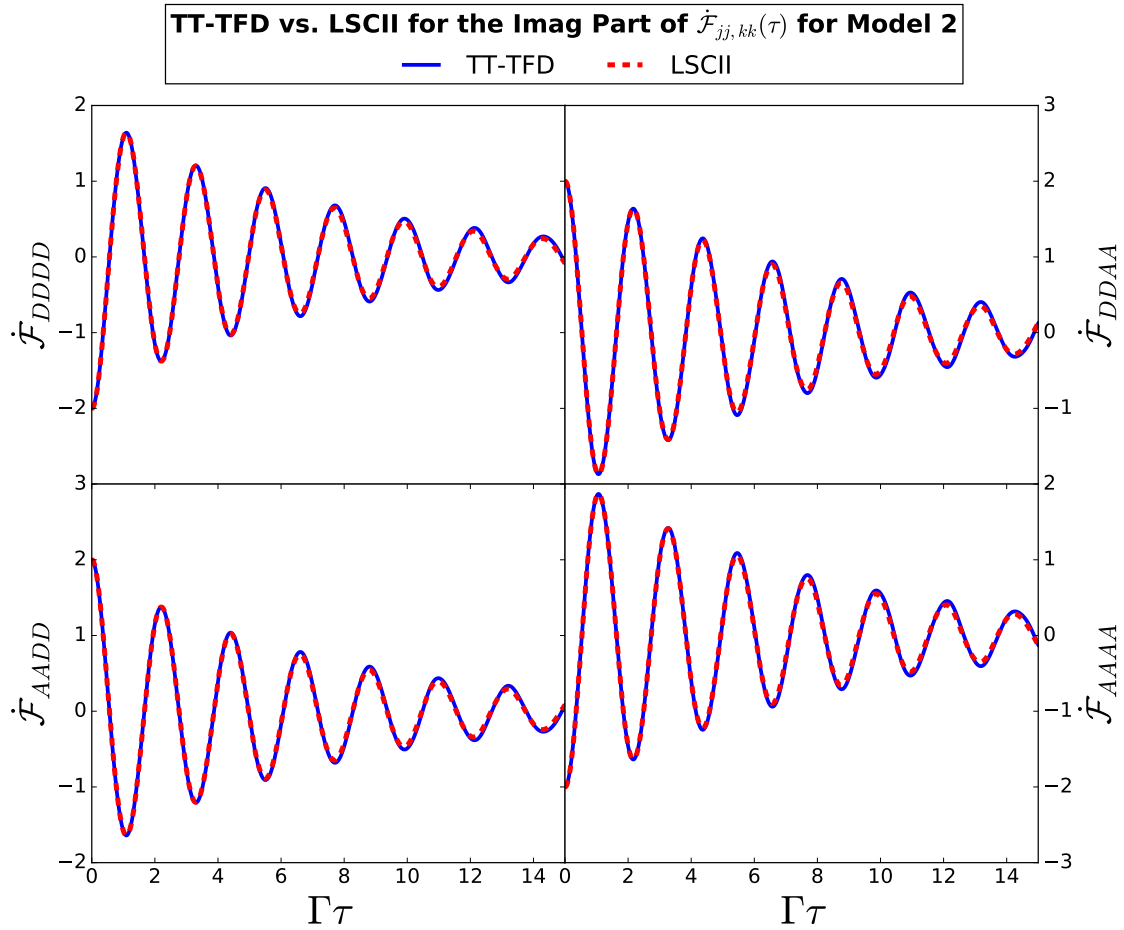


Figure S6: Imaginary parts of the $DDDD$, $DDAA$, $AADD$ and $AAAA$ matrix elements of $\dot{\mathcal{F}}(\tau)$ for model 2, as obtained via TT-TFD (solid blue lines) and LSCII (dashed red lines).

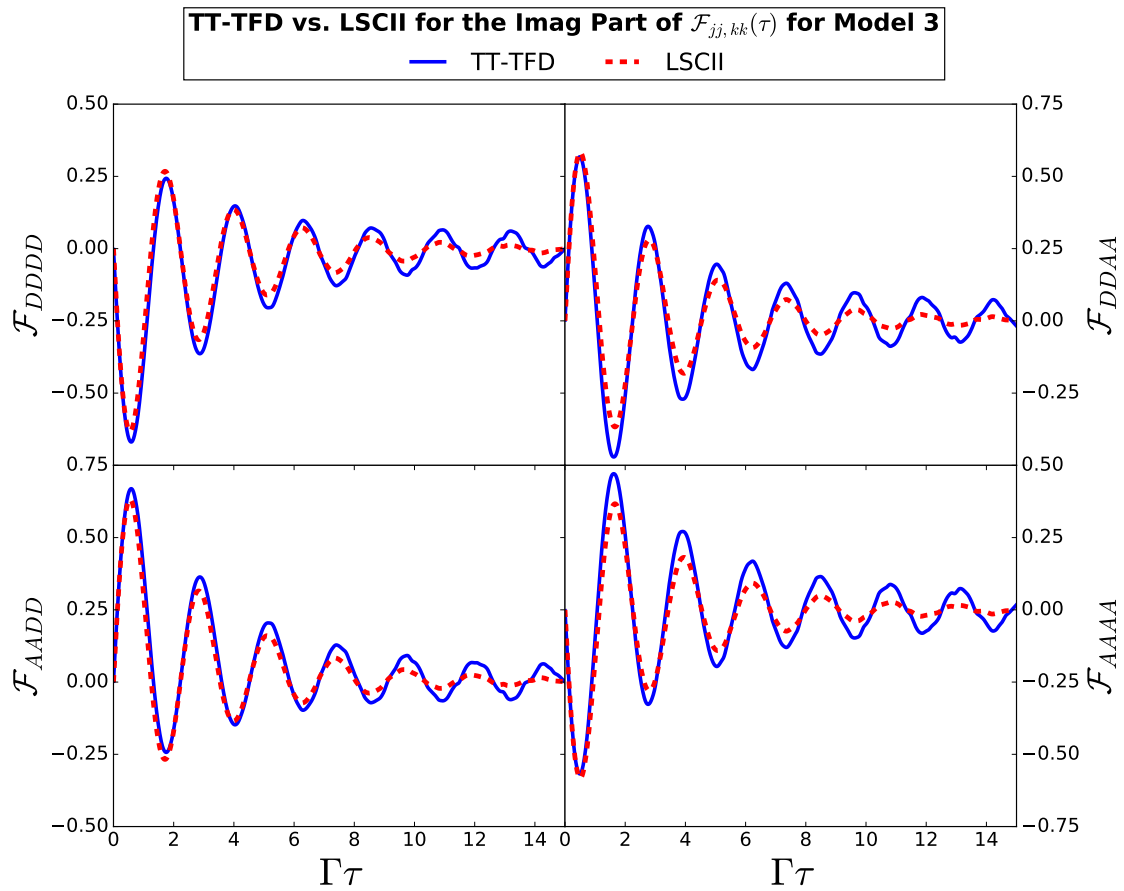


Figure S7: Imaginary parts of the $DDDD$, $DDAA$, $AADD$ and $AAAA$ matrix elements of $\mathcal{F}(\tau)$ for model 3, as obtained via TT-TFD (solid blue lines) and LSCII (dashed red lines).

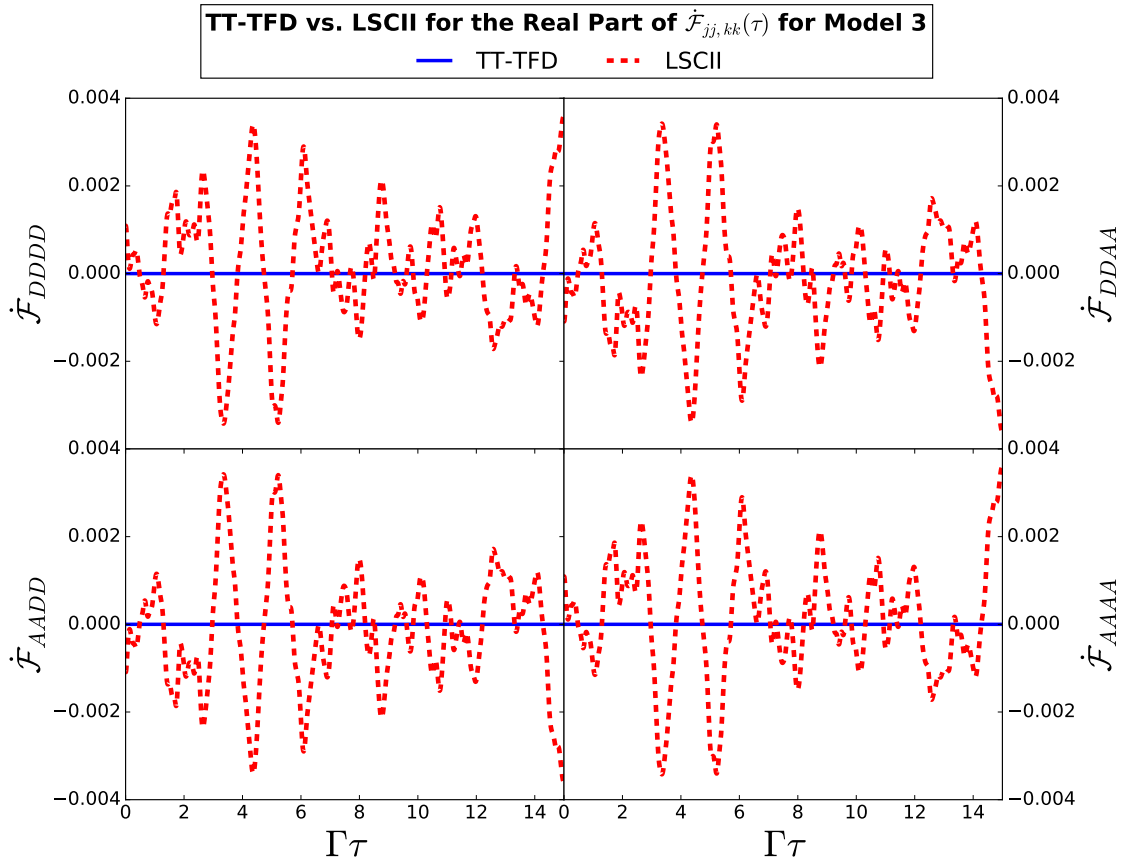


Figure S8: Real parts of the $DDDD$, $DDAA$, $AADD$ and $AAAA$ matrix elements of $\dot{\mathcal{F}}(\tau)$ for model 3, as obtained via TT-TFD (solid blue lines) and LSCII (dashed red lines).

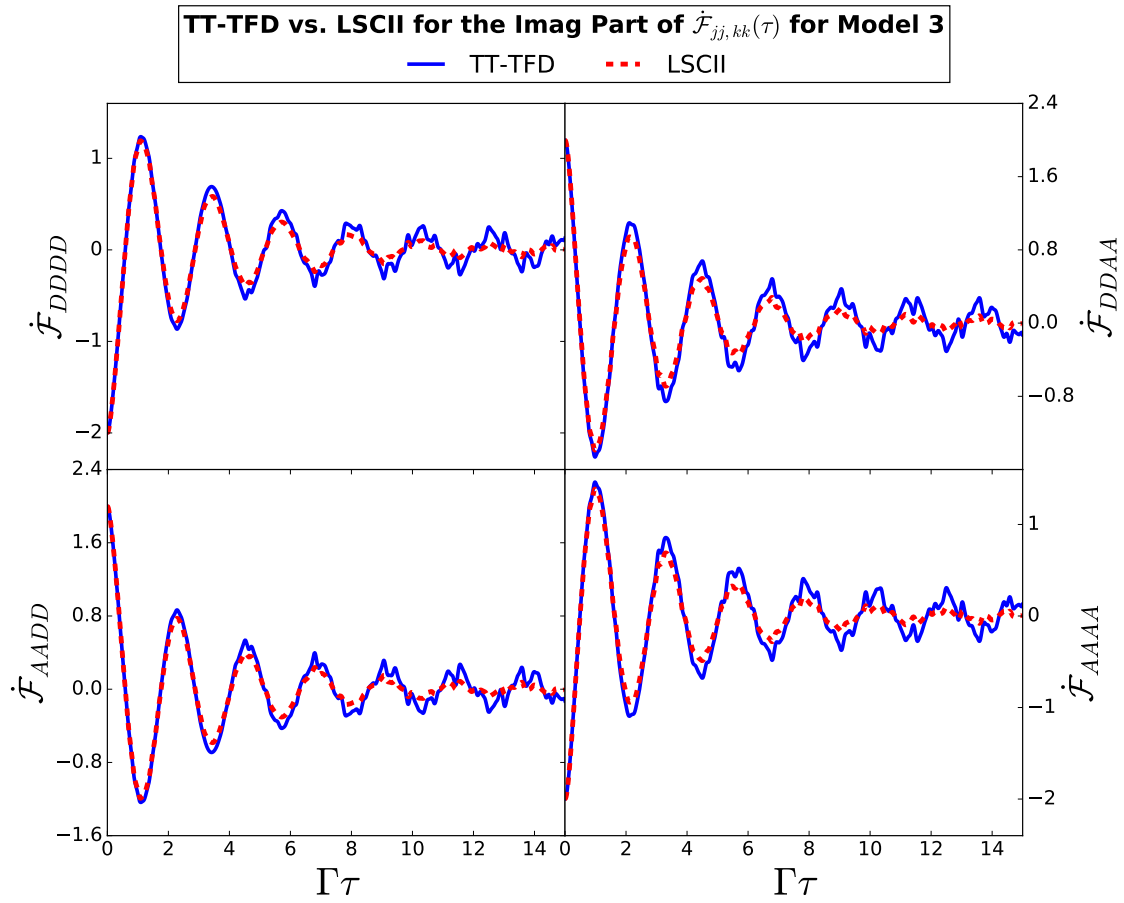


Figure S9: Imaginary parts of the $DDDD$, $DDAA$, $AADD$ and $AAAA$ matrix elements of $\dot{\mathcal{F}}(\tau)$ for model 3, as obtained via TT-TFD (solid blue lines) and LSCII (dashed red lines).

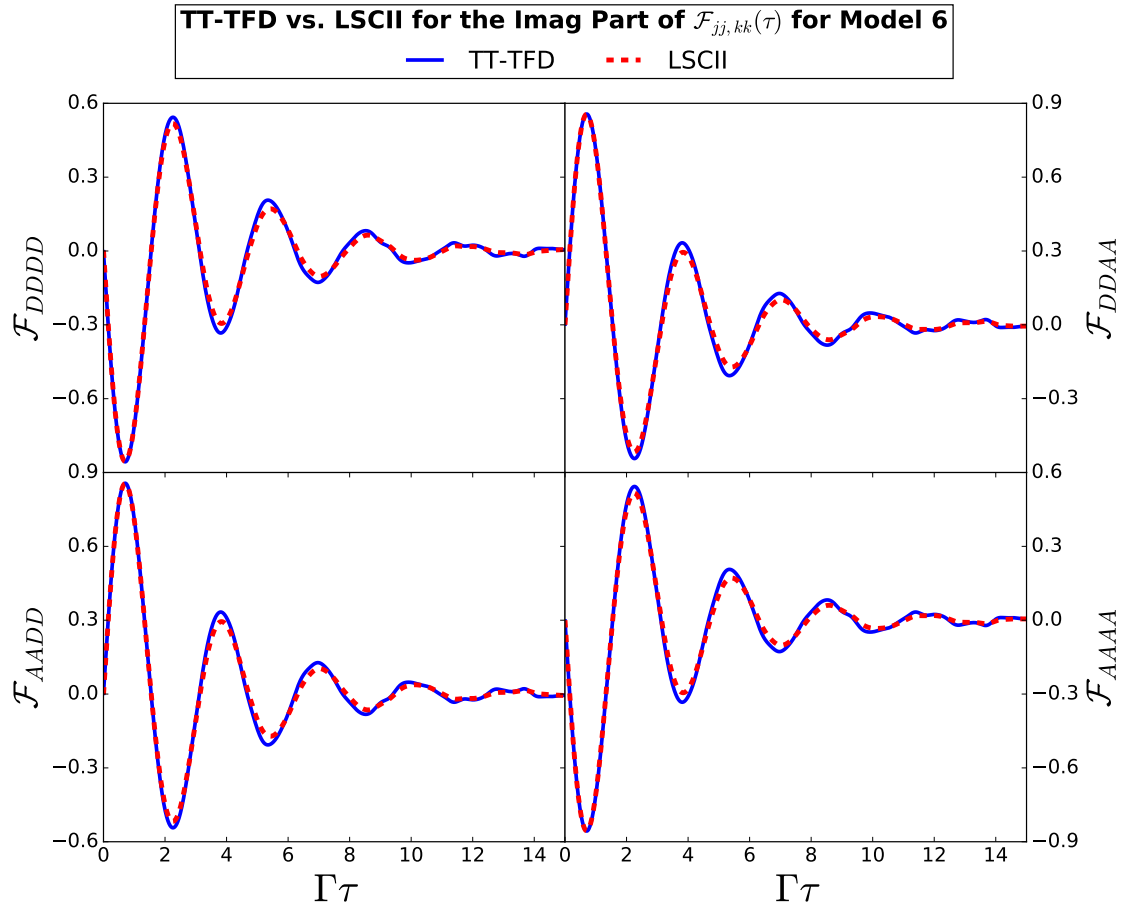


Figure S10: Imaginary parts of the $DDDD$, $DDAA$, $AADD$ and $AAAA$ matrix elements of $\mathcal{F}(\tau)$ for model 6, as obtained via TT-TFD (solid blue lines) and LSCII (dashed red lines).

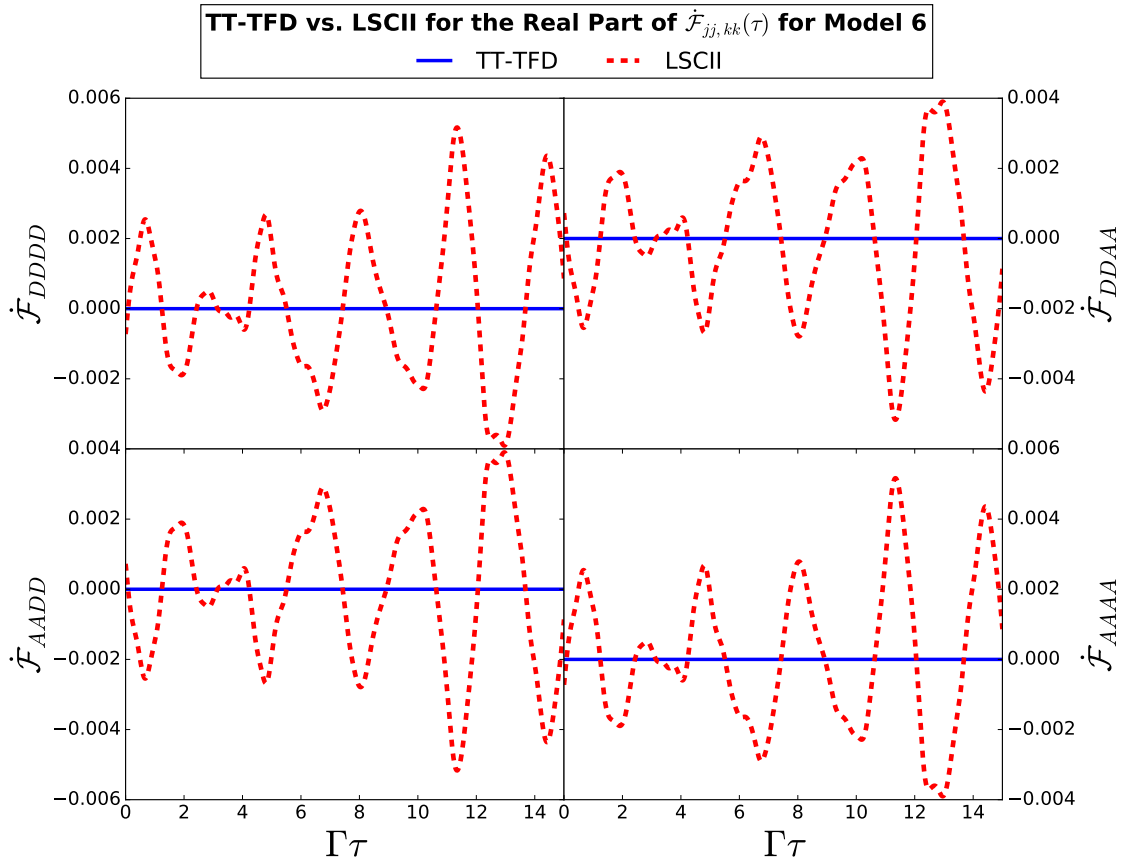


Figure S11: Real parts of the $DDDD$, $DDAA$, $AADD$ and $AAAA$ matrix elements of $\dot{\mathcal{F}}(\tau)$ for model 6, as obtained via TT-TFD (solid blue lines) and LSCII (dashed red lines).

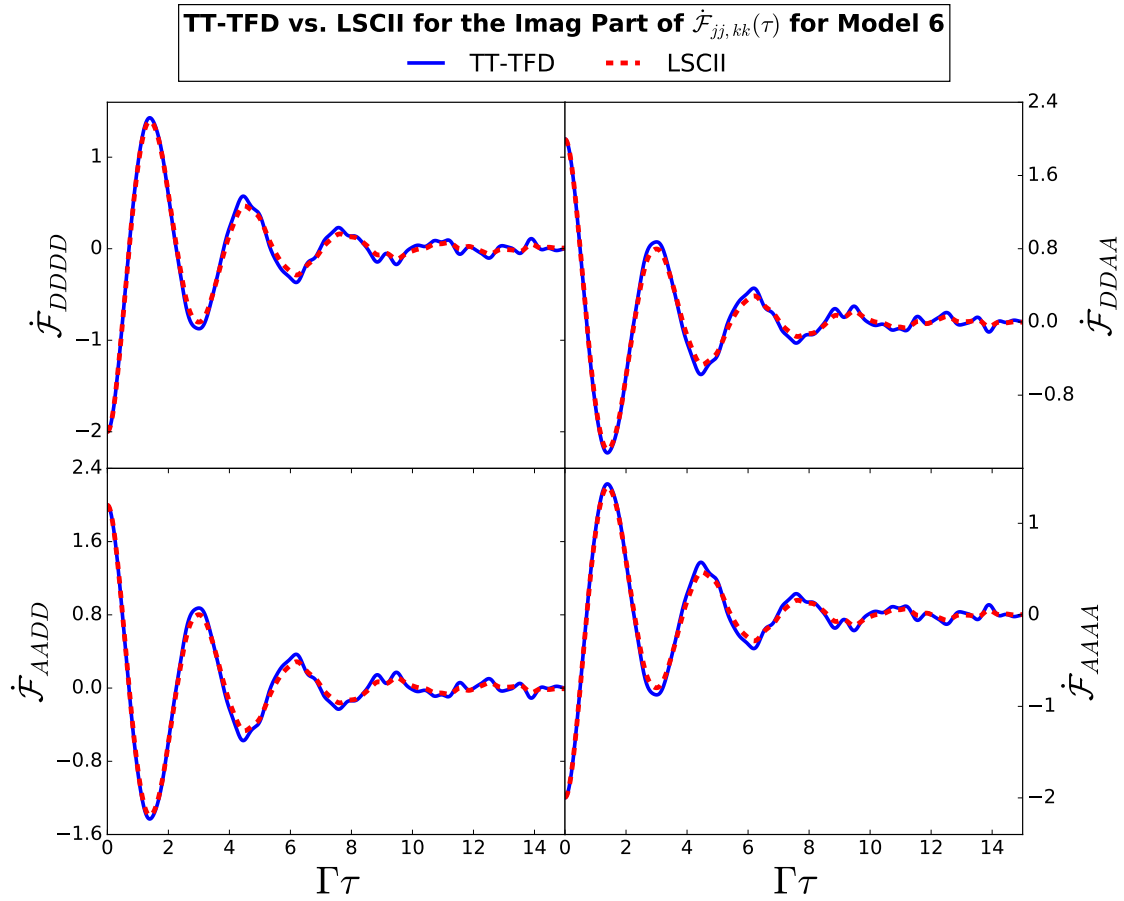


Figure S12: Imaginary parts of the $DDDD$, $DDAA$, $AADD$ and $AAAA$ matrix elements of $\dot{\mathcal{F}}(\tau)$ for model 6, as obtained via TT-TFD (solid blue lines) and LSCII (dashed red lines).

S.VI Graphs of the Memory Kernels

Given in this section are the graphs of the real and imaginary parts of the memory kernels for models 1, 2, 3, and 6.

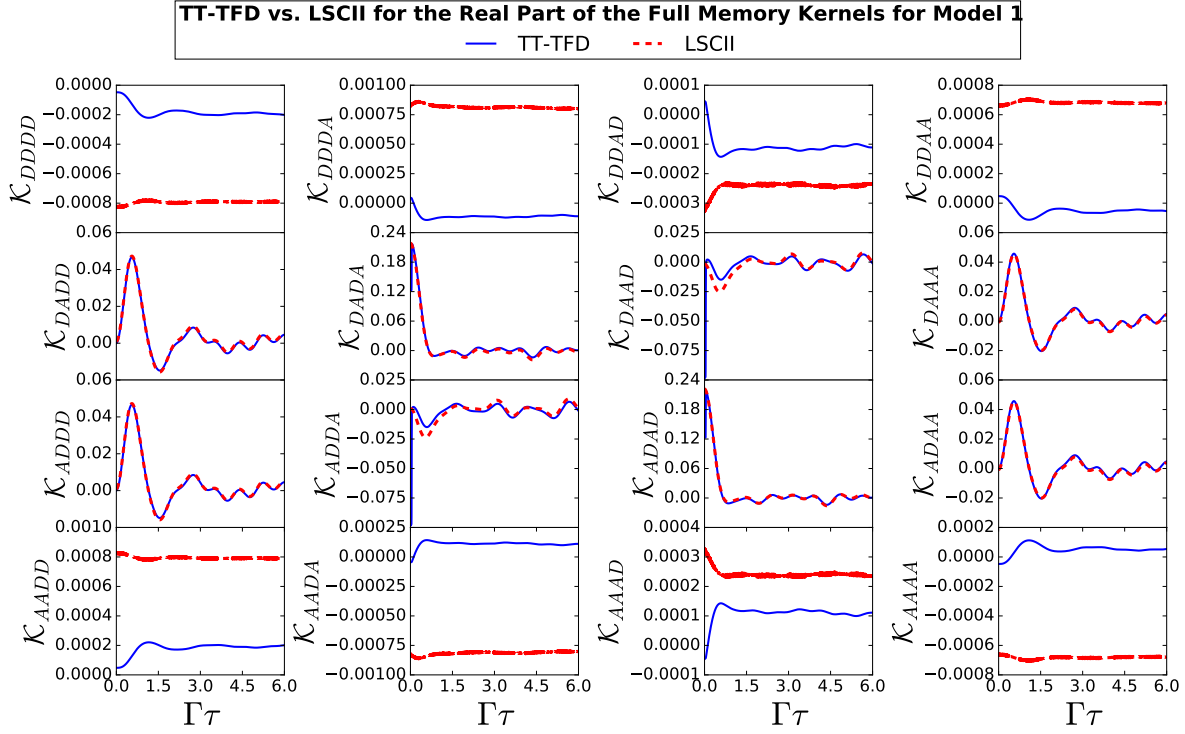


Figure S13: Real parts of the matrix elements of the memory kernel of the GQME for the full electronic density matrix $[\mathcal{K}^{\text{full}}(\tau)]$ for model 1 as obtained from TT-TFD-based PFIs (solid blue lines) and LSCII-based PFIs (dashed red lines).

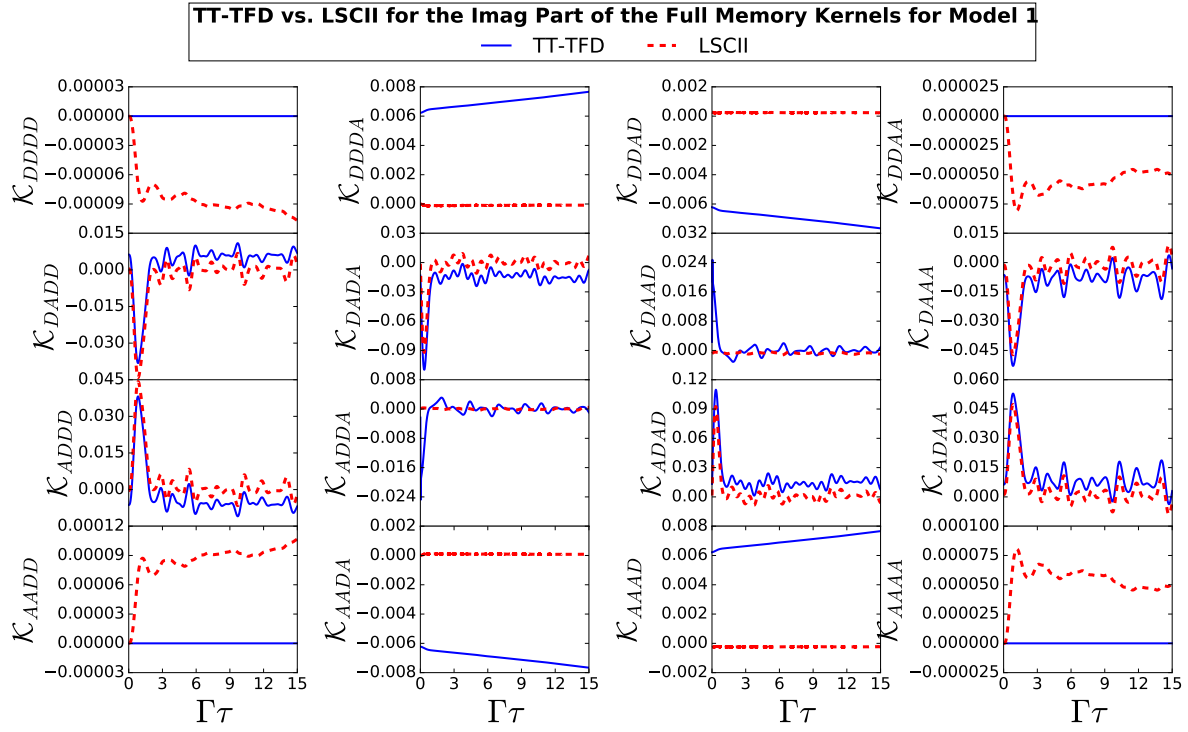


Figure S14: Imaginary parts of the matrix elements of the memory kernel of the GQME for the full electronic density matrix $[\mathcal{K}^{\text{full}}(\tau)]$ for model 1 as obtained from TT-TFD-based PFIs (solid blue lines) and LSCII-based PFIs (dashed red lines).

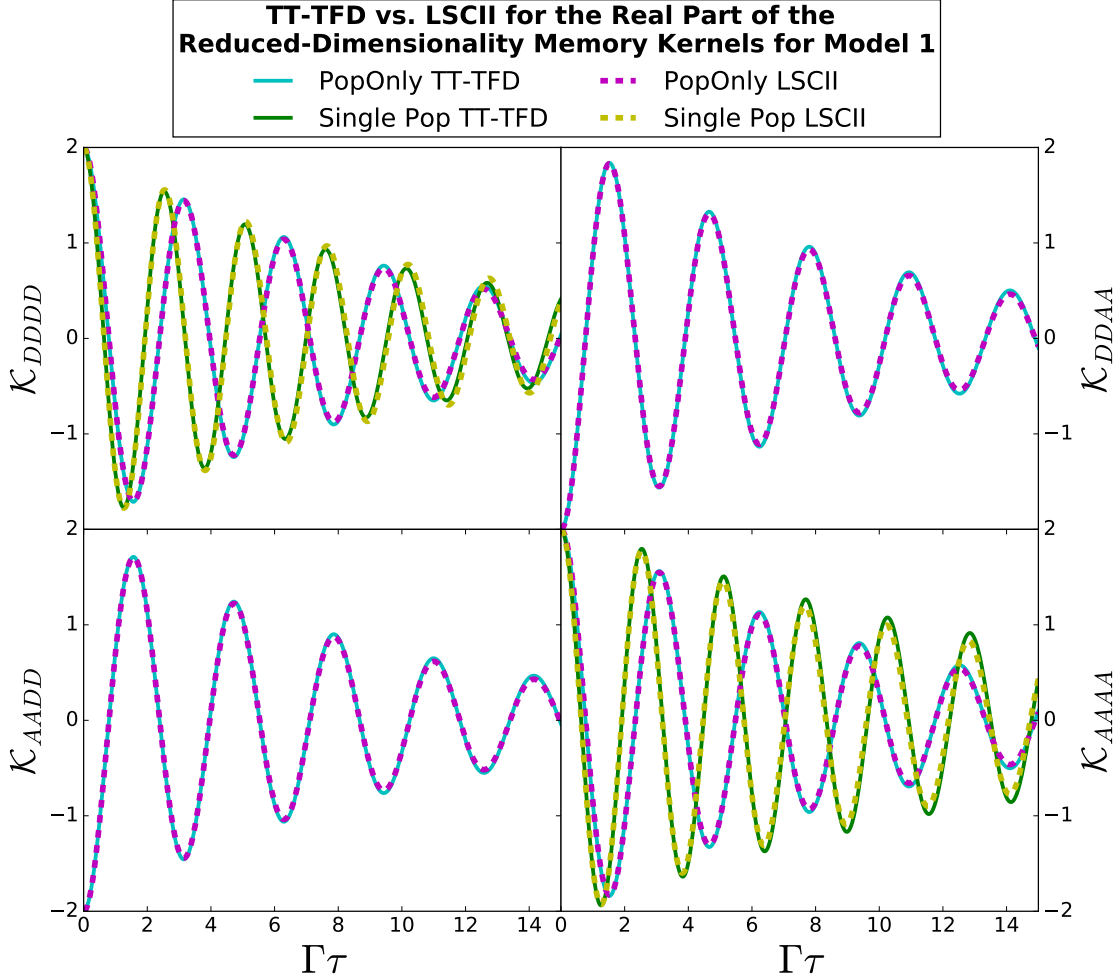


Figure S15: The real parts of the matrix elements of the memory kernels for the populations-only and single-population GQMEs for model 1 as obtained from TT-TFD-based PFIs and LSCII-based PFIs. Shown are the matrix elements of three different memory kernels: (1) The memory kernel of the populations-only GQME [$\mathcal{K}^{\text{pop}}(\tau)$], which has four elements ($DDDD$, $DDAA$, $AADD$, $AAAA$) and is depicted with solid cyan lines for the results from TT-TFD-based PFIs and dashed magenta lines for the results from LSCII-based PFIs; (2) and (3) The single-element memory kernels of the scalar single-population GQMEs [$\mathcal{K}_{DD,DD}^{\text{donor}}(\tau)$ and $\mathcal{K}_{AA,AA}^{\text{acceptor}}(\tau)$], which are depicted in the $DDDD$ and $AAAA$ panels, respectively, with solid green lines for the results from TT-TFD-based PFIs and dashed yellow lines for the results from LSCII-based PFIs.

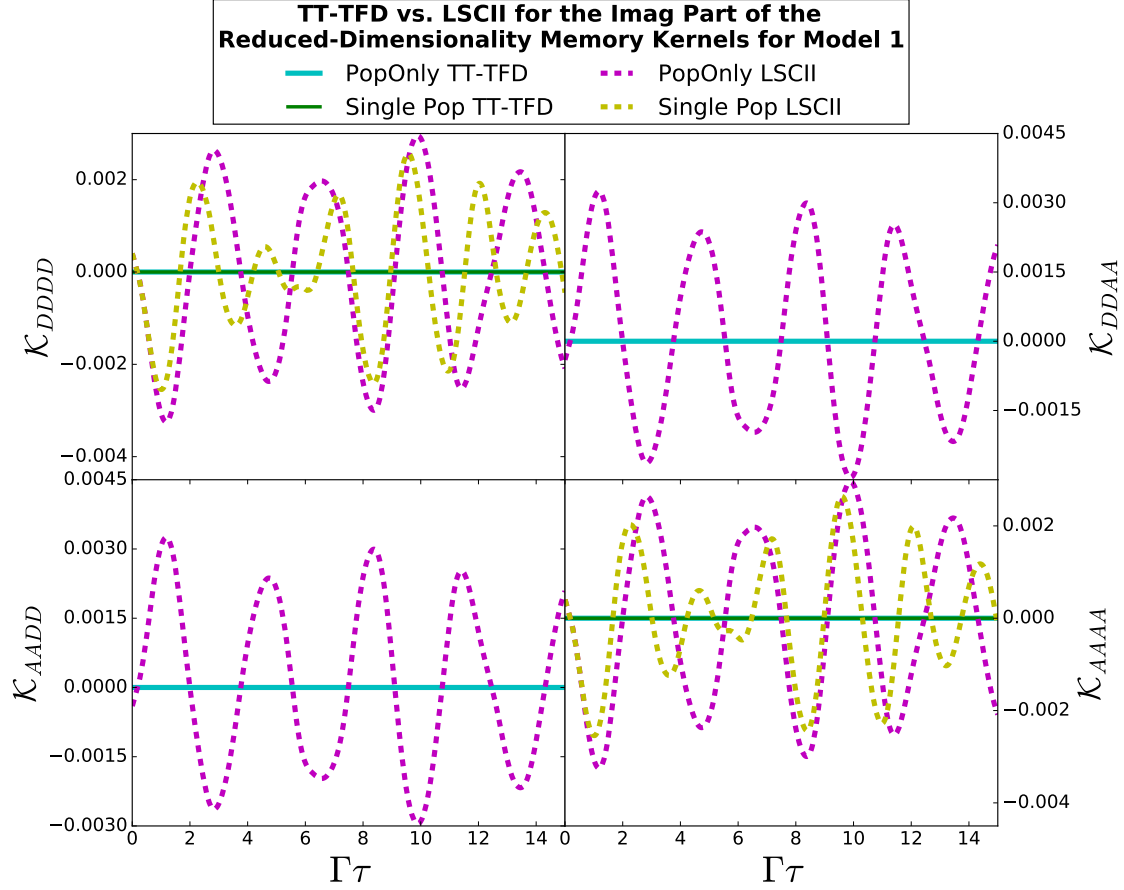


Figure S16: The imaginary parts of the matrix elements of the memory kernels for the populations-only and single-population GQMEs for model 1 as obtained from TT-TFD-based PFIs and LSCII-based PFIs. Shown are the matrix elements of three different memory kernels: (1) The memory kernel of the populations-only GQME [$\mathcal{K}^{\text{pop}}(\tau)$], which has four elements ($DDDD$, $DDAA$, $AADD$, $AAAA$) and is depicted with solid cyan lines for the results from TT-TFD-based PFIs and dashed magenta lines for the results from LSCII-based PFIs; (2) and (3) The single-element memory kernels of the scalar single-population GQMEs [$\mathcal{K}_{DD,DD}^{\text{donor}}(\tau)$ and $\mathcal{K}_{AA,AA}^{\text{acceptor}}(\tau)$], which are depicted in the $DDDD$ and $AAAA$ panels, respectively, with solid green lines for the results from TT-TFD-based PFIs and dashed yellow lines for the results from LSCII-based PFIs.

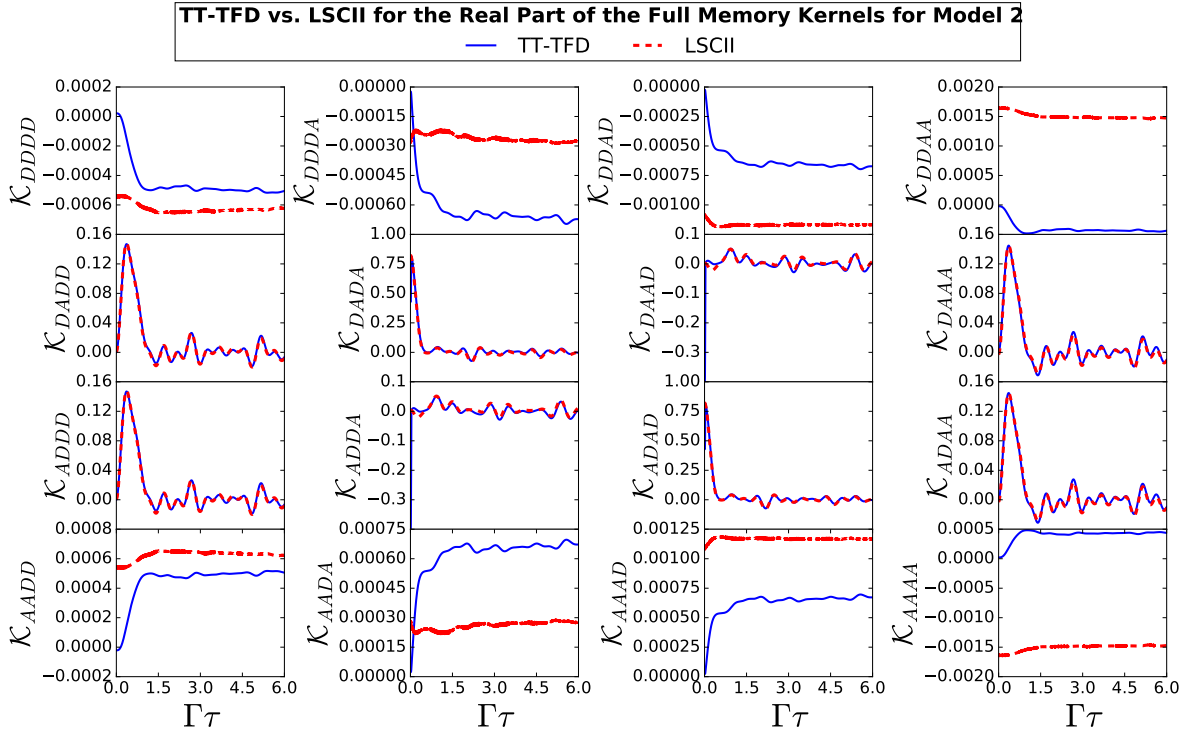


Figure S17: Real parts of the matrix elements of the memory kernel of the GQME for the full electronic density matrix $[\mathcal{K}^{\text{full}}(\tau)]$ for model 2 as obtained from TT-TFD-based PFIs (solid blue lines) and LSCII-based PFIs (dashed red lines).

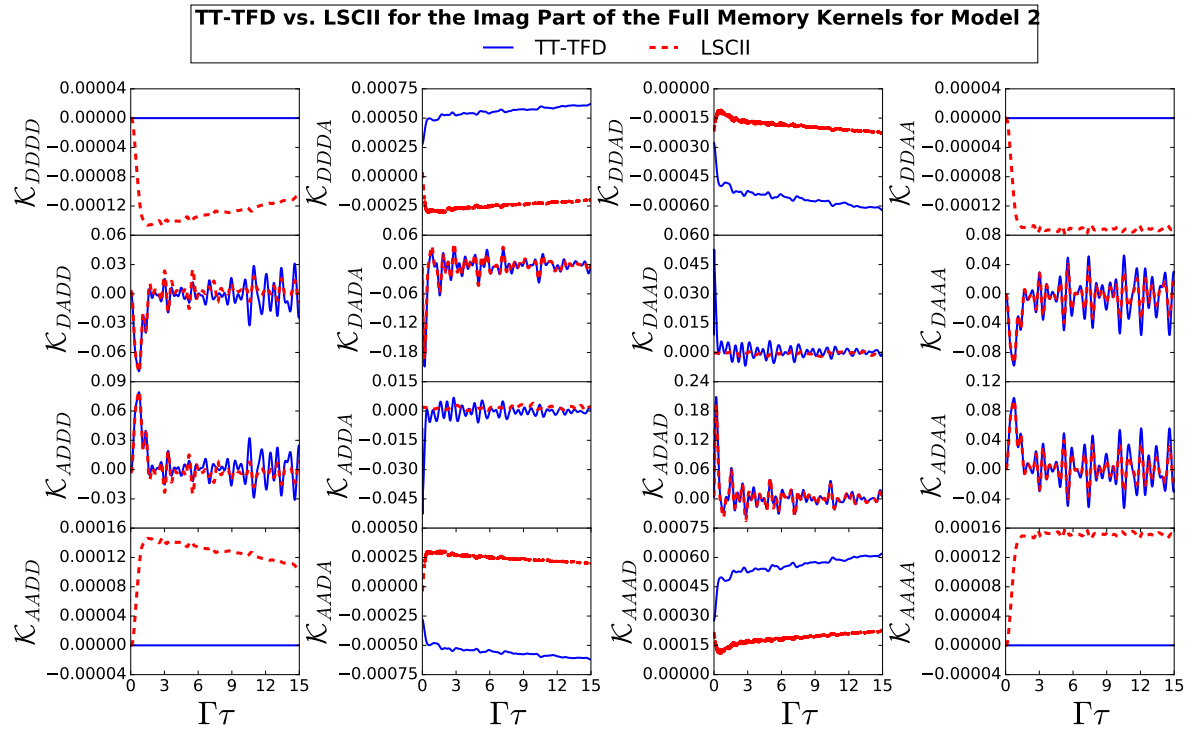


Figure S18: Imaginary parts of the matrix elements of the memory kernel of the GQME for the full electronic density matrix $[\mathcal{K}^{\text{full}}(\tau)]$ for model 2 as obtained from TT-TFD-based PFIs (solid blue lines) and LSCII-based PFIs (dashed red lines).

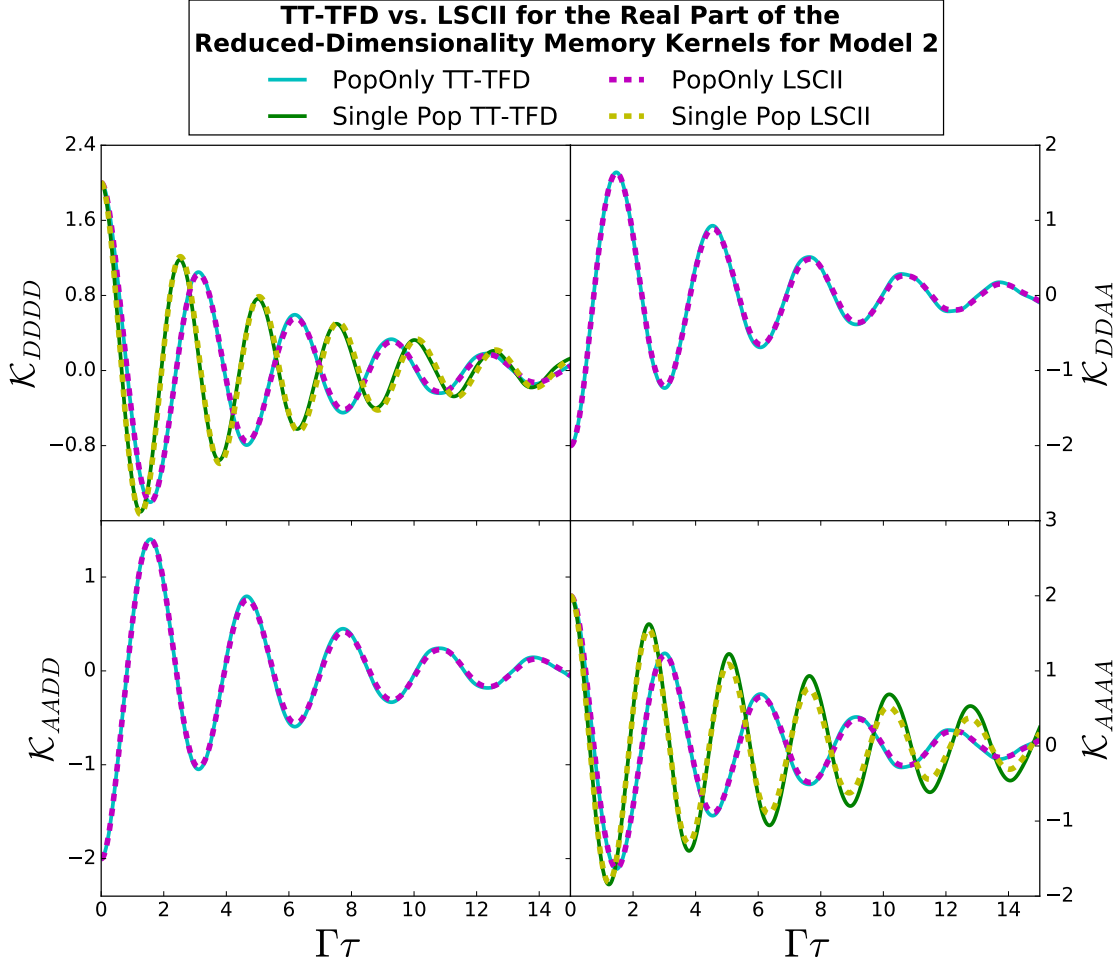


Figure S19: The real parts of the matrix elements of the memory kernels for the populations-only and single-population GQMEs for model 2 as obtained from TT-TFD-based PFIs and LSCII-based PFIs. Shown are the matrix elements of three different memory kernels: (1) The memory kernel of the populations-only GQME [$\mathcal{K}^{\text{pop}}(\tau)$], which has four elements ($DDDD, DDAA, AADD, AAAA$) and is depicted with solid cyan lines for the results from TT-TFD-based PFIs and dashed magenta lines for the results from LSCII-based PFIs; (2) and (3) The single-element memory kernels of the scalar single-population GQMEs [$\mathcal{K}_{DD,DD}^{\text{donor}}(\tau)$ and $\mathcal{K}_{AA,AA}^{\text{acceptor}}(\tau)$], which are depicted in the $DDDD$ and $AAAA$ panels, respectively, with solid green lines for the results from TT-TFD-based PFIs and dashed yellow lines for the results from LSCII-based PFIs.

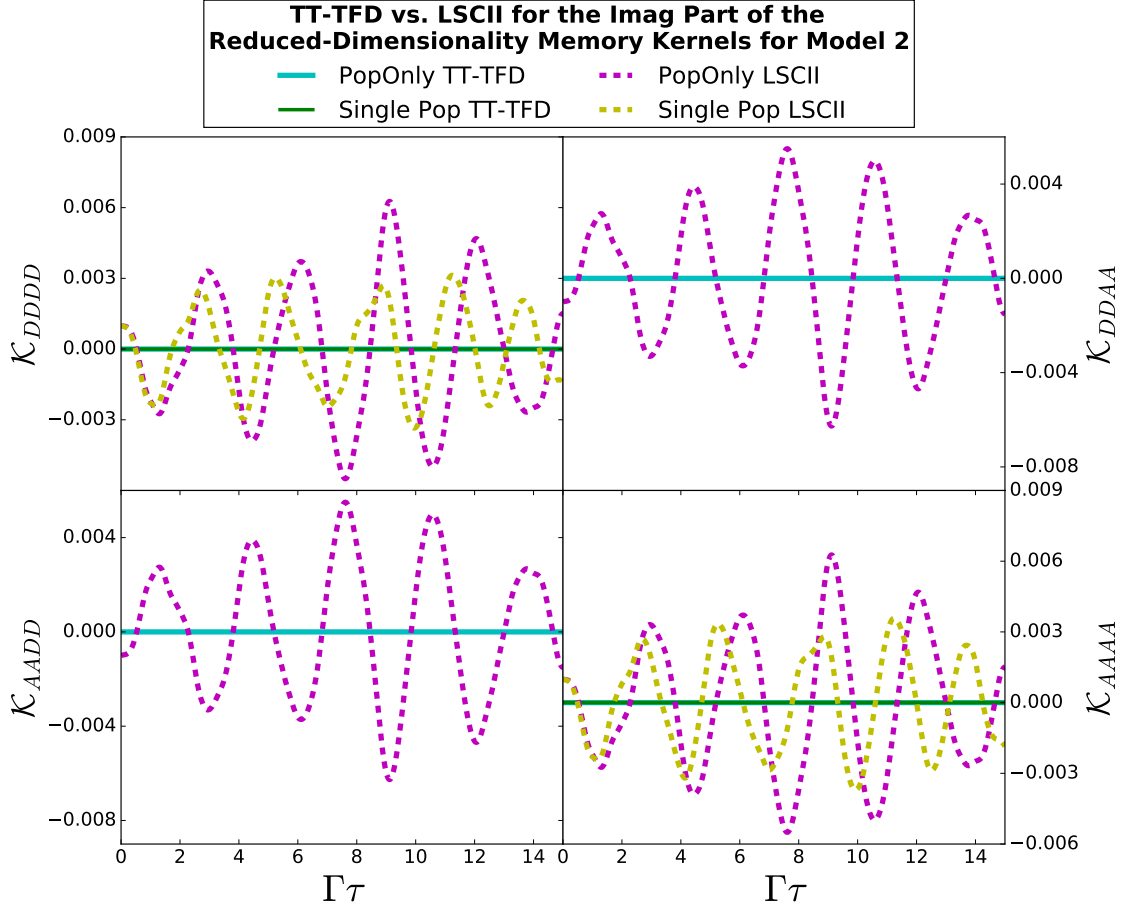


Figure S20: The imaginary parts of the matrix elements of the memory kernels for the populations-only and single-population GQMEs for model 2 as obtained from TT-TFD-based PFIs and LSCII-based PFIs. Shown are the matrix elements of three different memory kernels: (1) The memory kernel of the populations-only GQME [$\mathcal{K}^{\text{pop}}(\tau)$], which has four elements ($DDDD, DDAA, AADD, AAAA$) and is depicted with solid cyan lines for the results from TT-TFD-based PFIs and dashed magenta lines for the results from LSCII-based PFIs; (2) and (3) The single-element memory kernels of the scalar single-population GQMEs [$\mathcal{K}_{DD,DD}^{\text{donor}}(\tau)$ and $\mathcal{K}_{AA,AA}^{\text{acceptor}}(\tau)$], which are depicted in the $DDDD$ and $AAAA$ panels, respectively, with solid green lines for the results from TT-TFD-based PFIs and dashed yellow lines for the results from LSCII-based PFIs.

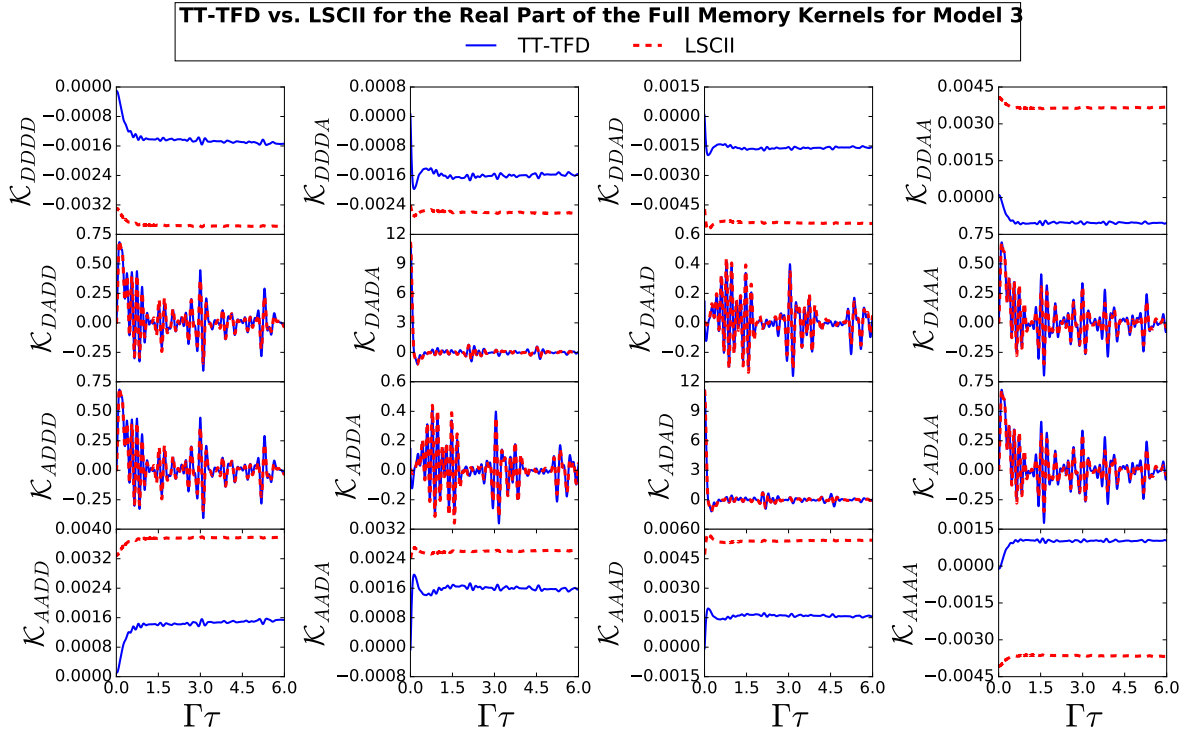


Figure S21: Real parts of the matrix elements of the memory kernel of the GQME for the full electronic density matrix $[\mathcal{K}^{\text{full}}(\tau)]$ for model 3 as obtained from TT-TFD-based PFIs (solid blue lines) and LSCII-based PFIs (dashed red lines).

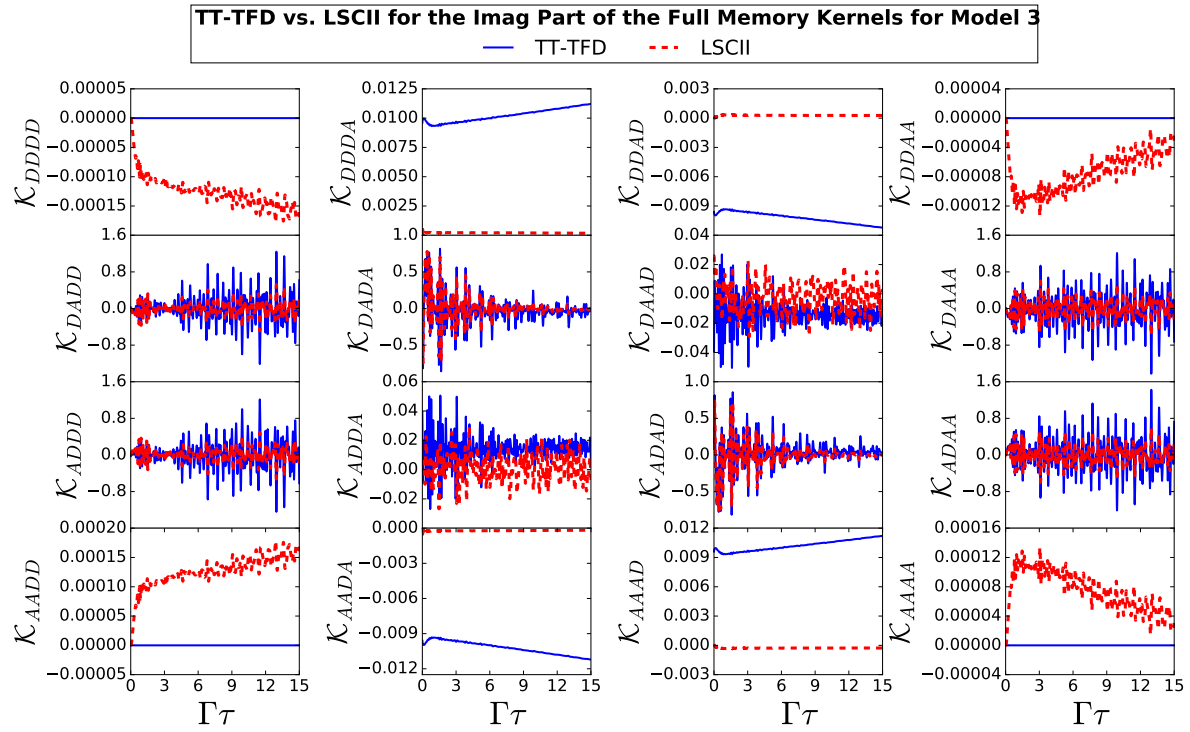


Figure S22: Imaginary parts of the matrix elements of the memory kernel of the GQME for the full electronic density matrix $[\mathcal{K}^{\text{full}}(\tau)]$ for model 3 as obtained from TT-TFD-based PFIs (solid blue lines) and LSCII-based PFIs (dashed red lines).

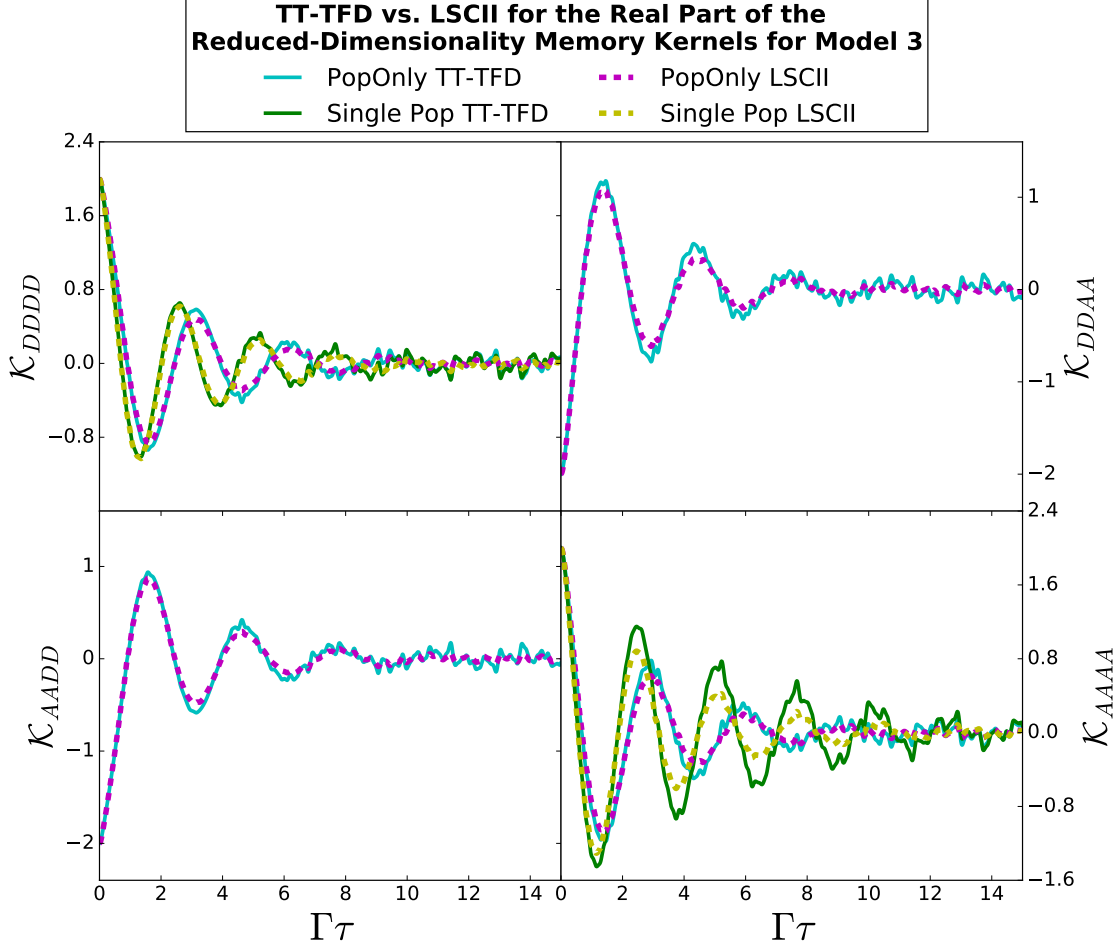


Figure S23: The real parts of the matrix elements of the memory kernels for the populations-only and single-population GQMEs for model 3 as obtained from TT-TFD-based PFIs and LSCII-based PFIs. Shown are the matrix elements of three different memory kernels: (1) The memory kernel of the populations-only GQME [$\mathcal{K}^{\text{pop}}(\tau)$], which has four elements ($DDDD, DDAA, AADD, AAAA$) and is depicted with solid cyan lines for the results from TT-TFD-based PFIs and dashed magenta lines for the results from LSCII-based PFIs; (2) and (3) The single-element memory kernels of the scalar single-population GQMEs [$\mathcal{K}_{DD,DD}^{\text{donor}}(\tau)$ and $\mathcal{K}_{AA,AA}^{\text{acceptor}}(\tau)$], which are depicted in the $DDDD$ and $AAAA$ panels, respectively, with solid green lines for the results from TT-TFD-based PFIs and dashed yellow lines for the results from LSCII-based PFIs.

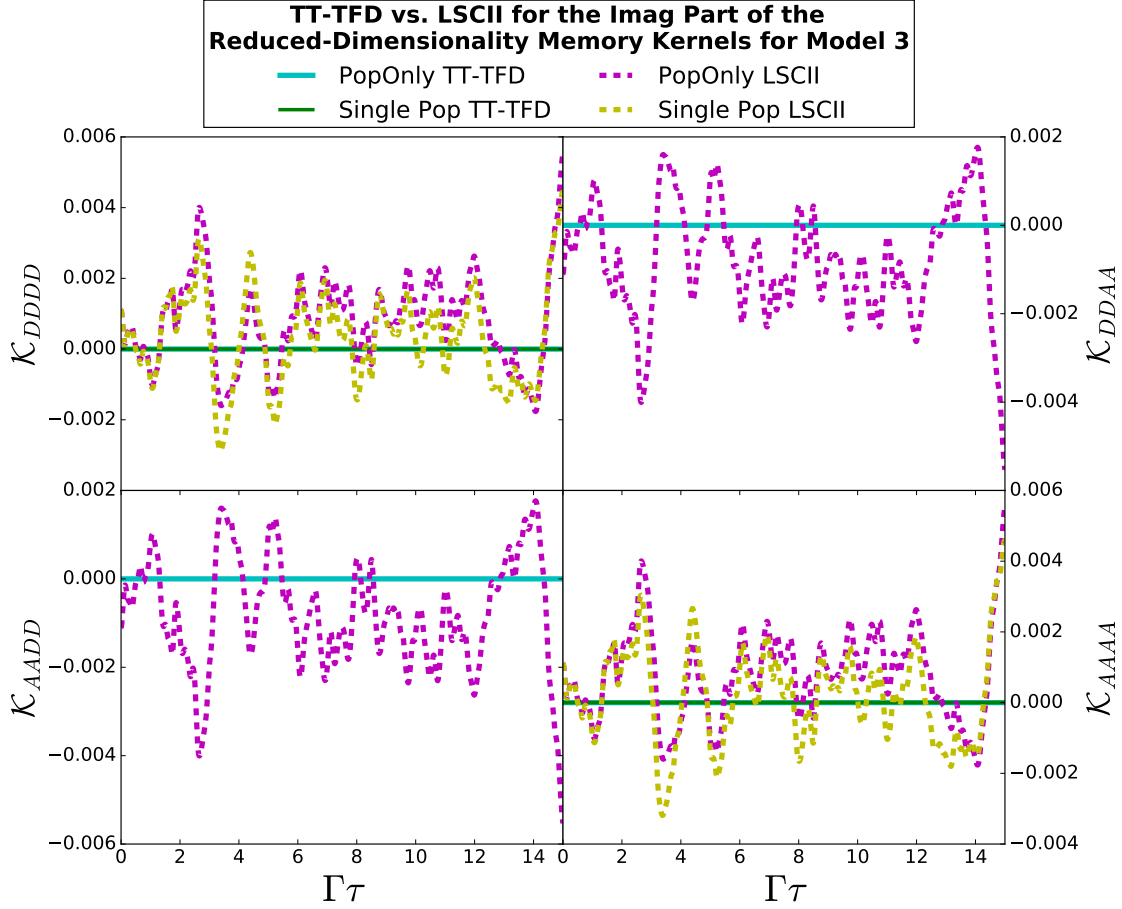


Figure S24: The imaginary parts of the matrix elements of the memory kernels for the populations-only and single-population GQMEs for model 3 as obtained from TT-TFD-based PFIs and LSCII-based PFIs. Shown are the matrix elements of three different memory kernels: (1) The memory kernel of the populations-only GQME [$\mathcal{K}^{\text{pop}}(\tau)$], which has four elements ($DDDD, DDAA, AADD, AAAA$) and is depicted with solid cyan lines for the results from TT-TFD-based PFIs and dashed magenta lines for the results from LSCII-based PFIs; (2) and (3) The single-element memory kernels of the scalar single-population GQMEs [$\mathcal{K}_{DD,DD}^{\text{donor}}(\tau)$ and $\mathcal{K}_{AA,AA}^{\text{acceptor}}(\tau)$], which are depicted in the $DDDD$ and $AAAA$ panels, respectively, with solid green lines for the results from TT-TFD-based PFIs and dashed yellow lines for the results from LSCII-based PFIs.

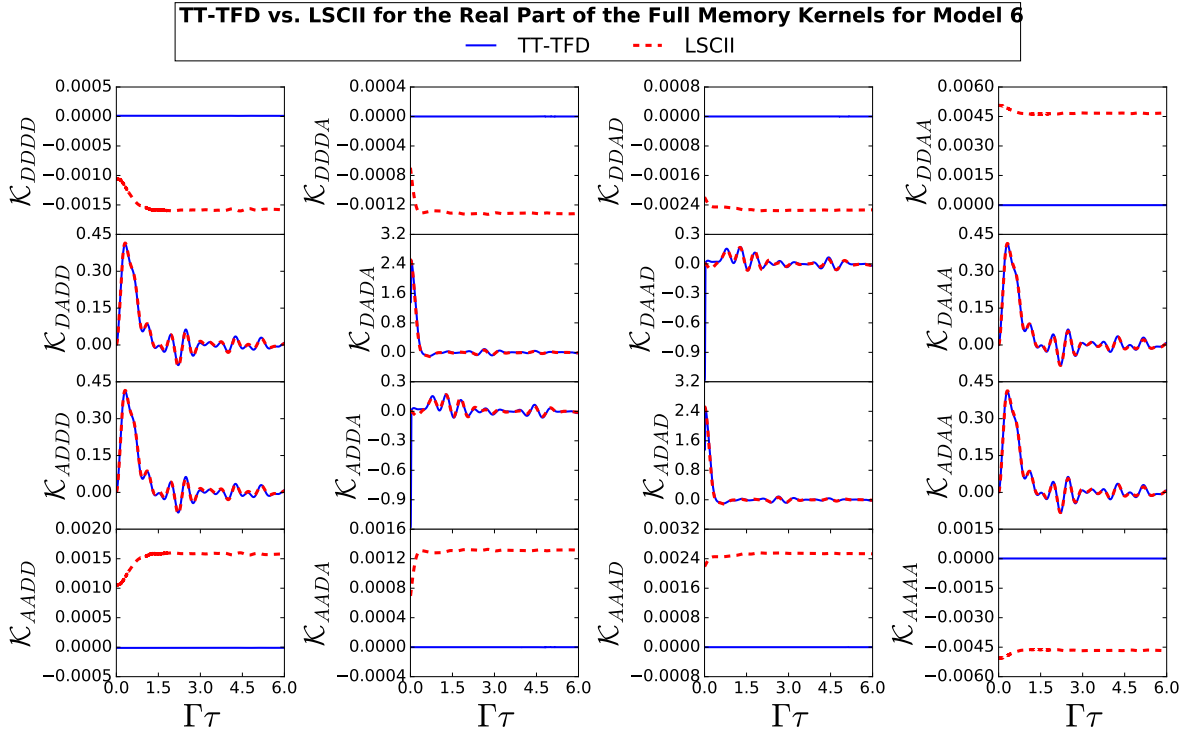


Figure S25: Real parts of the matrix elements of the memory kernel of the GQME for the full electronic density matrix $[\mathcal{K}^{\text{full}}(\tau)]$ for model 6 as obtained from TT-TFD-based PFIs (solid blue lines) and LSCII-based PFIs (dashed red lines).

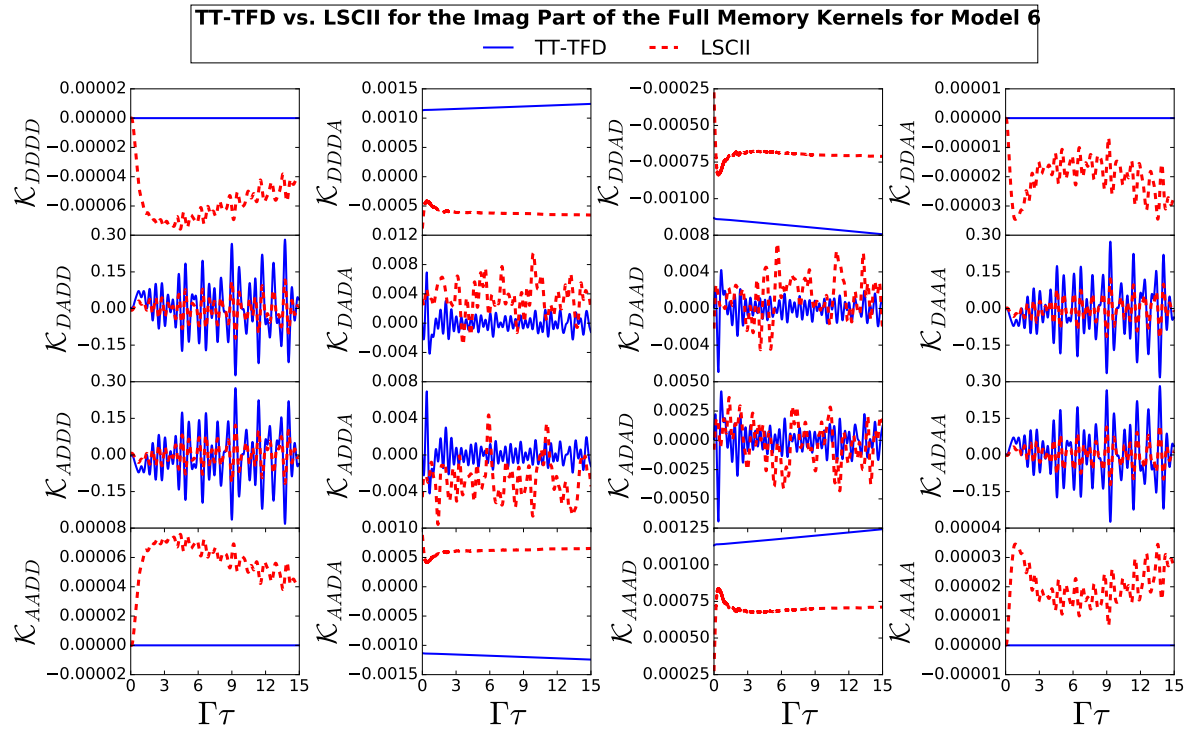


Figure S26: Imaginary parts of the matrix elements of the memory kernel of the GQME for the full electronic density matrix $[\mathcal{K}^{\text{full}}(\tau)]$ for model 6 as obtained from TT-TFD-based PFIs (solid blue lines) and LSCII-based PFIs (dashed red lines).

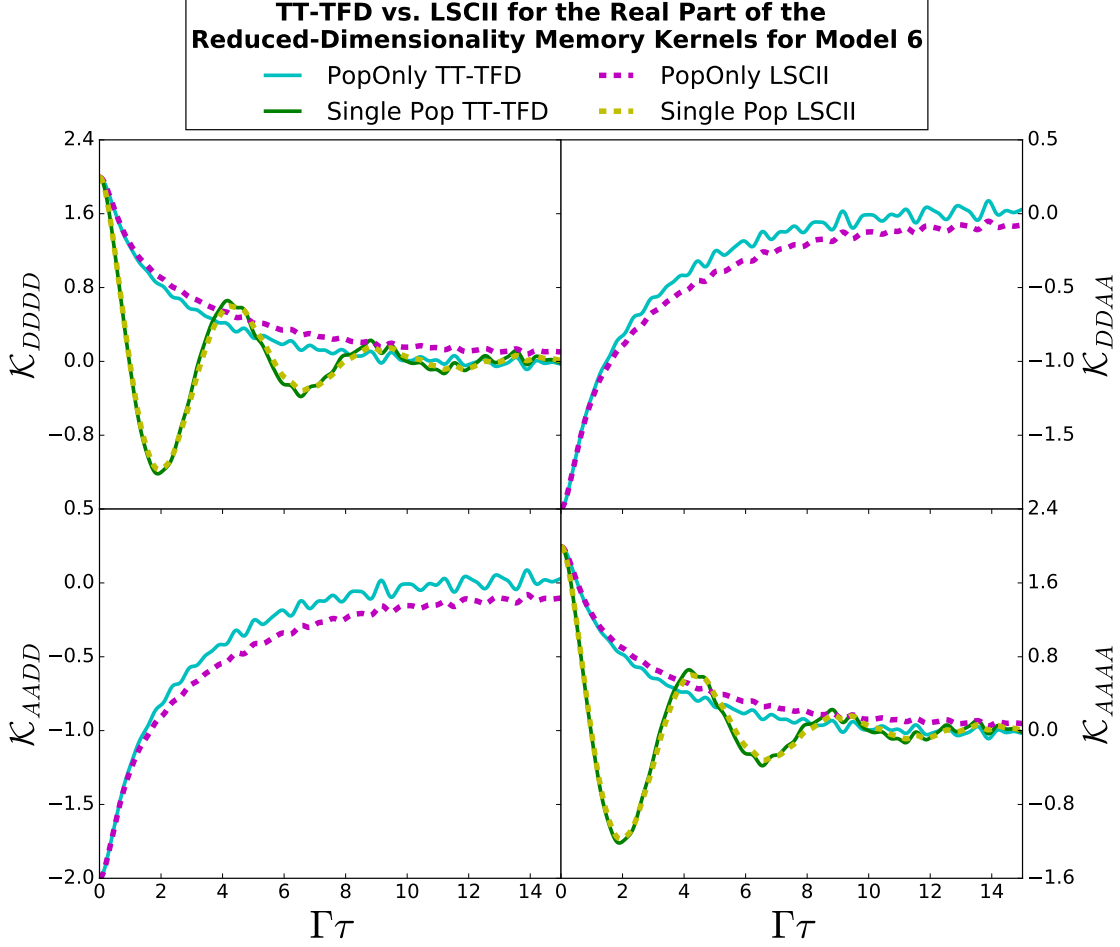


Figure S27: The real parts of the matrix elements of the memory kernels for the populations-only and single-population GQMEs for model 6 as obtained from TT-TFD-based PFIs and LSCII-based PFIs. Shown are the matrix elements of three different memory kernels: (1) The memory kernel of the populations-only GQME [$\mathcal{K}^{\text{pop}}(\tau)$], which has four elements ($DDDD, DDAA, AADD, AAAA$) and is depicted with solid cyan lines for the results from TT-TFD-based PFIs and dashed magenta lines for the results from LSCII-based PFIs; (2) and (3) The single-element memory kernels of the scalar single-population GQMEs [$\mathcal{K}_{DD,DD}^{\text{donor}}(\tau)$ and $\mathcal{K}_{AA,AA}^{\text{acceptor}}(\tau)$], which are depicted in the $DDDD$ and $AAAA$ panels, respectively, with solid green lines for the results from TT-TFD-based PFIs and dashed yellow lines for the results from LSCII-based PFIs.

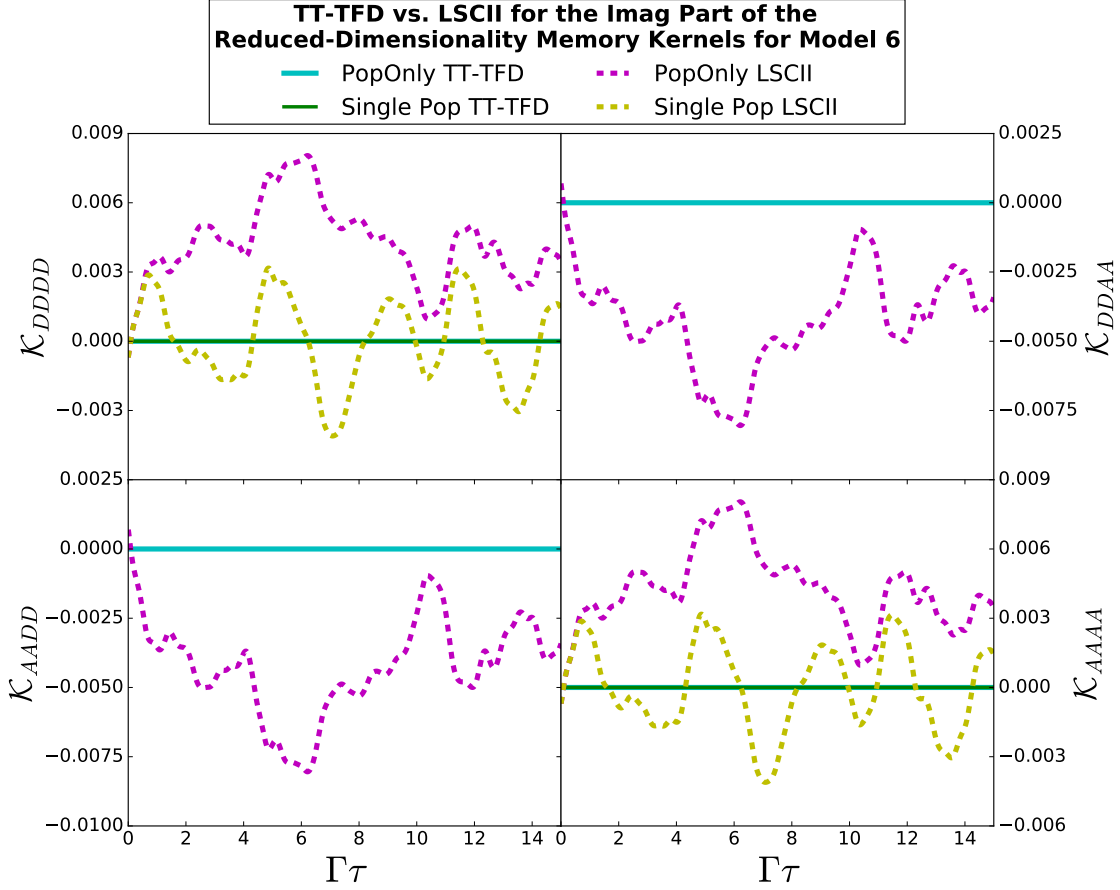


Figure S28: The imaginary parts of the matrix elements of the memory kernels for the populations-only and single-population GQMEs for model 6 as obtained from TT-TFD-based PFIs and LSCII-based PFIs. Shown are the matrix elements of three different memory kernels: (1) The memory kernel of the populations-only GQME [$\mathcal{K}^{\text{pop}}(\tau)$], which has four elements ($DDDD$, $DDAA$, $AADD$, $AAAA$) and is depicted with solid cyan lines for the results from TT-TFD-based PFIs and dashed magenta lines for the results from LSCII-based PFIs; (2) and (3) The single-element memory kernels of the scalar single-population GQMEs [$\mathcal{K}_{DD,DD}^{\text{donor}}(\tau)$ and $\mathcal{K}_{AA,AA}^{\text{acceptor}}(\tau)$], which are depicted in the $DDDD$ and $AAAA$ panels, respectively, with solid green lines for the results from TT-TFD-based PFIs and dashed yellow lines for the results from LSCII-based PFIs.

S.VII Graphs of the Inhomogeneous Terms of All of the Models

Given in this section are the graphs of the real part of the inhomogeneous terms for models 1, 2, 3, and 6. The imaginary part is not shown, as it is zero for all models for both inhomogeneous terms calculated via TT-TFD and LSCII.

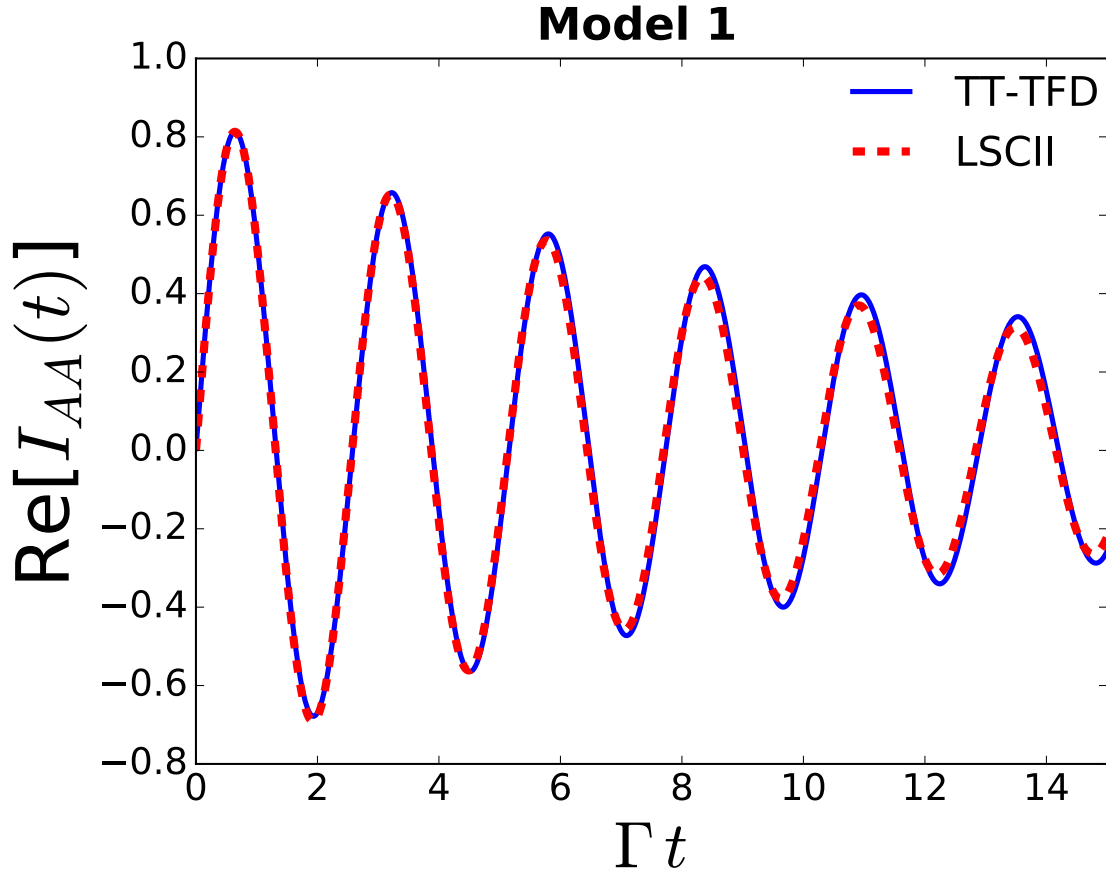


Figure S29: Real part of $\hat{I}_{AA}(\tau)$ for model 1, as obtained from TT-TFD-based PFIs (solid blue lines) and LSCII-based PFIs (dashed red lines).

References

- [1] R. Zwanzig, *Nonequilibrium statistical mechanics* (Oxford University Press, New York, 2001).
- [2] A. Nitzan, *Chemical Dynamics in Condensed Phases* (Oxford University Press, New York, 2006).

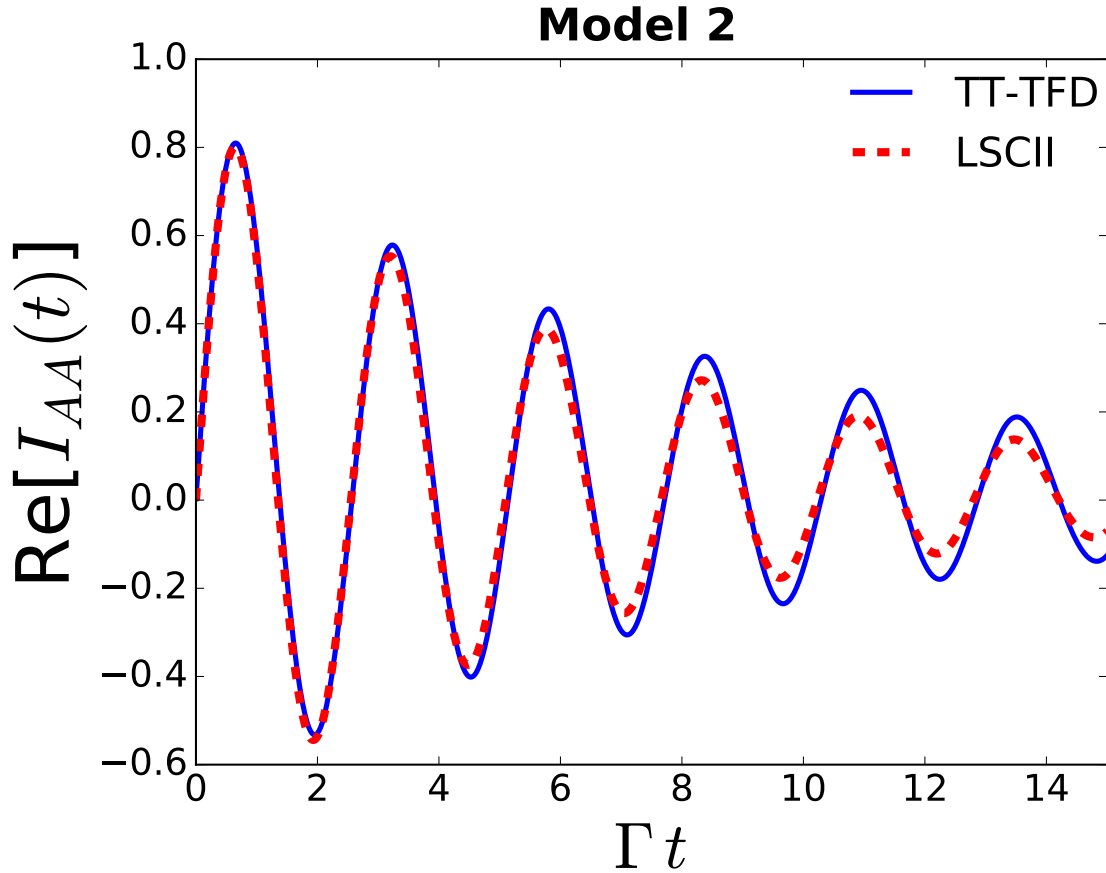


Figure S30: Real part of $\hat{I}_{AA}(\tau)$ for model 2, as obtained from TT-TFD-based PFIs (solid blue lines) and LSCII-based PFIs (dashed red lines).

- [3] S. Mukamel, *Principles of Nonlinear Optical Spectroscopy* (Oxford, New York, 1995).
- [4] H.-P. Breuer, F. Petruccione, *The Theory of Open Quantum Systems* (Oxford Press, Oxford, 2002).
- [5] E. Mulvihill, E. Geva, *J. Phys. Chem. B* **125**, 9834 (2021).
- [6] E. Mulvihill, A. Schubert, X. Sun, B. D. Dunietz, E. Geva, *J. Chem. Phys.* **150**, 034101 (2019).
- [7] E. Mulvihill, E. Geva, *J. Chem. Phys.* **156**, 044119 (2022).
- [8] Q. Shi, E. Geva, *J. Chem. Phys.* **119**, 12063 (2003).
- [9] Q. Shi, E. Geva, *J. Chem. Phys.* **120**, 10647 (2004).
- [10] M.-L. Zhang, B. J. Ka, E. Geva, *J. Chem. Phys.* **125**, 044106 (2006).
- [11] B. J. Ka, M.-L. Zhang, E. Geva, *J. Chem. Phys.* **125**, 124509 (2006).

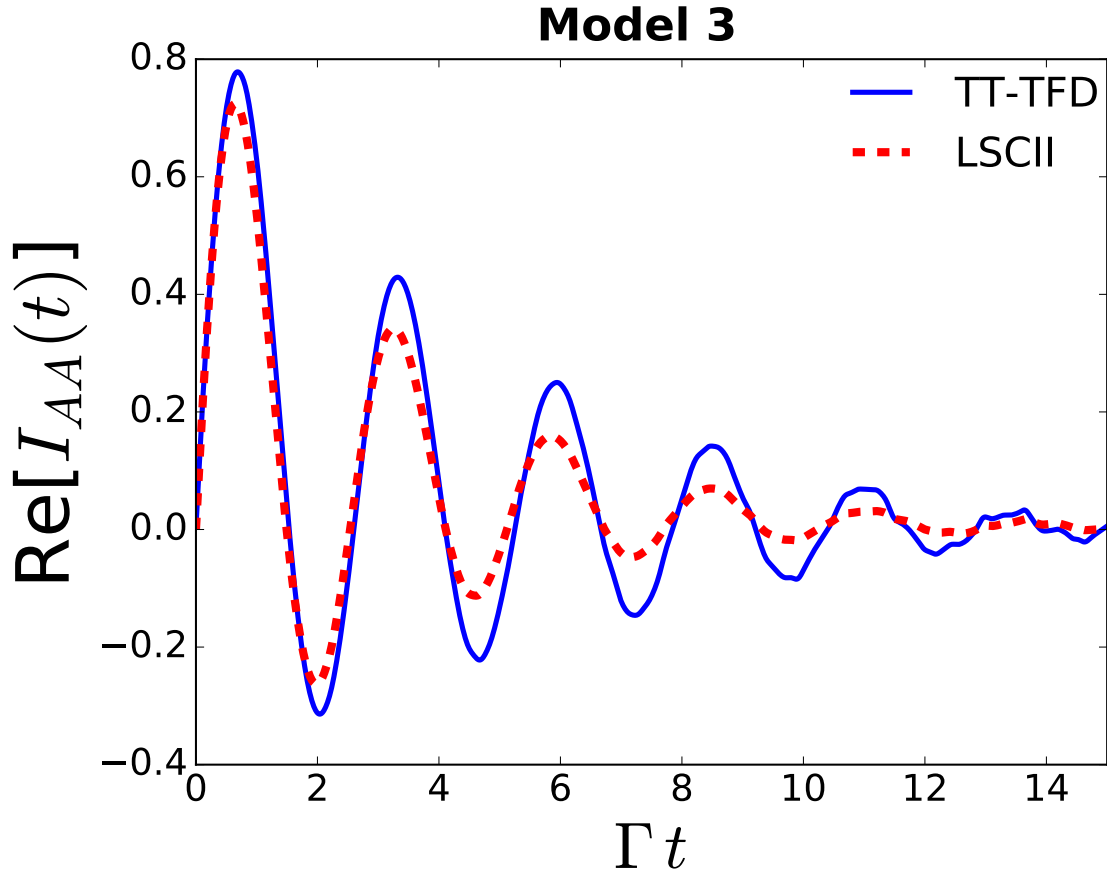


Figure S31: Real part of $\hat{I}_{AA}(\tau)$ for model 3, as obtained from TT-TFD-based PFIs (solid blue lines) and LSCII-based PFIs (dashed red lines).

- [12] G. Cohen, E. Rabani, *Phys. Rev. B* **84**, 075150 (2011).
- [13] E. Y. Wilner, H. Wang, G. Cohen, M. Thoss, E. Rabani, *Phys. Rev. B* **88**, 045137 (2013).
- [14] G. Cohen, E. Y. Wilner, E. Rabani, *New Journal of Physics* **15**, 073018 (2013).
- [15] G. Cohen, E. Gull, D. R. Reichman, A. J. Millis, E. Rabani, *Phys. Rev. B* **87**, 195108 (2013).
- [16] A. Kelly, T. E. Markland, *J. Chem. Phys.* **139**, 014104 (2013).
- [17] L. Kidon, E. Y. Wilner, E. Rabani, *J. Chem. Phys.* **143**, 234110 (2015).
- [18] W. C. Pfalzgraff, A. Kelly, T. E. Markland, *J. Phys. Chem. Lett.* pp. 4743–4748 (2015).
- [19] A. Montoya-Castillo, D. R. Reichman, *J. Chem. Phys.* **144**, 184104 (2016).
- [20] A. Kelly, N. Brackbill, T. E. Markland, *J. Chem. Phys.* **142**, 094110 (2015).

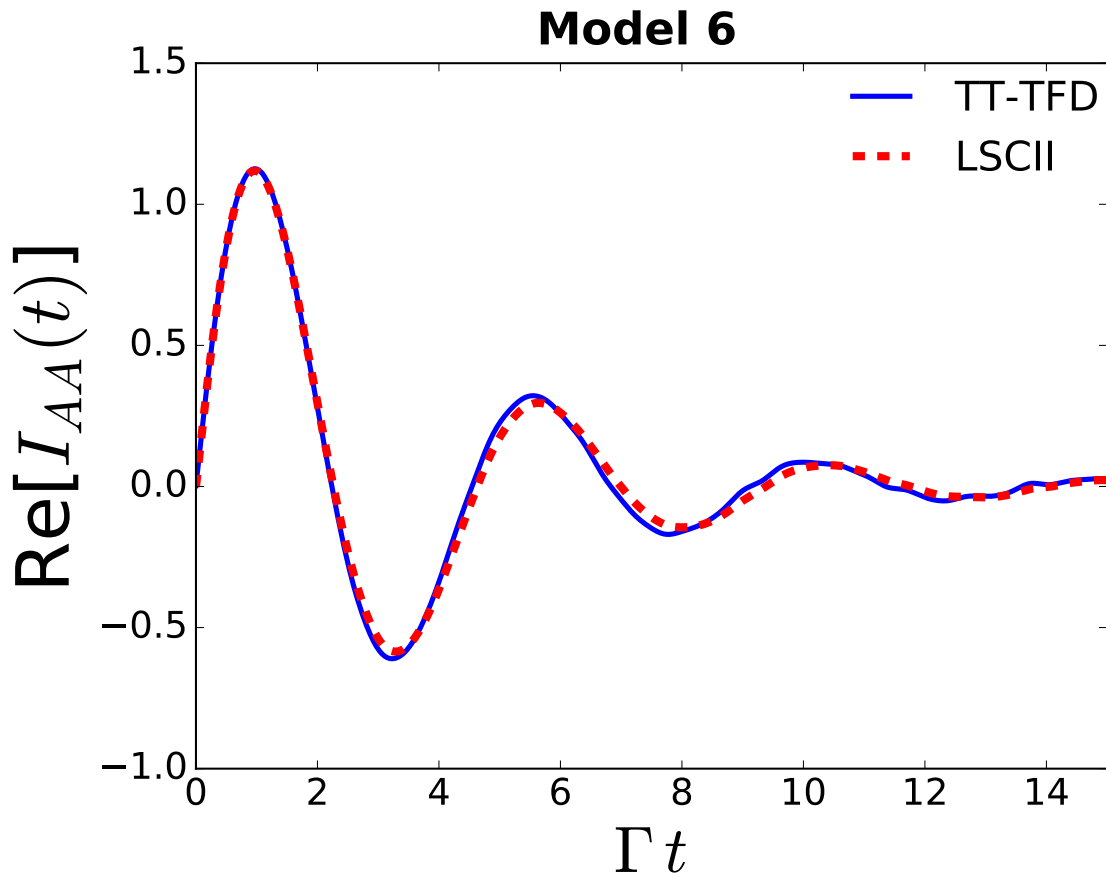


Figure S32: Real part of $\hat{I}_{AA}(\tau)$ for model 6, as obtained from TT-TFD-based PFIs (solid blue lines) and LSCII-based PFIs (dashed red lines).

- [21] A. Kelly, A. Montoya-Castillo, L. Wang, T. E. Markland, *The Journal of Chemical Physics* **144**, 184105 (2016).
- [22] L. Kidon, H. Wang, M. Thoss, E. Rabani, *The Journal of chemical physics* **149**, 104105 (2018).
- [23] W. Pfalzgraff, A. Montoya-Castillo, A. Kelly, T. Markland, *J. Chem. Phys.* **150**, 244109 (2019).
- [24] E. Mulvihill, *et al.*, *J. Chem. Phys.* **151**, 074103 (2019).
- [25] E. Mulvihill, *et al.*, *J. Chem. Phys.* **154**, 204109 (2021).
- [26] N. Ng, D. T. Limmer, E. Rabani, *The Journal of Chemical Physics* **155**, 156101 (2021).